POLITECNICO
MILANO 1863

SCUOLA DI INGEGNERIA INDUSTRIALE
E DELL'INFORMAZIONE

Sabot design for improved performance in bird strike testing

Tesi di Laurea Magistrale in
Aeronautical Engineering - Ingegneria Aeronauticaa

Author: **Marco Salvatore**

Student ID: 915371
Advisor: Prof. Marco Anghileri
Co-advisors: Ivan Colamartino, Navid Ghavanini, Giulia Vignati
Academic Year: 2021-22

Abstract

High-speed impact testing between birds and aircraft components is essential to simulate birdstrike events in order to certify aircraft and ensure the safety of all passengers on board.

The La.S.T. laboratory of the Politecnico di Milano conducts these tests, through a dedicated launch system, consisting of a compressed air cannon. The launch system accelerates projectiles, such as real birds or surrogates in ballistic gelatin, against the aeronautical components to be tested. This experimental thesis addresses the problem of birdstrike and focuses on increasing the efficiency of one of the main components of the gun, called Sabot.

In particular, the aim is to maximise the speed at which the projectile can be launched during testing, in order to broaden its application field. A new sabot is therefore developed through a design and optimization process based on an iterative approach, which exploits both finite element analysis and experimental testing. The guiding principles for the design are identified starting from the requirements to be met, also considering the main criticalities related to the production of the new component.

During the optimization phase, several versions of the sabot are developed, analyzing and investigating different possible configurations, up to the realization of a bi-material component which maximizes performances.

Keywords: Birdstrike, sabot, air cannon, ballistic test

Abstract in lingua italiana

I test di impatto ad alta velocità tra volatili e componenti di velivoli sono essenziali per simulare eventi di birdstrike al fine di certificare gli aerei stessi e di garantire la sicurezza dei passeggeri a bordo.

Il laboratorio La.S.T. del Politecnico di Milano conduce tali test, tramite un sistema di lancio dedicato, costituito da un cannone ad aria compressa. Tramite il sistema di lancio si accelerano dei proiettili, quali uccelli reali o surrogati in gelatina balistica, contro i componenti aeronautici da testare. Questa tesi sperimentale affronta il problema del birdstrike e si focalizza sull'incremento dell'efficienza di uno dei componenti principali del cannone, detto Sabot.

In particolare si desidera massimizzare la velocità alla quale il proiettile può essere lanciato durante i test, al fine di ampliarne il campo d'applicazione. Un nuovo sabot viene dunque sviluppato tramite un processo di progettazione e ottimizzazione basato su un approccio iterativo, il quale si avvale sia di analisi ad elementi finiti che di prove sperimentali. I principi guida per la progettazione vengono identificati a partire dai requisiti da soddisfare, considerando anche le principali criticità legate alla produzione del nuovo componente.

Nella fase di ottimizzazione si sviluppano più versioni del sabot, analizzando e investigando diverse possibili configurazioni, fino ad arrivare alla realizzazione di un componente bi-materiale che ne massimizza le prestazioni.

Parole chiave: Impatto volatile, sabot, cannone ad aria, test balistico

Contents

1 | Introduction

The purpose of this chapter is to introduce the reader to the bird-strike phenomenon, also known as bird aircraft strike hazard (or BASH). Particular emphasis is put on the dangers it poses to the civil aviation sector. The aim is to highlight some key features of this problem, which has often been overlooked in the past, in order to better catch the context of applicability of this thesis. A discussion on the evolution of bird-strikes monitoring and risk mitigation tools follows, in order to provide the most significant data found in literature from the main agencies which deal with this issue. Ballistic testing is then presented as a mean to reproduce and study bird-strike events. Lastly, the work outline is introduced.

1.1. BirdStrike Phenomenon

A Birdstrike is an event that involves a collision between a bird and an aircraft, it can have severe consequences on the passengers' safety since it could lead to fatal accidents. For this reason the birdstrike phenomenon is widely studied and monitored by all major airports and aviation bodies, such as: International Civil Aviation Organization (ICAO), Federal Aviation Administration (FAA) and European Union Aviation Safety Agency (EASA).

At the dawn of civil aviation, with the first scheduled passenger flight from Paris to London carried out in 1910, the number of flying aircrafts was very limited and birdstrikes events were extremely rare. However as the global aviation evolved, providing more air traffic and larger aircrafts traveling at higher speeds, the probability of a bird-strike event to occur increased, as well as the damage severity due to such collisions. Nowadays birdstrikes are quite common and unfortunately it seems that they are destined to increase in number. In fact in the last decades the aviation sector has seen a significant growth, as attested by the International Civil Aviation Organization (ICAO) which produces monthly an Air Transport Monitor [19] providing economic analysis as well as many indicators regarding the global aviation traffic. From these reports it emerges that not only the worldwide traffic has significantly increased over the last decades with a grow-rate of 5.2%, but also

that the demand for air transport will increase by an average of 4.3% per annum over the next 20 years according to the latest estimates (see fig. 1.1). If these predictions will actually take place, more that 200.000 flights per day are expected to take off by mid-2030s, and therefore the probability of birdstrike occurrence is expected to increase as well.

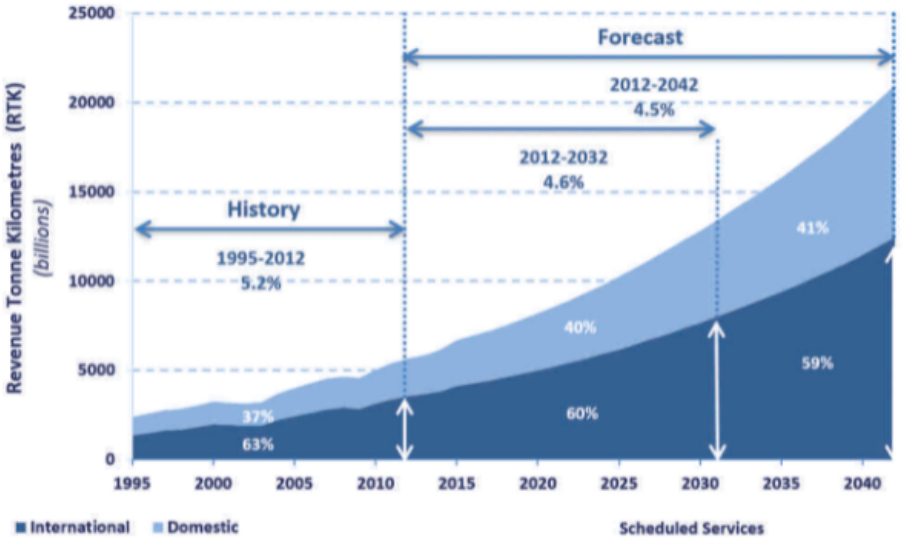

Figure 1.1: ICAO Future Air Transport Estimates, [19]

From 2008 to 2015 ICAO also produced a detailed report [20] on the major wildlife strikes occurred during this time span, emphasizing how grave the safety hazard and the damages deriving from such collisions can be. Even if around the 92% of the total impacts between aircrafts and volatiles do not causes appreciable damage, there are still many cases in which these events can lead to minor or substantial damage to the aircrafts, compromising the passengers' safety on board. In this regard it's explanatory the emergency landing of US Airways Flight 1549 Airbus 320 into the Hudson River on January 15, 2009; due to the ingestion of many Migratory Canada geese into both engines at an altitude of 2,818 feet. This accident was followed by a thorough investigation [29], conducted by the U.S. National Transportation Safety Board (NTSF), which demonstrated how dangerous aircrafts' collisions with birds and other wildlife really are. In the following years, from 2009 to 2020, over $350 millions of Airport Improvement Program (AIP) funds have been allocated to wildlife-related projects such as Wildlife Hazard Assessments and Wildlife Hazard Management Plans.

According to the Wildlife Strike Analyses [20] performed by ICAO, 91% of the strikes occur nearby the aerodrome. Of these occurred collisions 31% takes place during take-off (at an altitude below 1000 ft), while 59% of them typically occurs during the approach and landing phase. Bird-strikes reported at higher altitudes are very rare and they account only for a small percentage of the total cases, as shown in fig. 3.15b
Depending on the extent of the damage reported by the aircraft due to a bird-strike, the flight-plan is effected accordingly: for substantial or severe damages pilots can decide to abort take off or to perform a precautionary/emergency landing, while another serious emergency situation occurs when one or more engines shut down.

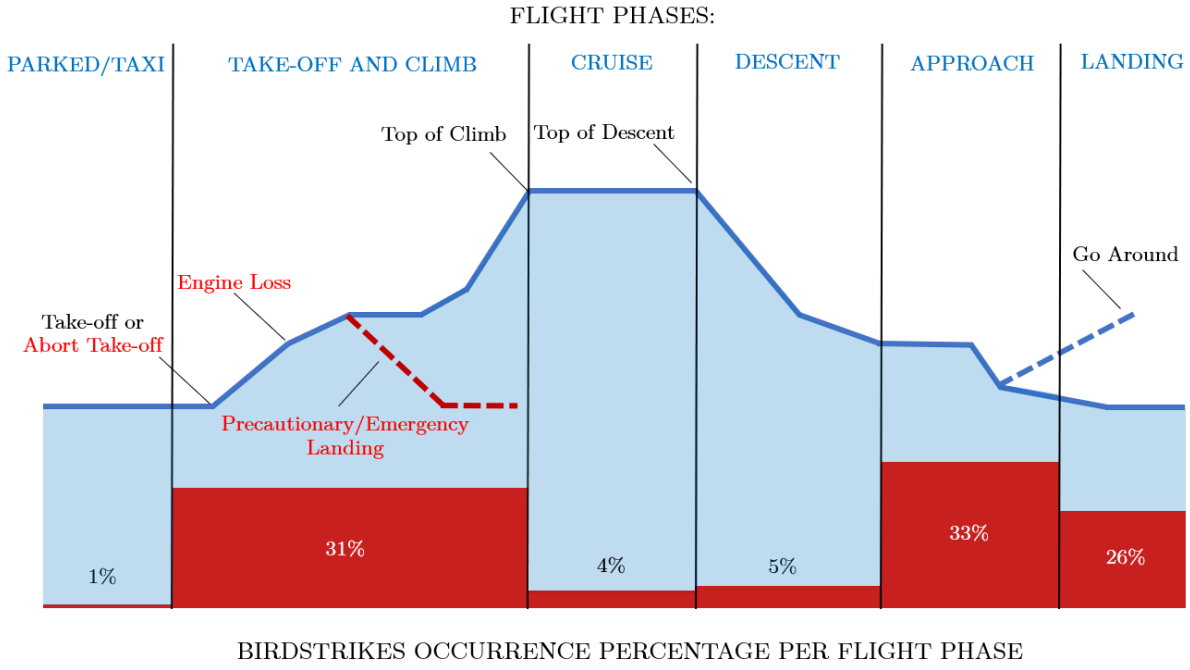

Figure 1.2: Birdstrikes occurrence percentage per flight phase

Further wildlife strikes effects on the flight include, but are not limited to: flight delay, declaring technical emergency and aircraft return.

All reported strikes are investigated and all the information, including the area of the aircraft affected by the impact and the damage it caused, is coded. When reports are filed, it is important that all relevant information is provided whenever possible also regarding the phase of flight in which the collision occurred, time and altitude of the strike, species and number of volatiles involved for identification purposes [11]. From all this data it appears that the most struck parts of an aeroplane are the Windshield, the wings and the nose, while the parts that suffer the greatest damage are the engines and wings. Fig.3.15c

illustrates the respective percentages for every part of the aircraft typically damaged by wildlife strikes.

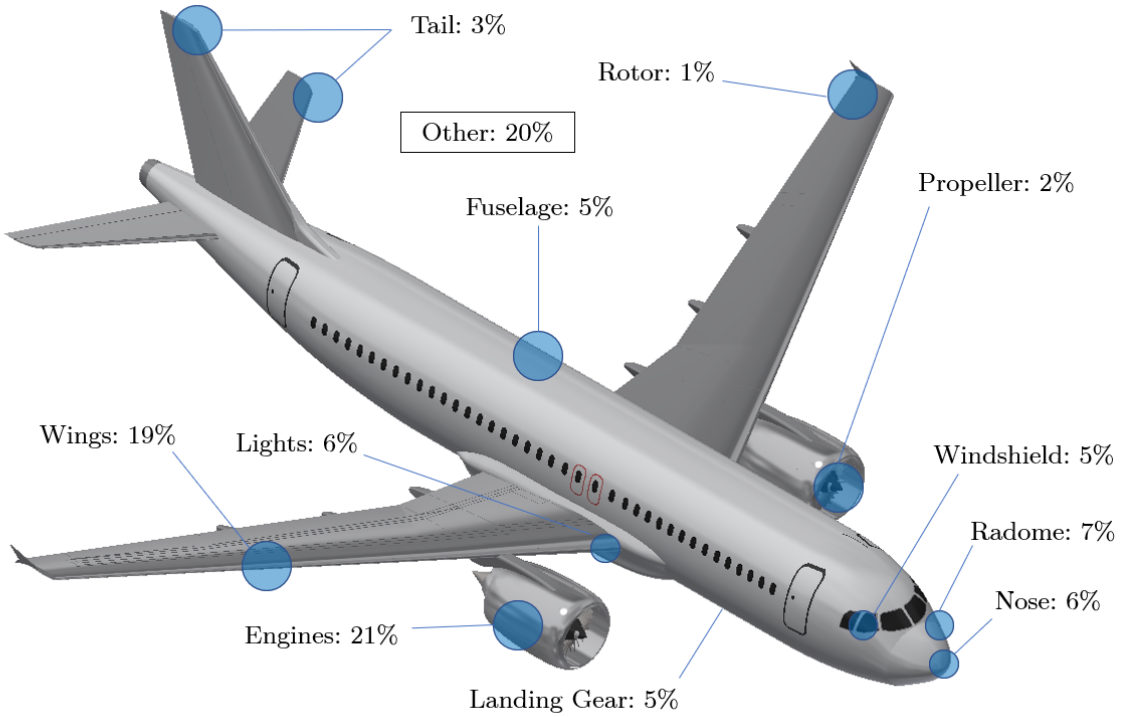

Figure 1.3: Birdstrike rates per different aircaft parts

Current certification standards [27] provide strict requirements in order to guarantee that both engines and airframe are able to withstand bird impacts without endangering the flight's safety. Nevertheless the engine is still the most vulnerable element given that it is only certified to sustain the ingestion of a small number of birds, therefore in the event of an impact with flocks of large birds, a sudden loss of power remains likely.

Since 1965 the FAA availed itself with Advisory Circulars on Bird Hazards to Aviation as the main tool in the wildlife program to systematically improve its oversight for reducing risks. Management efforts to lower the risks of birdstrikes have primarily focused on airports since most civil aircraft strikes occur (during take-off and landing at $<$500 ft). However the certificated airports that have stabilized or reduced damaging strikes for commercial transport aviation in recent years have done little to reduce strikes outside the airport environment (such as occurred with US Airways Flight 1549). The main solutions to mitigate the risk for birdstrikes occurring beyond the airport fences consist in

integrating avian radar and bird migration forecasting into airspace management for civil aviation [4], alongside with a further development of aircraft lighting systems to enhance detection and avoidance by birds [12]. Furthermore, since nowadays there's still a great need for increased and more detailed strike reporting, it is highly desirable to incorporate new technology in order to optimize such procedure and to keep providing Airport Improvement Program (AIP) funds to keep conducting Wildlife Hazard Assessments and to develop Wildlife Hazard Management Plans.

1.2. Ballistic Testing

Every aircraft must undergo a development and certification process which assess its ability to withstand possible birdstrikes. Birds impact tests play a fundamental role in such phase. These tests are necessarily conducted in a controlled environment as it is important to ensure their accuracy, repeatability and safety. They consist in reproducing as faithfully as possible a birdstrike event by shooting a real or a surrogate bird at an aircraft component. To all intents and purposes these types of tests fall within the purview of ballistics. Ballistics is the science of motion of projectiles in flight [7]: such discipline studies the launch of a projectile, its behavior during flight and the effects of its final impact. Throughout history ballistic has had a main role in the development of space launchers, missiles, munitions and unmanned aircrafts. Its main applications are in the experimental flight dynamics branch for the determination of a projectile's flight data such as: ballistic trajectory, velocity, flight attitude and aerodynamic coefficients. Among all these flight data, the most relevant ones for the purposes of this thesis are: velocity and trajectory.

The projectile is defined as a flying object following a ballistic trajectory, which in our case will be taken as the sabot-bird package accelerated up to the desired speed. In order to accelerate projectiles in ballistics tests a number of different guns can be employed depending on the test's requirements. The most common ones are powder gas guns or light-gas guns. A more detailed description of these launching systems will be given in chapter 2.

The ballistic test range is an indoor firing range used to examine the projectile's flight dynamics and its impact loading behavior, Polytechnic of Milan has its own firing range at La.S.T laboratory, were all experimental tests inherent birdstrikes are conducted using

a single-stage gas cannon. To capture the projectile's position and attitude history is one of the main goals of a ballistic test; from the 1950's this was mainly accomplished by using yaw cards and sparks photographic stations. Yaw cards [7] are low density and resistance targets connected to a light weight frame and arranged in an equally spaced series along the projectile's flight path, as shown in fig.1.4. They are typically made out of low strength material as to be easily pierced by the projectile without causing too much attitude disturbance.

Figure 1.4: Yaw Cards [22]

However simple, such instrumentation allows to extrapolate the projectile's yaw motion and its aerodynamic coefficients by recovering little data from each card. Nowadays they are still used for projectile development since predictive codes don't always provide precise aerodynamic coefficients at high Mach regimes. In the experimental tests conducted during this thesis work there was no need to use yaw cards, given a not excessively high Mach number and a short distance firing range. Another apparatus used in the past to retrieve important data from a ballistic test consisted in multiple spark photographic stations [10] which provided snapshots of the projectile's passage through the ballistic test range. Its operation involves generating a spark to project the shadow of the projectile and its surrounding flow on a screen which is then photographed (fig.1.5a). Despite the low resolution, the resulting shadow-graph (fig.1.5b) was able to effectively highlight the projectile's pitch along with the density gradient in the disturbed flow, providing a deeper understanding of high-velocity phenomena.

(a) Spark Photographic Stations

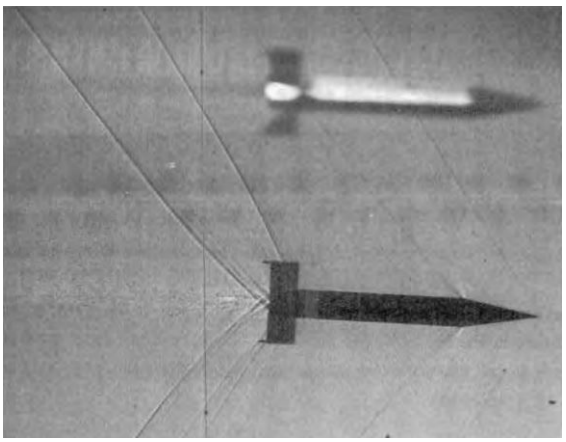

(b) Shadowgraph

Figure 1.5: Indoor Test Range and Projectile Views, [10]

With the development of new technologies and improved optics, photographic stations have evolved to such an extent that it is now possible to capture entire videos of high-speed phenomena such as a projectile motion.

1.3. Thesis Motivation and Objectives

The aim of this experimental thesis is to maximize the impact speed of the surrogate bird used in bird-impact tests at La.S.T Laboratory by means of the design and optimization process of the launch system's component called Sabot.

The achievement of higher impact velocities is of paramount importance in the execution of future bird impact tests as it would allow to study more faithfully phenomena such as the collision of birds with helicopter rotors or with airplanes flying at greater speeds in different flight phases.
In the following, the methodology adopted for the design of a new Sabot will be discussed, in which both numerical simulations and experimental tests are exploited. 3D printing technology was adopted for the realization of the new component and all obtained results from the experimental tests were compared with the numerical outputs of the simulations in order to validate the Sabot's model developed in previous design phases.

1.4. Thesis Outline

This experimental thesis is organized into 6 Chapters:

- **Chapter 1** introduces the reader to the bird-strike phenomenon, to the typical experimental tests for studying it and defines the scope of the thesis.
- **Chapter 2** provides an overview on the launching system used to simulate bird-strikes at high velocities, describing its main components alongside with some previously performed improvements with respect to the original system.
- **Chapter 3** illustrates the design process for the sabot component and the principles upon which it is based, explaining methods and algorithms behind some decision-making tools. At the end of this chapter the obtained preliminary designs are presented.
- **Chapter 4** deals with the optimization procedure adopted to improve all preliminary designs. It describes in details the development of numerical models, the production of finished components and the execution of experimental tests.
- **Chapter 5** gathers and provides all achieved results, a numerical-experimental comparison is performed in order to assess the correlation between numerical simulations' outputs and experimental tests' results.
- **Chapter 6** presents the conclusion to this research work and future developments of the study are investigated.

2 | State of the art

This chapter describes the whole launching system, its various possible configurations, its components and the main changes it underwent in the past at La.S.T laboratory.

2.1. Launching System

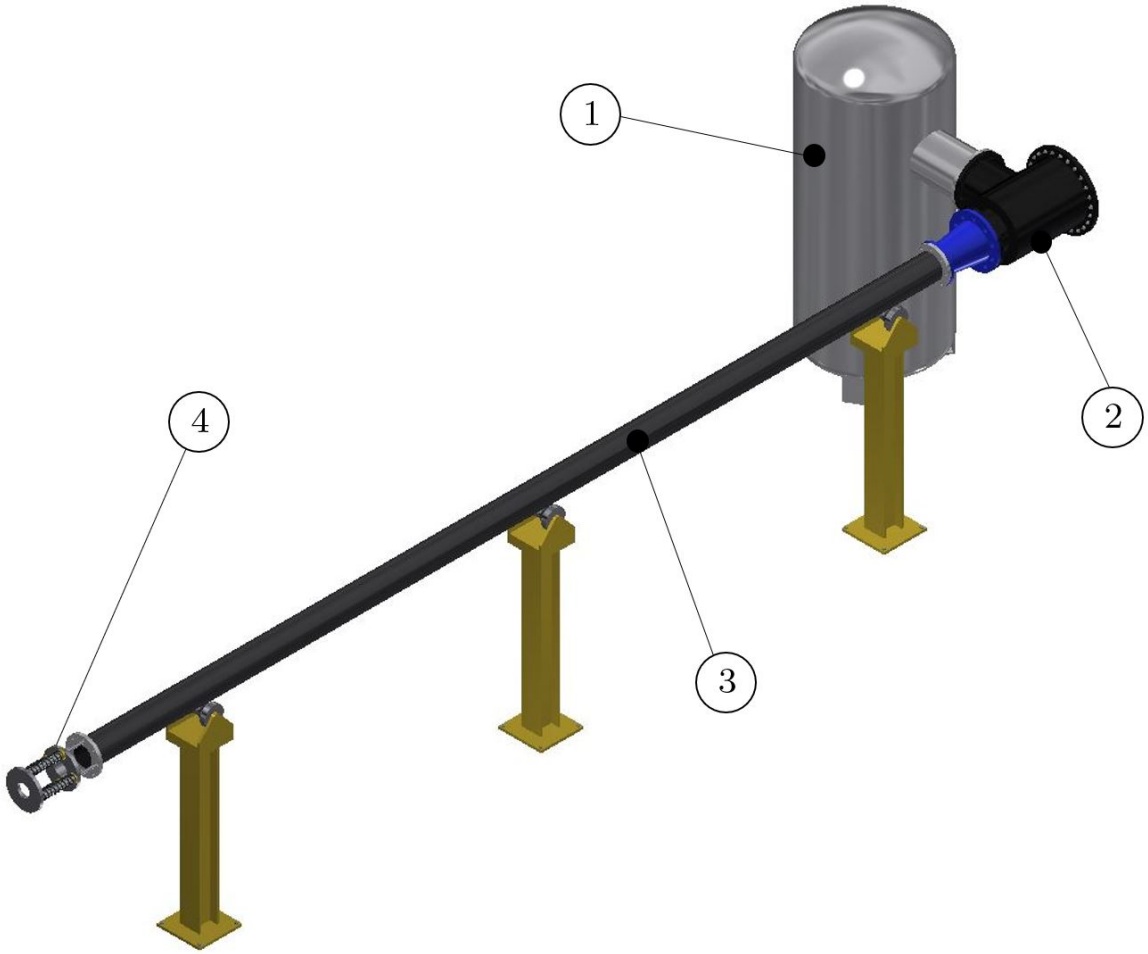

Figure 2.1: Launch System

The launch system currently used at La.S.T. laboratory consists of the following main components needed to perform the ballistic tests, with reference to fig.2.1 :

1. Pressure tank
2. Fast acting valve
3. Barrel
4. Stopper

Several launch system configurations or architectures for high-speed impact testing applications exist, they typically differ in the projectile propulsion mode and in the launch trigger mechanism:

- Explosive
- Single-Stage Gas Gun
- Fast acting valve
- Two-Stage Gas Gun
- Wrap Around

2.1.1. Explosive

Until the 1950's the most powerful guns fired projectiles for range tests using gun powder [7], [31]. These launch systems generate a high pressure wave which accelerates the projectile no longer by the instantaneous release of compressed gas, but by the ignition of propellant charges. contained in a breech chamber. Such procedure allows to reach very high speeds (even in the supersonic field) and maintains the advantage of a great operational simplicity, which is why it's still used today as a research tool. However explosive launch systems also have several disadvantages: high pressures and temperatures can damage the projectile and, in the long term, erode the chamber. Furthermore it is difficult to control the launch pressure, which directly depends on the amount of gun powder used. In light of this and considering that such launch systems presents an intrinsic danger due to the explosive reaction, they have never been employed at La.S.T. laboratory.

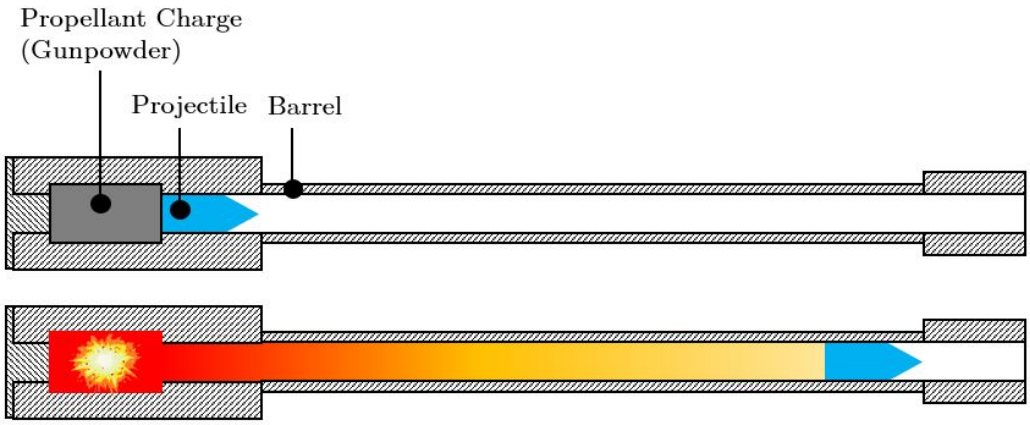

Figure 2.2: Explosive System Scheme

2.1.2. Single-Stage Gas Gun

Single-stage gas guns are among the simplest systems used to perform impact tests in aerospace industries due to the high velocity they generate [8]. Their architecture consists of a pressure reservoir, or tank, containing the propellant gas separated from the rest of the gun by a diaphragm. Inert gases such as helium or nitrogen are typically used, but often pressurized air is simply employed. The diaphragm has the task of keeping the gas separated from the projectile until the desired firing pressure is reached, at its rupture the released gas accelerates the projectile. The diaphragm may consist of a thin metal foil punctured by a penetrator when the system is triggered, or by a polyester membrane (usually in Mylar® material) which is then broken by an electrical resistance. This system being very simple and effective, it has been developed and deployed in the past at La.S.T. laboratory using a thin metal sheet as diaphragm. During its operative life, although high speeds were reached, some disadvantages also emerged. The sudden rupture of the diaphragm due to small imperfections lead to a low level of reliability, there was also the need to repeatedly replace the diaphragm at each shot. Such replacement operation always had to be carried out carefully in order to reduce gas leakage, two gaskets were needed on both sides of the diaphragm. In addition, to achieve higher speeds at higher launch pressures, more metal sheets had to be positioned. Therefore, such a launch system has been modified over the years, adopting a different trigger mechanism.

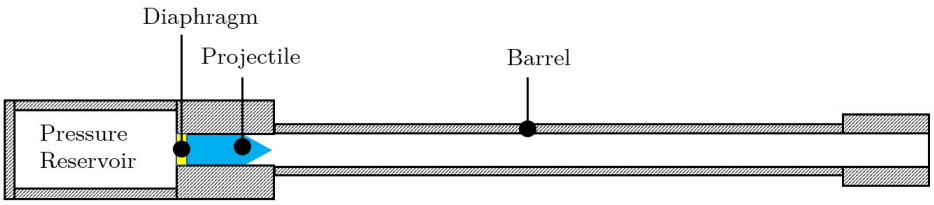

Figure 2.3: Single Stage System Scheme

2.1.3. Fast Acting Valve

The air cannon effectively in use at La.S.T. laboratory is based on a fast acting valve architecture. Such configuration allows to guarantee great accuracy and repeatability for all launches. The fast acting valve, interposed between the pressure reservoir and the barrel (fig. 2.4), has the advantage of being able to precisely adjust the firing pressure before the launch. It's then possible to release the compressed gas all at once and almost instantaneously thanks to the dedicated fast acting valve which has a millisecond order opening time as well as a wide section.

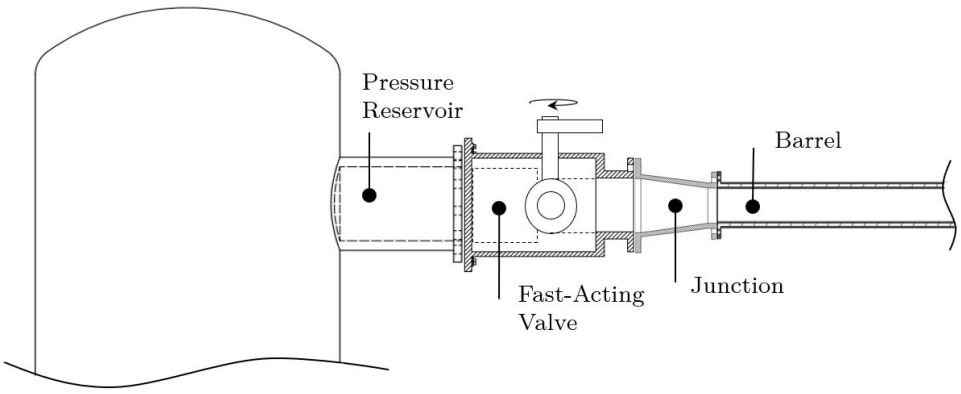

Figure 2.4: Embedded Valve Scheme

Such valves are typically employed in the industry to remove clogging in pipes and silos by releasing a pressure wave. Their application to the launch system allows to realize a controllable trigger mechanism, greatly reducing the risk of premature launches at lower pressures than the desired ones. In addition, by precisely setting the launch pressure, the desired projectile's speed can be repeatedly obtained.

2.1.4. Two-Stage Light Gas Gun

This launch system is similar to single stage gas gun previously described, with the difference from the latter of two diaphragms used instead of one. These diaphragms are separated by an intermediate chamber and they allow to reach higher launch pressures and therefore higher speeds. The system can provide for the use of explosive charges or high pressure gases in the main chamber. In the two-stage light gas gun [13] the first stage starts with the rupture of the first diaphragm separating the main chamber from the intermediate one. Compressed air reservoir or the firing of a charge in the main chamber is used to propel a piston into a tube containing the driver gas which is compressed. During this phase very high temperatures are reached. When the driver gas reaches the desired driving pressure the second diaphragm ruptures and the second stage begins. The driver gas is now free to accelerate the projectile inside the barrel to high velocity. These two operational stages are illustrated in the scheme of Fig. 2.5.

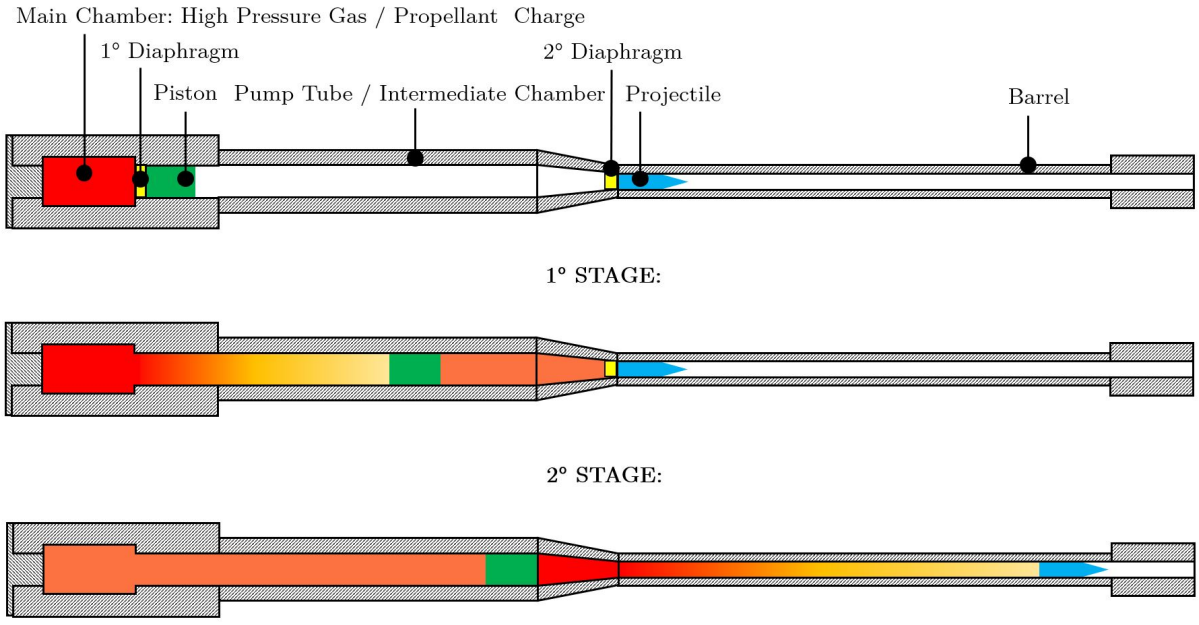

Figure 2.5: Two-Stage System Scheme

2.1.5. Wrap Around

An alternative trigger mechanism consists in the wrap around: a solution whereby the pressure reservoir is connected to the rest of the system no longer through diaphragms or valves, but directly by the projectile itself. The pressurized gas is in fact placed in a chamber around the side walls of the projectile, which maintains the sealing between tank and barrel. Once the desired launch pressure is reached, an actuator moves the projectile

forward, allowing the pressurized gas to push the latter along the barrel. However simple and controllable, this triggering mechanism also presents some drawbacks, such as: too high launch pressure may damage the projectile, which must also be specially designed to prevent gas leakages. Furthermore, wrap around requires a non-conventional tank with a particular geometry for its pressure chamber.

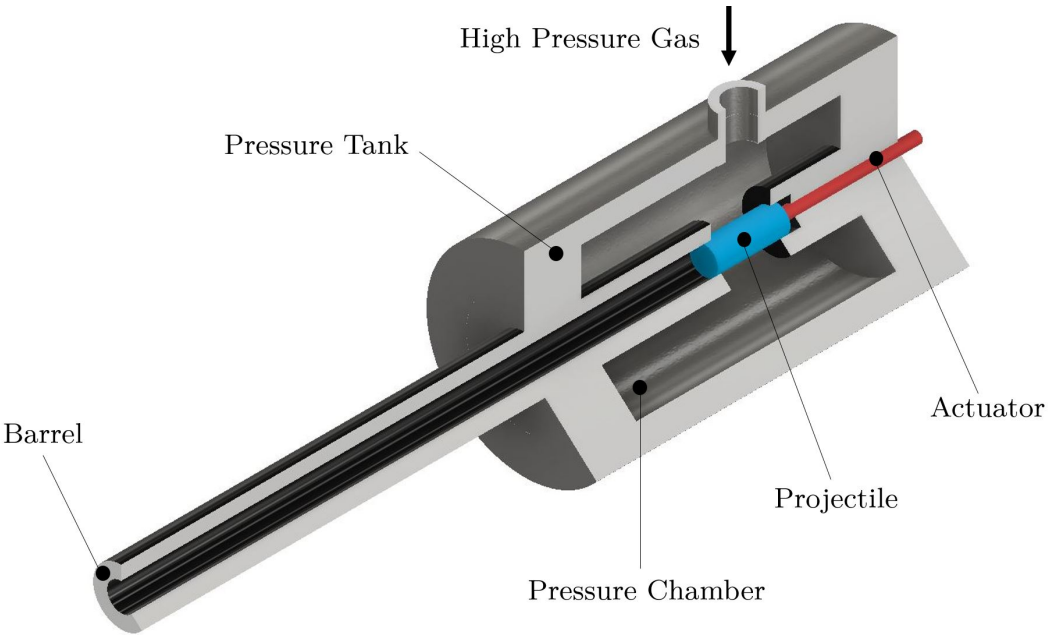

Figure 2.6: Warp Around System Scheme

2.1.6. Pressure Tank

In the early versions of the launch system at La.S.T laboratory, for which a single diaphragm was adopted, a 1000 litres tank (fig.2.7a) was connected to the barrel by a 180° turn (fig.2.7b). Such tank is certified to withstand pressures up to 10 bar.

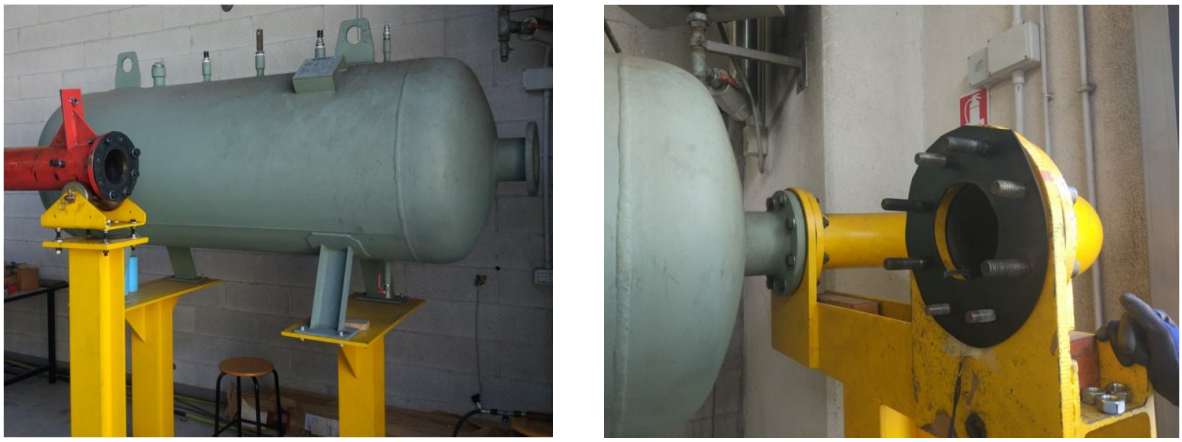

(a) 1000 Liters Tank (b) 180° Turn

Figure 2.7: Original Tank Arrangement

Subsequently, to reduce the pressure losses that such configuration with the 180° turn entails, a 90° connection was made between the tank and the barrel, as shown in fig. 2.8. In this new arrangement, a further improvement was performed by replacing the single diaphragm-based trigger mechanism with a fast acting valve.

Figure 2.8: New Tank Arrangement

2.1.7. Fast-Acting Valves

In the past, when switching to the fast-acting valve trigger mechanism, two different valves were tested, both produced by Standard Industrie: the Airchoc AC515 and AC5SP:

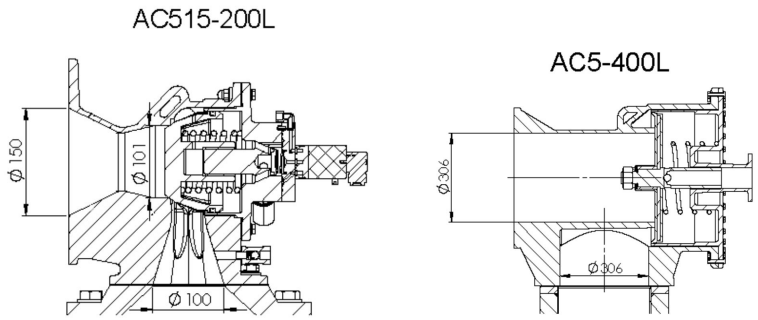

(a) AC515 Section View (b) AC5SP Section View

Figure 2.9: Fast Acting Valves

At first, the AC515 valve was fitted onto the system, for which a maximum speed of 191 $[m/s]$ was reached setting the launch pressure at 8 $[bar]$. Being this experimental result unsatisfactory, the larger AC5SP fast acting valve was installed, allowing to reach a much higher maximum speed of 230 $[m/s]$ at the same launch pressure. Therefore it was decided to maintain the AC5SP valve, which is still present in the current system architecture. The fast acting valve is connected to the barrel by means of a conical fitting as illustrated in fig.2.10.

Figure 2.10: Valve-Barrel Connection

2.1.8. Barrel

The barrel has the task of keeping the projectile on a straight path during the launch and must be strong enough to withstand the propulsive pressure inside it without any deformation. For this reason the barrel is made of steel and has a thickness of 5 mm along its entire length. Typically impact test facilities able to perform bird strike tests require a gas gun with a large barrel [3], whose internal diameter ranges between 100 and 200 $[mm]$ and is from 3 to 10 $[m]$ long, depending on the type of test to be executed. A barrel with a wider cross section allows the pressure to act on a larger area generating a greater thrust, therefore large sections are more suitable for launching of heavier projectiles. Of particular importance is the surface finish of the inner walls of the barrel. In fact, even slight imperfections can trigger a longitudinal spin of the projectile inside the barrel [28], greatly complicating the dynamics of the motion and introducing unwanted stresses on the projectile itself. In addition, such surface imperfections also increase friction while reducing the overall efficiency of the system and thus the maximum achievable speed, which is why the barrel's inner walls shall be as smooth as possible.

The system's original barrel (fig. 2.11) was 9.15 $[m]$ long with an internal diameter of 150 $[mm]$.

Figure 2.11: Original Barrel

A longer barrel favors the achievement of higher speeds giving more time to accelerate the projectile, although in reality such acceleration isn't constant but decreases proportionally to the decrease of pressure as the projectile advances inside the barrel. On the other hand a shorter barrel decreases energy losses due to friction, considering both of these effects a trade-off was performed and a new barrel developed. Such new barrel, shown in fig. 2.12a is currently in use, it retains the same internal diameter (150 $[mm]$) but is shorter (7.5 $[m]$) with respect to the original one. Three special supports keep the barrel at a height of about two meters above the ground in order to test also large aircraft components. These supports (fig.2.12b) allow to move the barrel along its axle, once detached from the rest of the system. The projectile can then be loaded inside it before each shot. A gasket is inserted at the interface between the barrel and the valve to reduce gas leaks, before reconnecting the two parts.

(a) New Barrel (b) Barrel Supports

Figure 2.12: New Barrel Configuration

2.1.9. Stopper

The stopper (fig. 2.13) is a component mounted with tapered bars at the end of the barrel, the purpose of which is to separate the sabot from the surrogate bird. As a result of this separation the dummy bird must be able to continue its journey, passing through the stopper, and along the same trajectory given to the projectile by the barrel during the first stage of the launch. This operation is therefore particularly delicate and must be able to take place in a safe and repeatable manner. To ensure that this happens, at the impact with the stopper the sabot shall disintegrate in a controlled way, so as not to disturb the dummy bird and to generate a few debris (thus ensuring clear video recordings as well as accurate speed estimates).

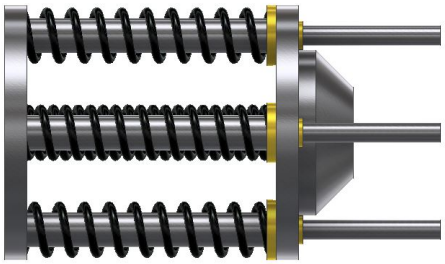

Figure 2.13: Stopper

With reference to the figure 2.13, it can be observed the presence of steel springs around the tapered bars, the purpose of which is to mitigate the force at the impact between sabot and stopper since such force tends to entirely discharge on the bars. Thanks to these springs instead the whole stopper can translate during the impact while compressing the springs, which can then safely release the stored energy without damaging or deforming the bars. From a geometric point of view the stopper is a perforated cone which in the past has been gradually perfected at the La.S.T. laboratory, changing its characteristic dimensions. Originally such piece was characterized by an angle with respect to the longitudinal axle of 30°, increasing which was observed an improvement during the separation phase. Currently the stopper in use (fig. 2.24e) has an angle of 45° and is slightly shorter w.r.t. the previous one.

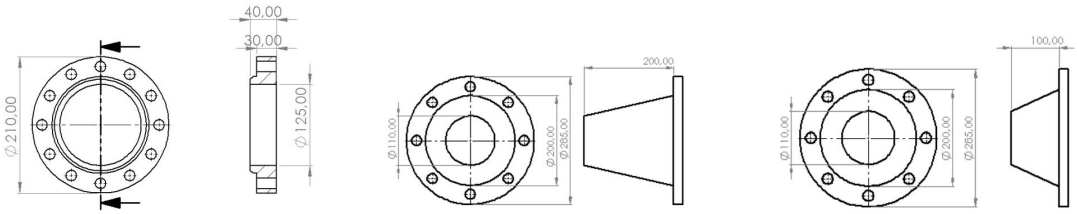

(a) Original Stopper (b) Old Stopper (c) New Stopper

Figure 2.14: Stopper Evolution

2.1.10. Target

Although the target cannot be properly defined as a part of the firing system, it's still an integral part of the ballistic firing range, since it represents the component against which the surrogate bird impacts. The target consists of an entirely steel plate (fig.2.15a), connected to a structure fixed to the ground (fig.2.15b) by means of three axial load cells(fig.2.15c), which allow to measure the impact force up to 20 tons. The position of

the target plate is adjustable in order to aim without the need of moving the entire cannon once the component to be tested has been placed. The target plate is 2.5 $[m]$ far from the cannon's mouth and it can also be set at different inclinations depending on the test specifications.

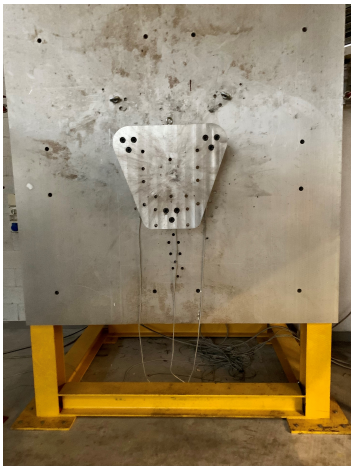

(a) Target Plate

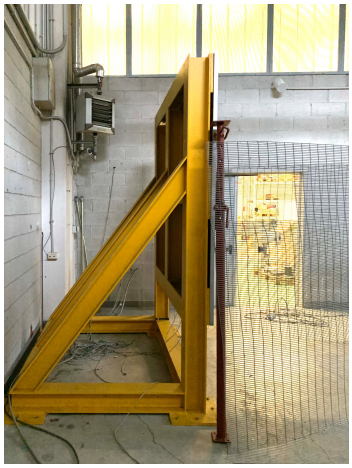

(b) Target Structure

(c) Load Cells

Figure 2.15: Target

2.2. Projectile

The projectile is the element that the launch system is designated to shoot at the target at the desired speed. Therefore, in bird-strike analysis, the projectile represents the bird impacting against an aircraft. The behavior of the projectile at impact depends on the maximum speed reached and can be of 5 kinds:

1. **Elastic:** an elastic impact occurs at low speeds and is such that the material remains in the elastic range: impact forces determine internal forces lower than the material's yield stress. Therefore the projectile doesn't rupture but is able to store elastic energy and subsequently release it during the rebound.

2. **Plastic:** increasing the speed, increased impact forces and internal stress above the yield one permanently deform the material which begin to behave plastically.

3. **Hydrodynamic:** at even higher speeds internal stresses become significantly higher than yield stress, resulting in very large deformations of the projectile. Impact response is no longer determined by the stiffness but by the projectile's density. This kind of impact was deeply studied by Willbeck and Barber [2] who stated how the projectile behaves like a fluid and can therefore be modelled accordingly to

hydrodynamic theory.

4. **Sonic:** occurs at or close to the speed of sound and involves the complete disintegration of the projectile, which can no longer be modelled according to hydrodynamic theory.

5. **Explosive:** at speeds above mach 1, the projectile assumes explosive behavior upon impact against the target.

In order to reproduce the bird-strike event in the laboratory, it's possible to employ two different types of projectile:

- Real Bird
- Surrogate Bird

2.2.1. Real Bird

The use of real birds as projectiles (fig.2.16) is a step required by the regulations for the approval and certification for all tested aircraft components. Conventionally in such homologation tests chickens are also used, which are killed just before testing in order to avoid *rigor mortis*. However necessary in some cases, the use of real birds has major disadvantages which have led to their use being limited to certification tests only. Beyond the clear ethical reasons, real birds also involve some practical drawbacks such as:

- **Increased time and cost of testing:** since the projectile disintegrates when impacting the target, the use of real birds requires extensive sanitization of the test range after each test.
- **Poor repeatability:** due to large differences in mass and anatomical characteristics between different birds, each test becomes intrinsically different from every other.

Figure 2.16: Real Bird Projectile

2.2.2. Surrogate Bird

The surrogate (or dummy) bird is a synthetic projectile that replicates the real bird's behaviour, and its impact forces, as faithfully as possible. Many studies have been carried out over the years to produce such a projectile, focusing on the material choice. In 2016, the SAE-G28 Commission was established [21] (in which Politecnico di Milano participated in 2017) whose purpose was to develop a qualified artificial bird material. Several tests were conducted using both real and surrogate birds in order to find similarities in the two responses. All tests, performed at various levels of complexity, are reported in the SAE AS6940 Aerospace Standard and led to the determination of material's properties and the geometry of the dummy bird:

Material Properties:

- Density = 0.95 $[g/cm^3]$
- Uniform texture
- Liquid enough to be poured into molds
- Stiff enough to be launched once solified

Geometry:

- Cylindrical shape
- Length-to-diameter ratio = 2

Accordingly to the identified criteria, the best solution for the dummy bird material is ballistic gelatin. At La.S.T. laboratory the elastomeric tissue simulant Perma-Gel® [1] (ρ=0.9 $[g/cm^3]$) was adopted for surrogate bird production (fig. 2.17), having it all the prescribed characteristics and having been specifically designed to simulate the consistency of internal organs and bones.

Figure 2.17: Surrogate Perma-Gel® Projectile

Perma-Gel® differs from other commonly used ballistic gelatin made out of animal jellies and water, since its composition is based on mineral oil and thermoplastic polymers. Depending on to the type of test to be performed, the mass of the surrogate bird may assume the values of: 1 $[Kg]$, 1.8 $[Kg]$ or 3.6 $[Kg]$.

2.3. Overview of Sabots

The sabot is an essential element in launch systems, designed to hold and deliver a projectile to a designated target. Since a launch system can generally be employed for several tests and therefore to fire different projectiles depending on the specific test, it's necessary to match the characteristic dimensions for different sub-caliber projectiles with the internal dimensions of the barrel. A sabot, suitably designed for a particular test, allows to perfectly accommodate a specific projectile inside the gun tube while ensuring the seal necessary to minimize high pressure gas leaks. These components have been extensively studied and perfected by the weapon and aeronautical industries over the decades and nowadays an extensive variety of sabot exist [15], depending on their specific application; the most relevant ones will be discussed below.

2.3.1. Functions of Sabots

The sabot must fulfill several functions, all equally important for the success of the experimental tests.

The sabot shall keep the bullet perfectly centered inside the barrel at all times, so as to confer the correct trajectory during the launch. As previously mentioned another relevant purpose of the sabot is to maintain the pressure seal, therefore acting as a moving gasket which ensures good performances. In addition, it's essential that the sabot is designed and manufactured in such a way as to effectively sustain the high loads that the sabot-projectile package undergoes during launch. Only this way it's possible to avoid unwanted damage to the projectile before its separation from the sabot. Once the stopper is reached the separation phase begins, during which a further purpose of the sabot is to open smoothly, leaving the projectile free and undisturbed.

2.3.2. Sabot's Configurations

As mentioned earlier, many different types of sabot exists nowadays, each designed for a specific application. However different, all existing sabots can be collected in two broad categories:

- **Pusher Type Sabot:**

Pusher type sabots completely enclose the projectile and are composed of two parts: pusher plate and side walls.

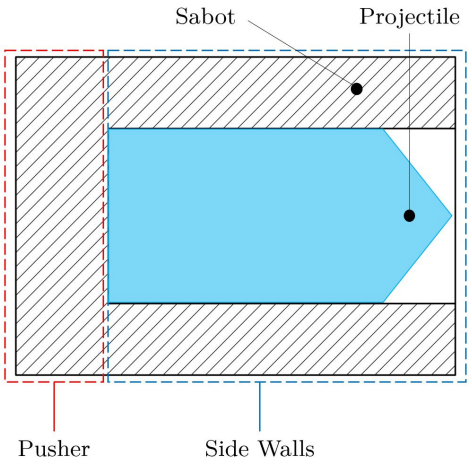

Figure 2.18: Pusher Type Sabot

The rear plate of the sabot, depicted in fig. 2.18, is called pusher and has the purpose

of supporting the pressure while accelerating the projectile as well as realizing the seal to prevent gas leakage. Side walls consist in an hollow cylinder, they're responsible for keeping the projectile in place and aligned with the launch line. Pusher type sabots are among the oldest and most widely used, characterized by a typical cup-like geometry which determines ease of production and a large use of material. Basic discarding sabot configurations [5] may present cuts along the side walls, divided into petals (fig.2.19a), in order to facilitate its separation. When the sabot exits the barrel aerodynamic forces act on the petals opening and deviating it from the line of launch (fig.2.19b). The same result can be obtained in a shorter range using a stopper.

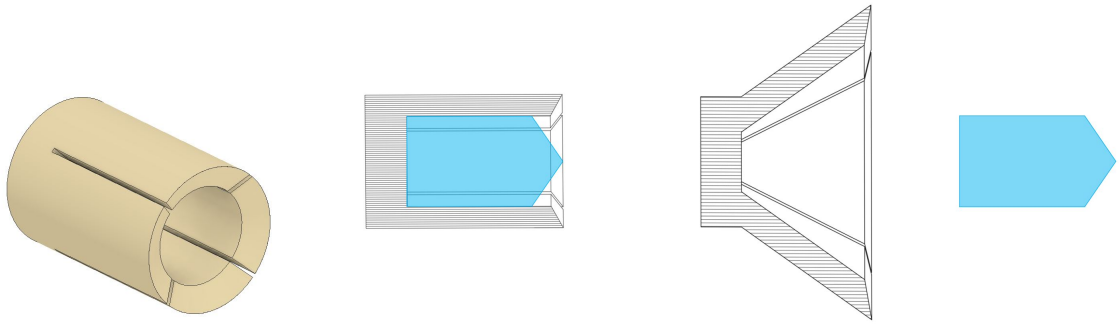

(a) (b)

Figure 2.19: Discharging Pusher Type

A further classification can be performed on the basis of the different shapes for the sabot's side walls, and therefore on how the driving pressure acts upon the sabot itself. Among various possible configurations, the most important ones are the Saddle-Back (fig.2.20a) and Double-Ramp configuration(fig. 2.20b). Such configurations are the result of research conducted by the US Army Ballistics Research Laboratory in 1978 [15], which allowed an advancement in the application of the finite element method for sabot design and they now represent industry standards.

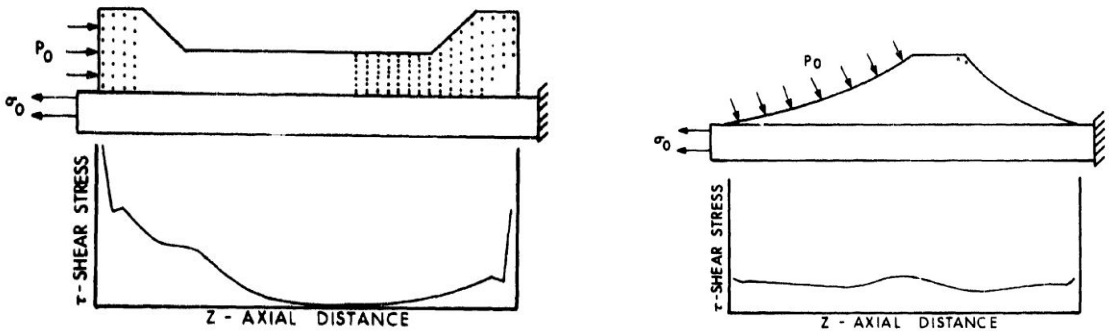

(a) Saddle-Back Configurations [15] (b) Double-Ramp Configuration [15]

Figure 2.20: Main Pusher Type Configurations

- **Puller Type Sabot:**

Puller type sabots are mainly employed in the weapons industry for testing kinetic energy and armor piercing projectiles [14], whose diameter is significantly smaller than the gun's bore. Unlike the pusher type, puller type sabot doesn't fully fill the gap between projectile and the barrel, leaving unsupported bow and stern of the bullet in order to minimize sabot's length. Puller type sabots typically consists of separate parts with few surfaces in direct contact with the inner cannon's walls. The result is an extremely light sabot, conventionally made of composite or poly-carbonate (PC), which allows to reach even supersonic speeds. Such sabot can have several geometrical shapes, generally consisting in wings or rings surrounding and supporting the projectile at its center of gravity. At launch, the sabot is able to pull the projectile (or model) thanks to a strong side-gripping (fig.2.21), or by interlocking grooves between sabot's and model's surfaces [22]. Since puller type sabots aren't usually whole rigidly connected pieces, at the exit from the barrel the sabot separation occurs and is entirely due to the effect of aerodynamic forces at high speeds.

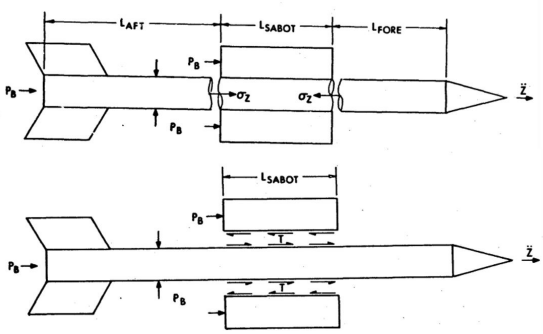

Figure 2.21: Side-Gripping Puller Type Configuration [14]

Since puller type sabots aren't usually whole rigidly connected pieces, at the exit from the barrel the sabot separation occurs and is entirely due to the effect of aerodynamic forces at high speeds, as shown in fig. 2.22:

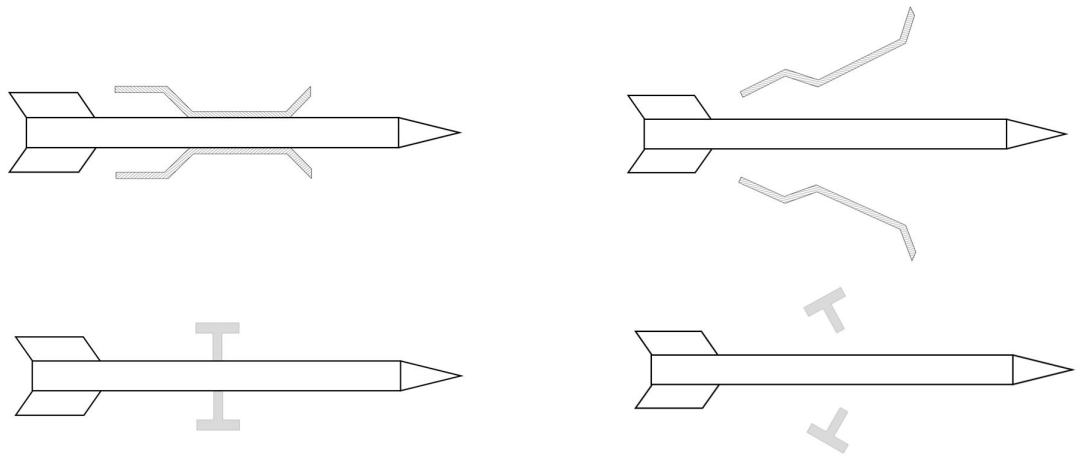

Figure 2.22: Discarding Puller Type

2.3.3. Sabot's Evolution

Over time, several sabots have been developed independently at La.S.T. laboratory, where they have been gradually improved to achieve better performances. Only pusher type sabots have been developed, since they are best suited for bird impact testing with a stopper-equipped launch system and a limited target range. Originally the materials used for sabot production consisted of Ciba (also known as Labelite, a high density expanded polyurethane); later on sabots in polystyrene were tested, as well as combinations of materials such as: Ciba + Balsa; Ciba + Polystyrene + Balsa. The most used material configuration was Ciba combined with some disks of Balsa as pusher plates. The sabot was composed of a series of disks, which were drilled to accommodate the dummy bird and then glued together to obtain the desired length. The number of wooden balsa discs, typically two or three, varied depending on the launch pressure value since their task was to absorb the first pressure wave.

Figure 2.23: Ciba+Balsa Sabot

These solutions have allowed good results to be achieved, however, due to the large number of debris generated by Labelite because of its brittle behaviour, it was decided to experiment the use of polyethylene PE300. PE300 presented a much higher ductile behaviour, leading to cleaner impacts, as well as much higher density ($\rho = 0.955$ $[g/cm^3]$) and mechanical properties. Sabots made of PE300 were very cost effective but they required a long time to be internally milled at La.S.T. laboratory. The next step in the sabot's evolution was performed considering thermoplastics as new production materials. Thermoplastics retain the advantage of having a high ductility while having a very low density with respect to the PE300, their density is indeed comparable with Ciba's density ($\rho = 0.275$ $[g/cm^3]$). Thermoplastics gave significant improvements in both terms of performance and debris generation, therefore it was opted for their realization inside the La.S.T. laboratory by means of 3D printing. The ability to print the sabot allowed to test different thermoplastics with mechanical properties increasingly suited to their application, such as: Polylactic acid (or PLA) and High Impact Polystyrene (or HIPS).

(a) Ciba

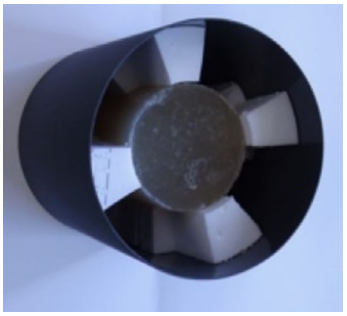

(b) Polyethylene

(c) PE300

(d) PLA

(e) HIPS

Figure 2.24: Sabot Evolution

3 | Sabot Design

This chapter presents the full design process developed to realize a new sabot. The definition of the projectual requirements is provided at first, followed by a detailed description of the design architecture alongside with a distinction between preliminary and optimized designs. The way design principles are determined as the project's guidelines is then presented, and each one of them is further investigated. Afterwards the focus is shifted toward the forces acting on the sabot as an additional tool to guide the design, leading to multiple alternative geometries. Lastly, all obtained preliminary designs are proposed.

3.1. Design Process and Requirements

As previously stated, the sabot is a component whose main task is to support the surrogate bird during the entire duration of the shot, up to the moment of their separation. The sabot must therefore withstand the high pressure and strong acceleration to which it is subjected, ensuring at the same time that the highest speed is reached.

It is therefore possible to determine the design requirements for the sabot, essential for a successful ballistic test:

- To reach the highest achievable speed while maintaining its structural integrity
- To generate none to little debris, allowing a clean separation from the dummy bird
- To confer a good attitude to the surrogate bird

Besides from reaching higher speeds, main objective of this work, both remaining requirements are equally important and must be taken into great consideration when developing a new sabot. Debris generation is an undesired effect, deriving from the sabot's fragmentation at the moment of its collision with the stopper, as it negatively affects the quality of high speed cameras' recordings, compromising the reliability of speed measurements. Furthermore such debris can disturb the dummy bird separation from the sabot itself and they represent a potential danger for delicate instruments placed in the ballistic test range (see Section 4.3.1). The attitude of the surrogate bird is another important aspect, as it

is desired for the sabot to always keep it perfectly centered inside the gun's barrel during the shot and to maintain a straight trajectory when exiting it. Only this way it will be possible for the dummy-bird to correctly pass through the stopper and to hit the target in a precise and repeatable way. Any misalignment or variation in the surrogate bird's trajectory would indeed lead to its disintegration against the stopper.

Achieving the optimal design, such that it meets all design requirements, is neither a straightforward process nor has it always been obtained. Most of the time a design that proves to be satisfactory is not simply a product of calculations, but requires a development phase which involves numerical simulations supported by experimental tests. Depending on the results of simulations and tests, it might be necessary to make changes to the preliminary design. Then the procedure is re-iterated, thus optimizing the original sabot's design until it meets the requirements identified above.
A strong inter-dependence therefore emerges between different phases of the sabot's design, leading to the development of an *ad hoc* engineering process. The obtained design process for the sabot is illustrated in fig. 3.1, which summarizes all steps and decisions made in the process of realizing a new sabot. It is hereby noted that such design process contains the following 7 fundamental activities:

1. **Determination of all design requirements**: (Block 1 of fig.3.1) previously identified and essential to establish the needs of the product.
2. **Identification of design principles** : (Block 2) once all design requirements have been determined, it is necessary to identify the design principles. These principles represent the main guidelines for the realization of a more efficient sabot, in terms of maximum reached velocity, with respect to those developed in the past. The choice of these design principles is based on some considerations resulting from an energy balance which will be conducted in the following section.
3. **Establishing criteria to evaluate different designs**: (Block 3) all produced alternative preliminary designs will need to be evaluated by means of specific criteria defined and discussed in chapter 4.
4. **Performing preliminary designs**: (Block 4) more tentative or preliminary designs are generated with the aim of obtaining a prototype to be tested.
5. **Evaluation of preliminary designs**: (Block 5) to compare all generated alternative designs with previously established specific criteria employing numerical simu-

lations and, when necessary, making changes to the preliminary design (Block 5A) subsequently repeating earlier steps (of Block 4, 5, 5A).

6. **Prototype production**: (Block 6) once a winning design is developed, it's possible to proceed with the realization of its prototype. The construction procedure and its limitations are addressed in 4.

7. **Prototype testing**: (Block 7) the final design activity is to assess the new sabot's performances through experimental tests. If obtained experimental results are satisfactory, then the sabot's final design is reached.

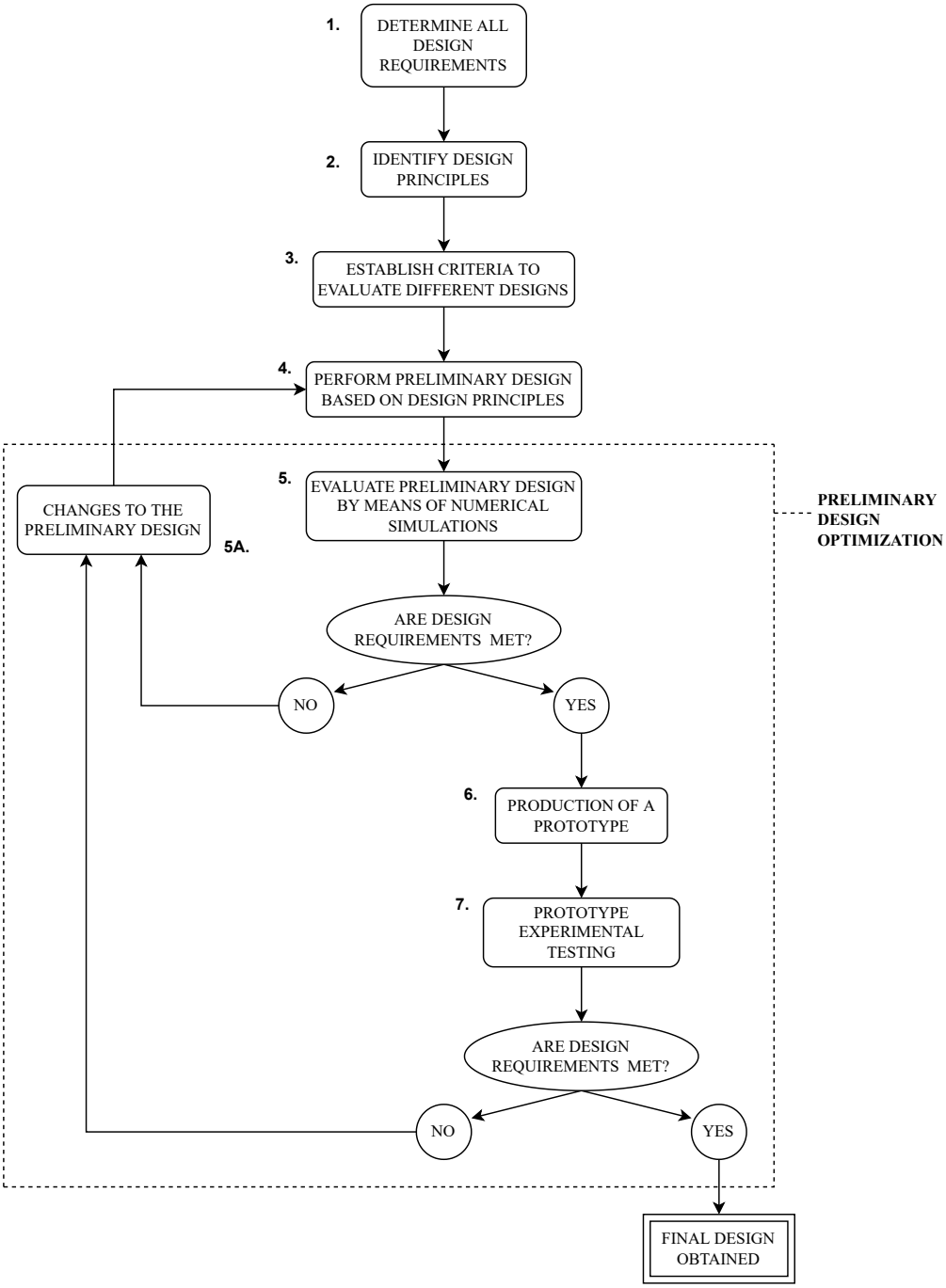

Figure 3.1: Sabot's design process flowchart

Whenever results gathered from the numerical or experimental tests turn out to be partially or entirely unsatisfactory, a re-design of the sabot is performed in order to achieve better and better outputs, up to the final design. While this is an integral part of the design process, it has been treated separately as a preliminary design optimization procedure, covered in chapter 4. For this reason all changes made to all alternative preliminary designs in this chapter are attributable and referenced to the sabot's optimization phase. Following the design flowchart displayed above, it is also possible to easily assess the correlation level between numerical simulation and experimental tests. In fact, if from both the numerical model and laboratory tests emerges that a certain design meets the project requirements, then it can be affirmed that a good correlation level has been achieved and therefore the numerical model used is valid. Similarly it can be said that there is no correlation between the developed numerical model and the experimental test, should the former prove that a preliminary design satisfies the requirements, while the latter proves the opposite. In the latter case it will be necessary to improve the quality of the numerical simulation in order to better model the real behavior of the sabot during the shot.

3.2. System's Energy Balance

The following analysis was carried out with the sole purpose to evaluate the efficiency of the existing launching system by adopting an energy-based approach. From a purely energetic point of view it is possible to estimate the energy which is dissipated during the firing of a bullet, allowing us to better understand what the effective margins for the *system*'s improvement are. Once it has been determined where the *system* can be improved, it will be possible to proceed with the identifications of all design principles which will guide the development of a new sabot. The system which is considered in this section is given by the projectile: defined as the set of both sabot and surrogate bird.

Hypothesis:

- The pressure applied to the projectile is assumed to be constant for the entire duration of the shot, until the projectile exits the gun barrel.
- Projectile's motion inside the cannon's barrel is given by a pure rigid translation.

The first formulated hypothesis represents a substantial approximation with respect to the real case: it is known that the true trend of the pressure inside the gun barrel is not constant. The pressure propelling the projectile during its firing will be maximum when the fast-acting valve opens and will tend to reduce as the volume occupied by the

pressurized gases increases (i.e. it reduces as the bullet advances inside the barrel of the gun). Likely, this hypothesis will lead to an estimate of an exit speed and final kinetic energy of the projectiles slightly higher than the real one. Also, assuming a constant pressure applied to the sabot during its design entails an oversizing of the piece, as it would be subject to higher loads than those actually applied. However, since there is yet no instrumentation providing a pressure curve inside the cannon during launch and given that the phenomenon of the shot is extremely rapid, it is acceptable to adopt such a conservative approach.

The second hypothesis consists in neglecting any possible spin that the projectile could undergo during its accelerated motion. It is possible for the projectile not only to rigidly translate, but also to rotate about its longitudinal axis when traveling inside the gun's barrel. Such spin would lead to the generation of centrifugal loads acting on the *projectile* and to a consequent increment of friction forces between the sabot and the barrel's internal walls. Still this motion has never been observed in any of the conducted firing tests (reported in chapter 5), so from the experimental evidence it is safe to ignore any centrifugal load and to assume a pure rigid translational motion.

Once these assumptions have been formulated, it is possible to proceed by applying to our system the principle of work and kinetic energy (also known as the work-energy theorem). This principle can be directly derived from Newton's second law and states that:

"*The work done by the resultant of all forces acting onto a body is equal to the variation of the body's kinetic energy.*"

Its analytical formulation is:

$$W_p = \Delta E_k = \frac{1}{2} \cdot m \cdot V_f^2 - \frac{1}{2} \cdot m \cdot V_i^2 \tag{3.1}$$

Where W_p is the work performed by the net force acting on the body, ΔE_k is the variation of kinetic energy, m is the body's mass, while V_f and V_i are respectively the body's velocities at the considered final and initial time instants. In the problem under consideration, the body is indeed the *projectile*, to which energy is provided by the applied pressure. In the case of constant pressure during the shot, the work done by the pressure forces is given by:

$$W_p = P \cdot A \cdot l \tag{3.2}$$

Where: P is the exerted pressure on the *projectile*, A is the *projectile*'s equivalent area upon which the pressure acts, and l is the traveled distance (a.k.a the barrel's length). The work-energy theorem reported in equation 3.1 refers to the ideal case in which there isn't any kind of energy loss. In reality however, not all provided energy is transformed into a variation of the *projectile*'s kinetic energy, as dissipative phenomena are also present. The main dissipative phenomena which occur during the firing of the *projectile* are:

- Sliding Friction
- Aerodynamic Drag

Even if the projectile has no spin, there will always be a loss of energy due to sliding friction. This energy disperses in the form of heat at the interface between the contact surfaces of the sabot and the internal walls of the barrel, and is directly proportional to the dynamic friction coefficient characteristic of these surfaces' materials. Similarly, part of the lost energy is due to the viscous friction between the projectile and the air around it. During its strong acceleration, aerodynamic resistance is generated and the resulting aerodynamic drag force tends to slow the projectile down and is proportional to the square of its speed. The determination of how much energy is lost due to friction and how much due to aerodynamic drag is not an easy task. Considering the complexity of the sabot's geometric shape, evaluating the aerodynamic resistance acting on it is not immediate and would require a full Computational Fluid Dynamics (or CFD) analysis. Furthermore, the material of which the sabot is made can deform, while remaining in the elastic range, as a result of the strong loads to which it is subjected. Likely this would lead to the sabot pressing against the barrel's internal walls and thus increasing friction forces. Therefore, for the sake of simplicity, the overall dissipated energy is indicated as:

$$E_D = E_{D\,friction} + E_{D\,drag} \tag{3.3}$$

In the presence of such energy losses the energy balance must be reformulated starting from the work-energy theorem of equation 3.1 as follows:

$$W_p = \frac{1}{2} \cdot m \cdot V_f^2 - \frac{1}{2} \cdot m \cdot V_i^2 + E_D \tag{3.4}$$

At this point, substituting expression 3.2 into equation 3.4 and considering the *projectile*

at rest at the initial time instant ($V_i = 0$), the total dissipated energy can be evaluated:

$$E_D = P \cdot A \cdot l - \frac{1}{2} \cdot m \cdot V_f^2 \tag{3.5}$$

Now, taking as reference the latest of the old sabots and its experimental test (whose results are reported in chapter 5), all relevant data is hereby reported:

Old sabot's mass: m_{sabot} $[Kg]$	0.457
Dummy-Bird's mass: m_{bird} $[Kg]$	0.982
Projectile's mass: m $[Kg]$	1.439
Sabot's Area upon which pressure acts: A $[m^2]$	0.01744
Barrel's length: l $[m]$	7.5
Firing pressure: P $[Pa]$	$7 \cdot e^{+5}$
Final projectile's velocity: V_f $[m/s]$	226

Table 3.1: Energy Balance Reference Data

The energy balance for the real case can be performed, thus considering the presence of all dissipative phenomena as per equation 3.5:

Provided Energy to the Projectile: W_p $[KJ]$	91.560
Projectile's final Kinetic Energy: E_{kf} $[KJ]$	36.749
Total Dissipated Energy: E_D $[KJ]$	54.811

Table 3.2: Energy Balance

With respect to the ideal case the *system*'s efficiency η can then be defined in terms of energy as:

$$\eta = \frac{Projectile's\ Kinetic\ Energy\ Variation}{Provided\ Energy\ to\ the\ Projectile} = \frac{\Delta E_k}{W_p} \tag{3.6}$$

As previously mentioned, in the ideal case all energy provided to the projectile would be translated into a variation of the projectile's kinetic energy ΔE_k, the energy balance would simply be given by equation 3.1, and the *system*'s efficiency would be: $\eta = 1$. Evaluating the projectile's final velocity in such instance, it would be equal to: $V_f = 356$ $[m/s]$ (higher than the speed of sound in dry air at 20°C). Instead, considering energy losses, the efficiency of the system drops to $\eta \approx 0.4$, meaning that in the real case more than half of the work done by the pressure is dissipated as a result of friction and aerodynamic resistance.

It should be noted that this energy balance is purely indicative, due to the strong assumptions on which it is based. Reminding how the true pressure trend is not constant but decreases in time, the effective W_p will be lower than the one estimated above and therefore the true efficiency η can be expected to be greater. A more realistic estimate of the theoretical velocity is given by the simplified formula:

$$V_f = \sqrt{\frac{P \cdot A \cdot L}{m}} \tag{3.7}$$

Nevertheless from this energy balance, however approximate, some meaningful considerations are drawn. Looking at equation 3.4, parameters on which it's possible to intervene from early design stages in order to maximize the projectile's V_f, are identified. It is evident how increasing the launch pressure P would provide more kinetic energy to the system, although this involves subjecting the sabot to greater loads and inducing a significant state of stress in its material. Since structural integrity is a key prerequisite for successful experimental testing, increasing P requires adequate stiffening of the sabot, which often leads to an increase in mass. As already said, the mass of the bullet is constituted by the dummy-bird and the sabot, being the first not alterable as established by certification standards (see section 2.2). On the other hand, sabot's mass is certainly a modifiable parameter which is preferably minimized during the design in order to reduce weight as much as possible. It is therefore clear that a trade-off between launch pressure and sabot mass must be achieved, bearing in mind also the limits of the launching system, which cannot reach indefinitely high pressures. Another parameter on which it's possible to intervene is the dynamic friction coefficient μ_d between contact surfaces: employing materials with low values of μ_d in fact would lead to reduce sliding friction forces. Starting from these considerations it's possible to proceed identifying all design principles for the development of the new sabot.

3.3. Sabot Design Principles

In this section all the assumptions that should be stated before undertaking the design of the sabot and its structural analysis are reported. The design principles on which the design is based, and their respective application, are then illustrated.

3.3.1. Assumptions and limitations

The design process which is about to be performed, considers the first stage of the ballistic test, concerning the in-bore motion of the projectile (described in subsection **??**). During this stage on the sabot act inertial loads, contact forces at its walls, pushing load due to high pressure, aerodynamic and gravitational forces. Among all these loads the most significant ones are inertial and pressure forces, as the acceleration imparted onto the projectile is extremely strong. Since these forces are much higher than the aerodynamic loads arising within the barrel, the latter ones are neglected.

A subsequent assumption concerns the effect of temperature on stress analysis. Although it is true that during the firing friction is present and is such as to generate heat at the contact surfaces between sabot and barrel, the reached temperatures are contained. All the more so considering that the sabot is lapped by cold air (whose temperature ranges between 15°C and 20 ºC), the heat dispersion by convection is extremely rapid. Keeping also in mind the short duration of the motion inside the cannon (a few milliseconds) the thermal effects are neither intense nor durable enough to induce any degradation of the sabot's mechanical properties. It is therefore reasonable to neglect all such temperature-related effects.

To the assumptions stated so far are added the two hypotheses previously formulated when performing the energy balance: the sabot is assumed to have no rotational motion inside the barrel (thus no centrifugal loads acts on it) and the applied pressure is taken as constant. Since it is difficult to determine the dynamic effects taking place inside the cannon, it is considered appropriate to maintain a conservative approach and to treat the pushing pressure as a static load. Moreover, being such load applied in a very short time, it is treated as an impact loading.

Looking at all above limitations, it may seem that system modeling is being oversimplified. Although, considering the magnitude of the loads involved, an excessive accuracy, however desirable, is not strictly necessary. It is also reminded how the adoption of this conservative approach allows to oversize the sabot, reducing the possibility of its failure during experimental tests. In addition, the design process requires many re-iterations and re-designs related to the optimization phase, so a simpler model is auspicable in order to perform more iterations and to save on computational costs. Satisfactory results can be achieved applying these assumptions, while a more detailed model would presumably

lead to slightly better results at a much higher cost.

3.3.2. Mass Reduction

Mass reduction is one of the fundamental principles on which the design of the sabot is based. According to Newton's second law of motion, if a body has a net force F acting on it, it is accelerated as in equation 3.8, being m the body's mass and a its resulting acceleration:

$$F = m \cdot a \tag{3.8}$$

So applying the same load, greater accelerations are expected for lower masses. The same conclusion can alternatively be drawn from equation 3.1 of the energy balance. Exploiting the work-energy theorem, by virtue of the principle of energy conservation, the energy W_p supplied to the body must be equal to the variation of its kinetic energy ΔE_k at all times. Therefore, by decreasing the mass m of the *projectile*, its final speed V_f must necessarily increase so that ΔE_k remains constant.

However, achieving the minimum mass goal is not immediate: generally engineering steps taken to reduce the sabot's weight may increase stress and deformation in its material []. If the generated stresses and deformations are too high, it is more likely for rupture to occur during the shot.

Mass Reduction Objective:

Objective of the mass reduction process is to produce a sabot design concept as light as possible which still meets the structural integrity requirement.

Initial and Boundary Conditions:

Mass reduction procedure shall start from a reference geometric shape and from an initial mass value. All projects for the new sabot should have a lower value of mass with respect to such initial value. The sabot in fig. 3.2 was chosen for its success in past tests and is therefore taken as a starting point. This sabot is the same one used to perform the energy balance, it will be referred to as "S_{00}" during all following design stages and is hereby reported for completeness along with its mass and characteristic dimensions.

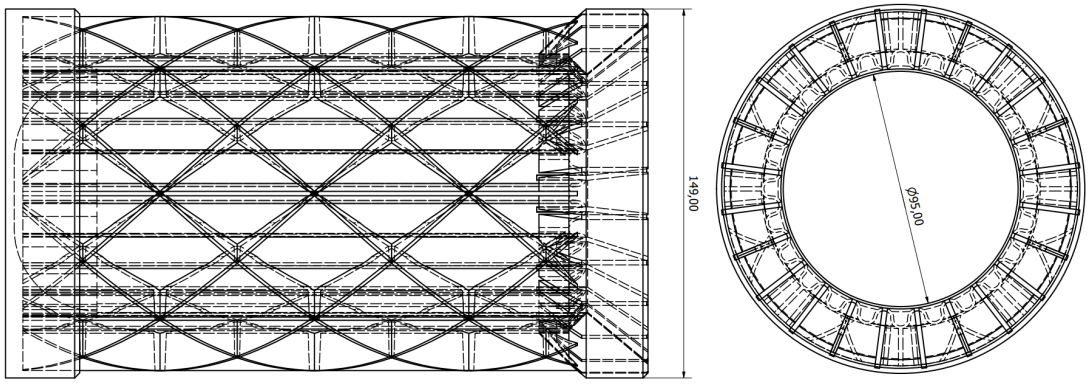

Figure 3.2: Sabot 0.

Length $[mm]$:	Inner Diameter $[mm]$:	Outer Diameter $[mm]$:	Mass $[g]$:
262	95	149	460

Table 3.3: Sabot 0 Reference Values

Design boundary conditions are of a purely geometric nature. The new sabot must be able to properly house the surrogate bird and to correctly slide inside the barrel. To be loaded into the cannon the sabot must necessarily have a clearance fit (fig.3.3a) with the bore's inner walls. It would be preferable to minimize sabot's outer diameter in order to reduce its mass, but excessive clearance would increase air leakage and compromise one of the primary functions of the sabot: to keep the projectile on a precise trajectory. Since the gelatin surrogate bird can be compressed when inserted into the sabot, the sizing of the latter can foresee an interference fit (fig.3.3b). Taking the sabot's nominal inner diameter smaller than the dummy bird's one ($\approx 97\ mm$) is a design choice aimed at preserving the reference inner dimension of sabot S_{00} and it is also found to be a mass-efficient solution. On the other hand an excessive interference with the surrogate bird may damage the sabot and lead to a not optimal separation or even to sabot failure during launch. These limitations result in boundary conditions on the sabot's volume, to respect which appropriate tolerances are defined for the inner and outer sabot's diameters:

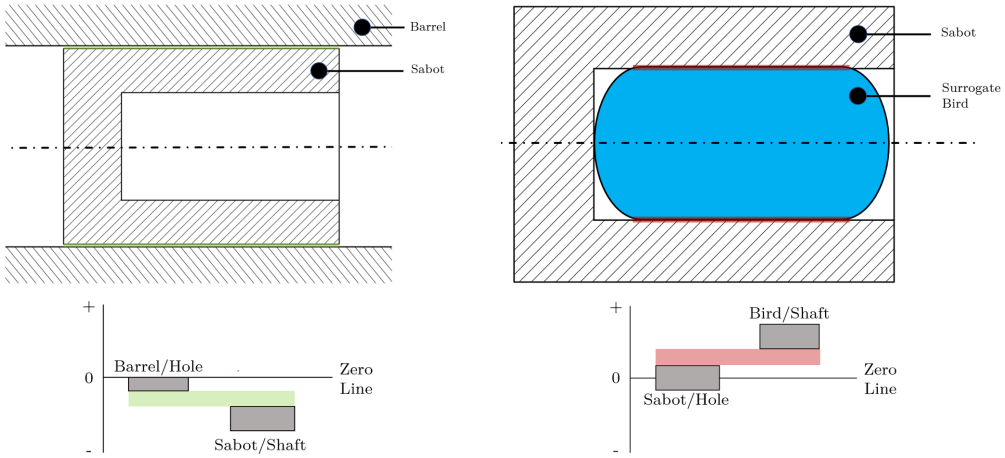

(a) Clearance Fit (b) Interference Fit

Figure 3.3: Sabot-Barrel and Sabot-Surrogate Bird Fits

Resulting designs' initial and boundary conditions are summarized in the following table:

Initial Condition:	
Initial Mass Value $[g]$	460
Boundary Conditions:	
Sabot's Outer Diameter $[mm]$	149 ± 0.5
Sabot's Inner Diameter $[mm]$	96 ± 1.0

Table 3.4: Initial and Boundary Conditions

Iterative Approach:

Once the objective and conditions have been defined, an iterative approach cite to minimize mass can be implemented. From the early design stages a weight-efficient structure for the sabot can be found exploiting the scheme shown in fig.3.4.

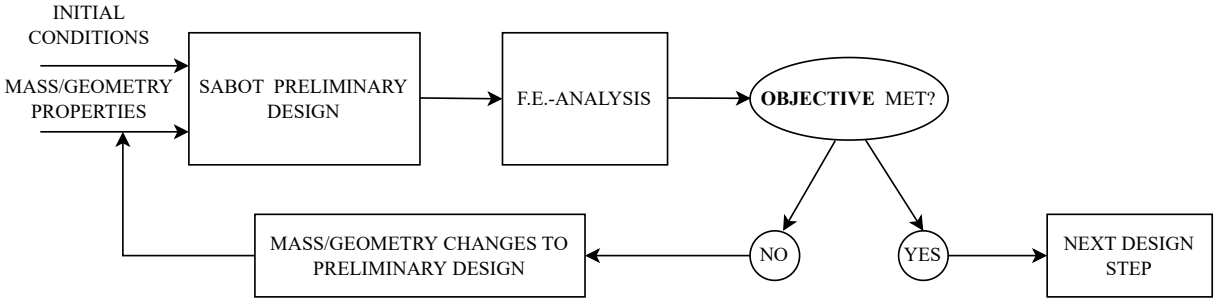

Figure 3.4: Iterative mass reduction

To verify whether a preliminary design achieves the mass reduction's objective, it is necessary to carry out a structural analysis by developing a finite element model (FEM) for the sabot and simulating the firing of both sabot and projectile. A preliminary design meets the defined objective if and only if numerical outputs show that such concept is able to withstand the applied loads with contained deformations and without any failure. A detailed description of all conducted finite element analyses is provided in chapter 4, section 4.1. Then the idea on which the mass reduction procedure is based is that exists a minimum mass sabot which can work properly. Such ideal sabot design is identified as the **Optimal Solution:** the minimum mass design which guarantees the structural integrity of the sabot during launch. So whenever a preliminary design turns out to be unsatisfactory from F.E. analysis, a new one is developed modifying the previous one's structural geometry or adding mass in order to strengthen critical areas. The resulting feedback procedure corresponds to the global design process' inner loop (of fig. 3.1), being mass reduction closely linked to the preliminary design optimization phase through numerical simulations. The ideal trend of the iterative mass reduction process is illustrated in fig.3.5

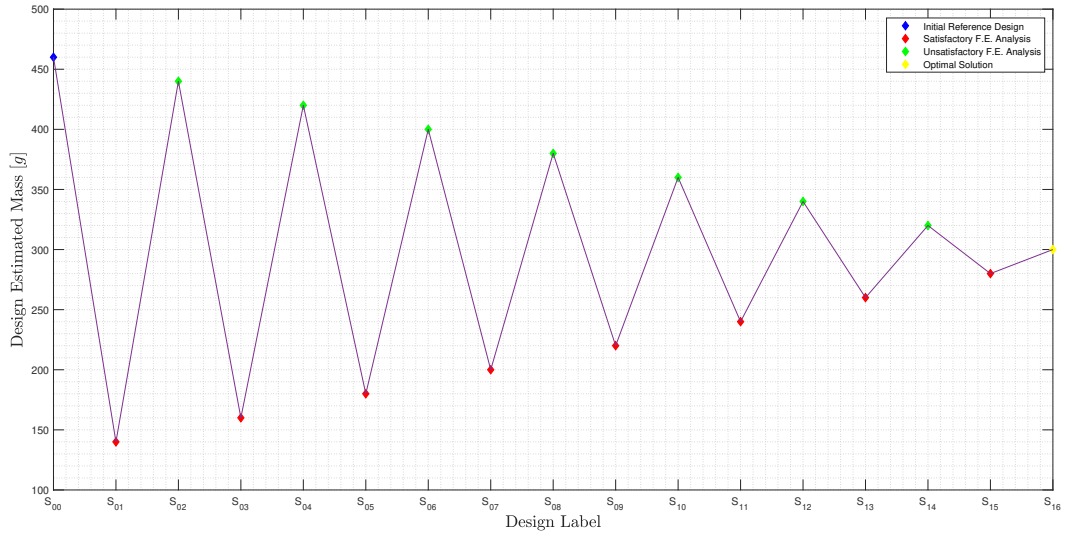

Figure 3.5: Ideal Iterative Mass Reduction Process

This methodology allows to make targeted changes at a time to the original preliminary design, converging towards the optimal solution. Generally such optimal solution is only reachable through a high number of iterations, in the real application a satisfactory result can be achieved by getting close enough to this ideal design. In the real case the optimal solution will lie within a certain mass range, between the last design with a successful

FE-Analysis and the latest unsuccessful one. The lower this mass range is, the better the obtained design will be in terms of mass with respect to the optimal solution. Overall, during this thesis work, 11 preliminary designs were developed following this methodology, each with different mass and structural elements. All preliminary design have been labeled as "S_i" (with "i" ranging from 01 to 11) and results for the performed mass reduction process are presented in chapter 5.

3.3.3. Material Choice

The material from which the sabot is made has great influence on its performance. As a matter of fact its density affects the sabot's mass and therefore a careful choice of the material collaborates with the mass reduction process in order to obtain a sabot as light as possible. This choice, however, is not limited only to considerations based on the mass, in fact the parameters to be considered when looking for a good material are:

1. Low density
2. High mechanical properties
3. Low friction coefficient
4. Ductile behaviour
5. Good machinability
6. Low cost

For high mechanical properties it is intended that the material should have high Young's Modulus E and high yield strength σ^y to resist the strong acceleration which will be imparted onto the sabot, since it's essential for this component to maintain its structural integrity until its collision with the stopper. As explained in section 3.2 one way to improve sabot's performances is to reduce as much as possible kinetic energy dispersion due to friction, so the employing materials with low coefficients of friction helps in this regard. Debris generation is an undesired effect of the collision between the stopper and the sabot as it negatively affects the quality of high speed cameras' recordings, compromising the reliability of speed measurements and disturbing the dummy bird separation from the sabot itself. Therefore it is preferable to use a material which doesn't exhibit a brittle behavior, but instead a ductile one with a high value of plastic deformation at failure. Good machinability is also an important aspect to take into consideration: once designed, the sabot will be realized with a 3D Printer (see section 4.2) whose extrusion nozzle can only reach temperatures within 250 °C, so it's crucial to select a material which doesn't

have an excessively high melting point. Finally, cost efficiency was also taken into account. All these parameters constitute selection criteria to identify the best material. Since the sabot must be as light, ductile and cheap as possible, the material choice can be narrowed down to thermoplastics.

HIPs: High Impact Polystyrene

High Impact Polystyrene (also known as HIPs) is a thermoplastic material consisting of polystyrene and styrene-butadiene rubber (or SBR rubber). From the molecular point of view (fig. 3.6) HIPs is an amorphous copolymer obtained by grafting, as such its polymer chains lose cohesion with heat and fluidify. This allows the material to be processed very easily by means of low cost technologies, exhibiting excellent dimensional stability. Once the material is solidified it retains good mechanical properties and can be employed in both structural and low heat applications as long as it doesn't exceed its glass transition temperature.

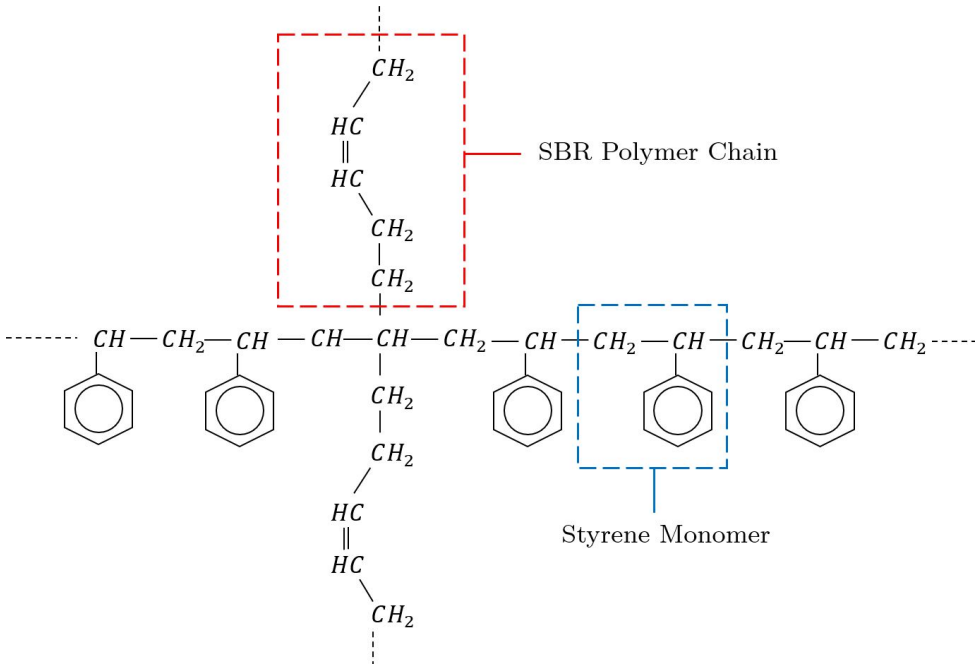

Figure 3.6: HIPs' Molecular Composition

Compared to common polystyrene (or PS), the presence of SBR elastomer confers to this material some peculiar properties which are particularly suitable for the realization of the sabot:

- Lower density
- Greater impact resistance

- Greater elongation at break

Overall HIPs reflects all designated requirements for the sabot, in particular the advantages of HIPs lie in its low density and in its high elongation at break, letting the material assume the desired ductile behavior. Furthermore previous experimental tests conducted at La.S.T. laboratory have shown that HIPs exhibits a clearly superior behaviour with respect to other materials used for the production of old sabots (see chapter 2, section 2.3). In the light of these excellent characteristics and of past experience, it was decided to continue to use this material for the realization of all new sabots' prototypes developed in this thesis work. On the other hand, high impact polystyrene is not perfect: some of its mechanical properties appear to be slightly worse when compared to pure polystyrene, such as:

- Lower Young's modulus
- Lower flexural strength
- Lower aging resistance

To have a quantitative indication of the difference between HIPs and polystyrene, respective values for their main mechanical and physical properties are given in the table below:

	High Impact Polystyrene (HIPs)	Polystyrene (PS)
σ^y [MPa]	21	39.3
E [MPa]	1550	3250
ε_{rott} [%]	42.0	4.0
ρ $[g/cm^3]$	1.04	1.2

Table 3.5: HIPs-PS Comparison

The above values for HIPs refer to the material technical datasheet from the supplier FormFutura®, which provided the 3D printing filament actually used for the sabot production. Therefore such values will be also taken as reference when creating the sabot's numerical model.

However, besides HIPs, a large variety of 3D printable thermoplastics exists, each with different properties. With the intent of investigating other potentially suitable materials for the realization of the sabot, a dedicated algorithm based on MCDC (Multi-Criteria Decision Making) methods has been implemented in Matlab® in order to easily compare multiple alternatives.

MCDM: Multi-Criteria Decision Making methods

Multi-Criteria Decision Making methods [36] are a prominent class of approaches for optimal decision making, widely adopted to solve problems in many engineering applications. The typical MCDM problem deals with the evaluation of a set of alternatives in terms of a set of decision criteria. There are three steps in utilizing any decision-making technique involving numerical analysis of alternatives:

1. Determining the relevant criteria and alternatives;
2. Attaching numerical measures to the relative importance of the criteria and to the impacts of the alternatives on these criteria;
3. Processing the numerical values to determine a ranking of each alternative;

There are many MCDM methods which can be utilized or not depending on the specific case, each of these methods uses slightly different numeric techniques to help decision makers choose among a discrete set of alternative decisions, but in all methods this is always achieved on the basis of the impact of the alternatives on certain criteria. Such methodology has been applied to the specific case study of the sabot's material choice and is hereby described step by step.

STEP 1: Determining the relevant criteria and alternatives

In order to identify the optimal material the criteria to be considered, as mentioned in subsection 3.3.3, are:

σ^y [MPa]	Yielding Stress
E [MPa]	Young's Modulus
ε_{rott} [%]	Plastic Deformation at Failure
ρ $[g/cm^3]$	Density
T [°C]	Extruder's Nozzle Maximum Temperature
μ	Friction Coefficient on Dry Steel
C [€/100 g]	Cost

Table 3.6: Decision Criteria

All above criteria are listed in order of importance since it's essential for the sabot to have high mechanical properties, preferably using a light and easily machinable material. Low friction coefficient and cost were taken as the least relevant parameters. The alternatives are given by all considered materials, so a database including a wide range of thermoplastics with their respective decision criteria was compiled as to choose the best one among

them.

STEP 2: Attaching numerical measures to the relative importance of the criteria and to the impacts of the alternatives on these criteria

To compare various alternatives it's necessary to attribute a numerical value to each decision criteria, representing one criterion's importance with respect to all others in the decision-making process. Such values are defined by the following scale of relative importance:

Value	Definition
1	Equal importance
3	Moderate importance
5	Strong importance
7	Very strong importance
9	Extreme importance
2,4,6,8...	Intermediate values
1/2,1/3,1/4...	Inverse comparison values

Table 3.7: Scale of relative importance

By assigning a numerical value to every criteria, accordingly with the scale of relative importance, a pairwise comparison matrix (or PWCM) is obtained:

	σ^y	E	ε_{rott}	ρ	T	μ	Cost
σ^y	1	2	3	2	6	5	7
E	1/2	1	2	1	4	4	5
ε_{rott}	1/3	1/2	1	1/2	3	3	4
ρ	1/2	1	2	1	3	2	4
T	1/6	1/4	1/3	1/3	1	1/2	2
μ	1/5	1/4	1/3	1/2	2	1	2
Cost	1/7	1/5	1/4	1/4	1/2	1/2	1

Table 3.8: Pairwise Comparison Matrix

All the elements of the PWCM have been assigned in such a way to give higher importance to density and mechanical properties of the material, intermediate importance to T and μ criteria, while the cost was considered as the least relevant parameter.

STEP 3: Processing the numerical values to determine a ranking of each alternative

Having defined all criteria, alternatives and the PWCM, the problem only consists in ranking such alternatives in terms of their total preferences when all decision criteria are

considered simultaneously. To carry out this last step, two further tools are used:

- **The Analytic Hierarchy Process (or AHP)** [35] :
  "The AHP is a decision support tool which can be used to solve complex decision problems. It uses a multi-level hierarchical structure of objectives, criteria, and alternatives." The data on which this tool operates are extrapolated from the PWCM through sets of pairwise comparisons. From these comparisons weights of importance for all decision criteria are derived and therefore also relative performance measures for various materials (or alternatives) can be obtained in terms of the calculated weights. The AHP tool also provides a mechanism to check the consistency of the PWCM, making sure that there are no logical conflicts in the previous assignment of relative importance to each criteria.

- **The Weighted Sum Model (or WSM)** [36] :
  The weighted sum model is one of the most commonly used approach, it provides a score indicative of the performance of each alternative thanks to which it's possible to develop a ranking. For an optimization problem with m alternatives and n criteria, the best alternative is the one that satisfies the following expression:

$$BPS = max_i(\sum_{1}^{n}{}_i CW_i \cdot NV_i) \qquad \textit{for i=1,2,3... m} \qquad (3.9)$$

In order to compute the criteria weights by means of the AHP process, the PWCM must first be normalized: each element of the matrix is divided by the sum of the elements belonging to its own column. Once the PWCM has been normalized all criteria weights, whose sum must be equal to one, can be obtained as percentage values by averaging every row of the resulting matrix. The weights for the criteria computed in the best-material decision process are reported below:

Criteria:	Criteria Weights (%):
σ^y	0.3330
E	0.2038
ε_{rott}	0.1309
ρ	0.1729
T	0.0702
μ	0.0523
$Cost$	0.0369

Table 3.9: Criteria Weights

Furthermore, to perform the PWCM consistency check a Consistency Index (CI) is computed as in Equation 3.10:

$$CI = \frac{\lambda_{MAX} - n_{criteria}}{n_{criteria} - 1} \tag{3.10}$$

where:
λ_{MAX} is the maximum eigenvalue of the PWCM and $n_{criteria}$ is the total number of considered decision criteria.
Finally the consistency ratio (CR), which really gives us information about the matrix consistency, is computed as the fraction between CI and a Random Index. This latter index depends on $n_{criteria}$ and from the literature (see [32], [23]) such Random Index appears to be equal to 1,32 when using 7 different criteria as in this case. The Pairwise Matrix can be considered consistent and the obtained Criteria Weights are reliable if and only if: CR < 0.1.

Once valid Criteria Weights have been obtained, the so-called Criteria Matrix is simply compiled by listing all analyzed materials altogether with the nominal values of all the considered decision criteria, as shown in Table 3.10. Such matrix, generally rectangular, links every nominal value (aka. NV) to the corresponding material and decision criteria (with m = total number of considered materials and n = total number of criteria).

At this point a differentiation between beneficial and non-beneficial criteria must be made:

- **Beneficial Criteria:** criteria for which the decision maker would like to assess a maximum nominal value among the alternatives. In the specific case of optimal

	$Criteria_1$	$Criteria_2$	...	$Criteria_n$
$Material_1$	$NV_{1,1}$	$NV_{1,2}$	...	$NV_{1,n}$
$Material_2$	$NV_{2,1}$	$NV_{2,2}$	$\ddots$	$\vdots$
$\vdots$	$\vdots$	$\ddots$	$\ddots$	$NV_{m-1,n}$
$Material_m$	$NV_{m,1}$	...	$NV_{m,n-1}$	$NV_{m,n}$

Table 3.10: Criteria Matrix

material choice for the sabot, the beneficial criteria correspond to : [σ^y; E; ε_{rott}]

- **Not-Beneficial Criteria:** criteria for which the decision maker would like to assess a minimum nominal value among the alternatives. In the specific case of optimal material choice for the sabot, the non-beneficial criteria correspond to : [ρ; T; μ; Cost]

Therefore the decision-making process needs to take into account such difference, privileging those alternatives (or materials) presenting high beneficial criteria nominal values and low values for not-beneficial ones. In order to analytically perform such distinction and to apply the WSM, all elements of the Criteria Matrix $NV_{i,j}$ must be linearly normalized as follows:
If the NV corresponds to a beneficial criteria, its normalized value $NV_{normalized}$ is given by:

$$NV_{normalized} = \frac{NV_{i,j}}{NV_{max}} \tag{3.11}$$

While if the element $NV_{i,j}$ is associated with a non-beneficial criteria, then its NV can be computed as:

$$NV_{normalized} = 1 - \frac{NV_{i,j}}{NV_{max}} \tag{3.12}$$

Where NV_{max} stands for the maximum nominal value of the column to which element $NV_{i,j}$ belongs. Resulting from this normalization is a normalized Criteria Matrix (mxn), so finally the WSM can be applied and a performance score (PS) which allows us to perform a ranking of all alternatives can be calculated for each material:

$$PS = \sum_{1}^{m}{}_{i} CW_i \cdot NV_i \tag{3.13}$$

So by means of the Weighted Sum Model it's possible to group all computed PS in a Performance Score Vector [PSV], comprehensive all analyzed material's performance scores:

Alternatives:	**Performance Score Vector:**
$Material_1$	PS_1
$Material_2$	PS_2
$\vdots$	$\vdots$
$Material_m$	PS_m

Table 3.11: Performance Score Vector

The Best Performance Score Value (BPS) is the maximum element of such vector, it identifies the optimal material for the sabot accordingly to the MCDM methodology and it can be computed directly from Equation 3.9.
The illustrated procedure was then implemented in a Matlab® code, outlined as reported by algorithm 3.1. Such analysis showed that HIP was among the best materials.

Algorithm 3.1 AHP:

This code computes the criteria weights starting from a pairwise comparison matrix ($PWCM$) of dimension (m x m) previously compiled, according to the AHP process. Computing the Normalized PWCM as:
$sum_{column} = zeros(1, m)$;
for $j = 1 : m$ **do**
    $sum_{column}(1, j) = sum(PWCM(:, j))$;
end for
for $i = 1 : m$ **do**
    for $j = 1 : m$ **do**
        $PWCM_{norm}(i, j) = PWCM(i, j)/sum_{column}(1, j)$;
    end for
end for
Computing Criteria Weights (w) as:
for $i = 1 : m$ **do**
    $w(i, 1) = sum(PWCM_{norm}(i, :))/m$;
end for
Final instructions

3.3.4. Friction Reduction

The reduction of sliding friction between the sabot and the barrel's inner walls is another design principle which has been followed in order to maximize the projectile's muzzle velocity. Although such friction can never be completely eliminated, it is possible to reduce it adopting two different approaches:

1. Lubricate the sabot and cannon barrel
2. Employ materials with low friction coefficient

The first option requires inert industrial lubricant to be applied on all surfaces that come into contact. From the experimental point of view however, this results to be impractical: given the length of the gun is difficult to apply the lubricant, also this procedure should be repeated before each new shot. In addition to this, the exact amount of lubricant used may vary from shot to shot, affecting test's results and repeatability. Instead, if lubricant was applied exclusively on the sabot, it might not be sufficient to give appreciable improvements in terms of speed.

The second option seems to be the most promising one, as it guarantees good reliability and repeatability of the experimental tests. A material available on the market, characterized by one of the lowest coefficient of friction is Teflon, also known in the industry as Polytetrafluoroethylene (or PTFE). Polytetrafluoroethylene is an innovative polymer material used in many engineering applications [], both chemical and mechanical, for its resistance to aging, its high chemical inertia and its anti-adherent properties. Compared to the dynamic friction coefficient (μ_d) between HIPs and dry steel (which ranges between 0.35 and 0.4), PTFE exhibits a $\mu_d = 0.04$ on dry steel, about an order of magnitude lower. Other physical and mechanical properties for this material are reported in table 3.12.

σ^y [MPa]	10
E [MPa]	750
ε_{rott} [%]	380
ρ $[g/cm^3]$	2.2
$T_{melting}$ [°C]	327
μ_d	0.04

Table 3.12: PTFE Properties

From the above values it can be concluded that PTFE cannot be used for the manufacture of the sabot, as it has a density more than double that of HIPs, while its yield strength and elastic modulus are too low to withstand the loads generated during the shot. A good compromise between the good mechanical properties of HIPs and the low coefficient of

friction of PTFE is achieved by making a two-material sabot. That is, applying to the sabot two Teflon rings in correspondence of the contact surfaces with the inner cannon's barrel. These rings act as bearings and they are designed in line with the principle of mass reduction, therefore in the most weight-efficient way possible. It is also essential that these bearings do not exceed the nominal external diameter of the sabot, as to still have a clearance fit when loading the latter into the cannon. Considering these aspects it has been obtained sizing of the Teflon rings (reported in fig. 3.7), with the ring slightly wider at the base of the sabot, where the greater pressure acts and the contact surface is more extended.

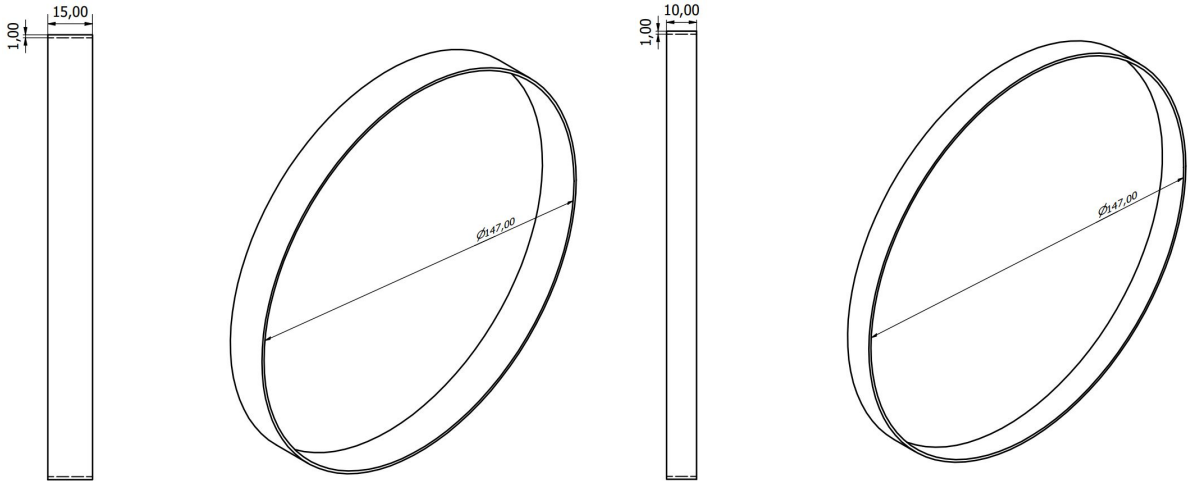

(a) Teflon Ring 1. (b) Teflon Ring 2.

Figure 3.7: Bearings' Sizing

The bearings have a maximum thickness of 1 *mm* to lower their mass and are wedged in the sabot at dedicated housings. Such housing slots (qualitatively depicted in figure 3.8) are designed in such a way as to facilitate the final assembly of the prototype and so that the acting pressure itself helps holding both rings in place.

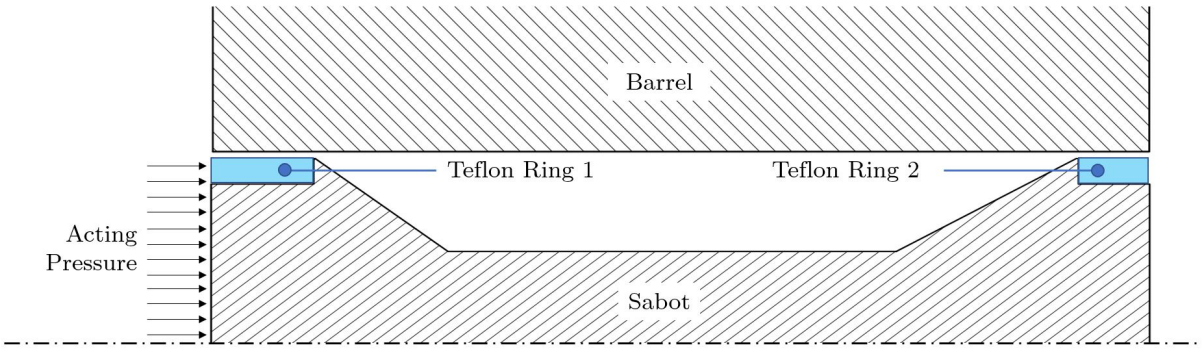

Figure 3.8: Bearings' Housing

To achieve a good joint to the sabot that doesn't solely depend on the pressing effect of pressure, a proper way to anchor the Teflon rings needs to be studied. On this front the main disadvantage in using Teflon emerges: its difficult machinability. In fact PTFE isn't suitable for welding techniques since when heated it releases toxic substances, neither to gluing techniques because of its high chemical inertia. This issue is addressed and discussed in chapter 4, section 4.2.4, where the sabot-Teflon bearings' assembly process is explained.

3.4. Preliminary Design

This section presents the new geometric shape adopted for the realization of the new Sabot. The use of different configurations and structural elements for its various parts is explained and motivated, accordingly to the design principles previously illustrated. All drawings for the new sabot were performed using the Autodesk Inventor® software, CAD models thus developed for each design will be the basis for the creation of their respective numerical models.

3.4.1. New Sabot Geometry

Referring to the old sabot labeled as S_{00}, the first preliminary design step was performed modifying such original geometry in order to make it more slender, accordingly to the mass reduction design principle. In fact, reducing sabot's body width as much as possible allows to lower its volume and weight. This must be done always considering the design's boundary conditions, in particular the minimum internal diameter needed to accommodate the surrogate bird, so the inner diameter is never taken less than $95 \pm 0.5\ mm$. Such leaner body must then be connected to the outer nominal diameter ($149 \pm 0.5\ mm$), so

that the sabot continues to have a proper fit inside the cannon's bore. It is preferable to have gradual junctions between different diameters instead of abrupt ones, as not to generate areas where stresses might concentrate and trigger failure mechanisms. Material is then removed from the original S_{00} design as in fig. 3.9a (subtracted areas are highlighted in red), leading to the resulting slender geometry of fig. 3.9b. Doing so gives a geometry traceable to a Saddle-Back-like configuration, previously illustrated in chapter 2, subsection 2.3.2. All wall thicknesses and final sizing are determined on the basis of the numerical simulations set out in the next chapter.

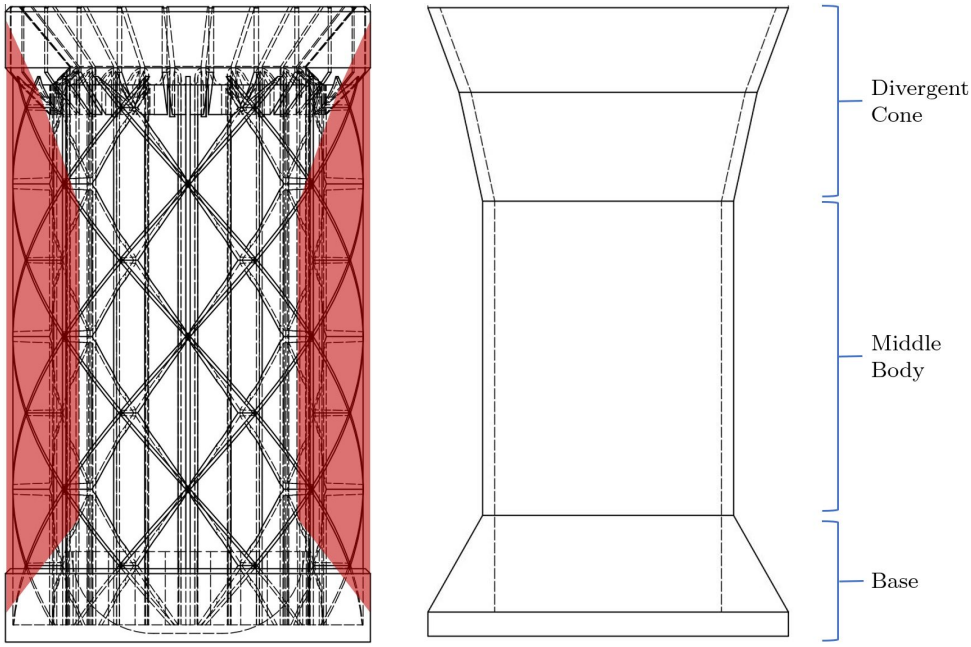

(a) S_{00} Material Removal (b) Slender Geometry

Figure 3.9: Sabot's New Geometric Shape

Referring again to fig. 3.9b, three different elements of the sabot's structure are identified: the base, the central (or middle) body and the terminal (or divergent) cone. For each of these, different structural geometries have been investigated in order to find the most efficient configuration in terms of stress resistance and lightness.

3.4.2. Sabot Base

The base of the sabot is an important structural element, as it must fulfill the task of bearing the pressure wave acting on its bottom surface when the launching system is triggered. Therefore it is one of the most stressed parts of the sabot and so, having to be extremely stiff in order to withstand such high impact loads, it's not by chance also

the heaviest (its mass ranges from 36% to 40% of the total mass of the sabot). Two different geometric shapes have been considered for the realization of the base during the preliminary design phase:

- Flat Plate Base
- Spherical Cap Base

The Flat Plate Base:
Taking the base as a flat circular plate has been the most adopted solution in the past for the realization of the sabot. Assuming a uniform pressure distribution on the back face of the flat plate, this will be aligned along the longitudinal axis of the cannon and the sabot, so the resulting force accelerating the sabot-projectile package will also be acting along such axle and will be equal to:

$$F_x = P \cdot A = P \cdot \pi \cdot r^2 \tag{3.14}$$

Where: P = Acting Pressure, A = Circular Face Area and r = Circular Face Radius. However, such flat plate base presents two main disadvantages. The first is of a structural nature, it can be better visualized by separating the base from the rest of the sabot (as in the free body diagram of fig. 3.10) and looking at the forces acting on it.

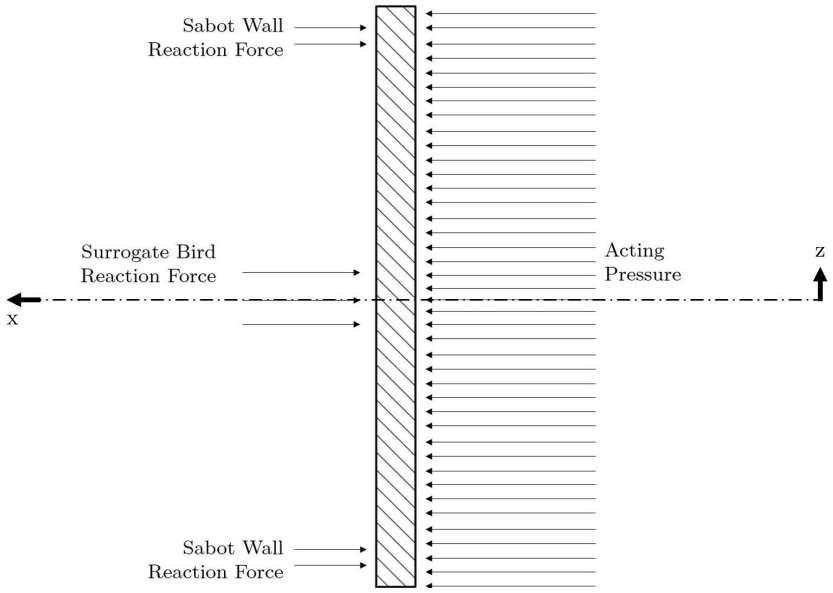

Figure 3.10: Flat Base Free Diagram

The working pressure is evenly distributed on the lower surface of the base, but during the acceleration phase inertia forces are also generated. The inertia force of the surrogate

bird (which has a mass of $1Kg$) and the inertia force due to the remaining parts of the sabot (middle body and terminal cone) both act in opposite direction with respect to the applied pressure, opposing the system's motion. Considering that the inertia forces of the remaining sabot's elements are far inferior in magnitude to that of the $1Kg$ dummy bird, the base is expected to undergo high bending stress.

The second disadvantage of a simply flat base concerns the prototype production. During construction stage, as best explained in section 4.2 of chapter 4, the flat base of the sabot adheres excessively to the plane of the 3D printer. Because of this, when removing the finished piece, the sabot's prototype may suffer irreversible damage, as already happened in the past.

The Spherical Cap Base:

A spherical cap base presents a different geometric configuration, in which the back face of the base has an assigned curvature and therefore its surface area is larger. Because of the base curvature, the applied pressure will always act along the normal direction to the surface of the spherical cap base, assuming the distribution depicted in fig. 3.11:

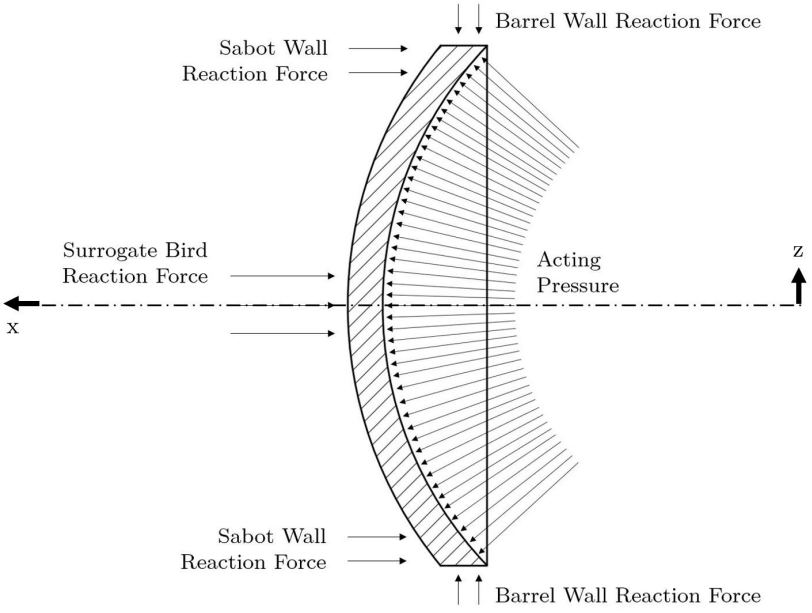

Figure 3.11: Cap Base Diagram

This means that pressure distribution, while remaining uniform, is no longer entirely aligned with the direction of the longitudinal axis of the gun and sabot. Nevertheless using this type of base does not involve any loss in terms of resulting pressure force acting along the axle and accelerating the sabot-bird package.Assuming the pressure forces to be

evenly distributed on the spherical surface, they will be radial and perpendicular to the infinitesimal surface element dS. The area of such element dS, in spherical coordinates, is given by:

$$dS = r \cdot d\phi \cdot R \cdot d\theta = R^2 \cdot \sin\theta \cdot d\theta d\phi \tag{3.15}$$

Therefore the infinitesimal pressure force acting upon the infinitesimal surface can be written as:

$$dF = P \cdot dS = P \cdot R^2 \cdot \sin\theta \cdot d\theta d\phi \tag{3.16}$$

Breaking down dF into its components along the reference system's axes:

$$\begin{cases} dF_x = dF \cdot \cos\theta, & \text{(3.17a)} \\ dF_y = dF \cdot \sin\theta \cdot \cos\phi, & \text{(3.17b)} \\ dF_z = dF \cdot \sin\theta \cdot \sin\phi, & \text{(3.17c)} \end{cases}$$

The transversal components dF_y and dF_z involve a pressing action of the base against the inner surface of the cannon and are balanced by its reaction forces. While this tends to increase friction, it also helps reducing the air leakage between cannon and sabot. The longitudinal component dF_x instead will decrease in magnitude moving towards the outer edge of the base, providing less flexural stress. For ϕ going from 0 to 2π and θ ranging from 0 to $\overline{\theta}$, the resultant longitudinal force acting on the spherical cap base will be:

$$F_x = P \cdot R^2 \cdot \int_0^{\overline{\theta}} \sin\theta \cdot \cos\theta d\theta \int_0^{2\pi} d\phi = P \cdot R^2 \cdot 2\pi \cdot \int_0^{\overline{\theta}} \sin\theta \cdot \cos\theta d\theta \tag{3.18}$$

$$F_x = P \cdot R^2 \cdot 2\pi \cdot \frac{\sin\overline{\theta}^2}{2} = P \cdot \pi \cdot r^2 \tag{3.19}$$

The spherical cap base is therefore able to provide the same acceleration force while generating less bending stress with respect to the flat plate base. So, by adopting this base, it should be possible to employ higher launch pressures. On the other hand, as the curvature of the spherical cap increases, the mass of the base increases while dF_x decreases at the outer edges. A good trade-off has been found sizing the spherical cap surface as shown below:
The frontal part of the base is taken flat in order to allow the projectile's inertia forces to act on a region with a diameter equal to the surrogate bird's one. To reduce mass,

the base has been engraved and ribs have been made with a 45^{o} angle with respect to the axle, connecting the base's rear part with its frontal flat surface, thus arriving at the final configuration for the spherical cap base used in many preliminary designs. A great advantage of this geometry is that it eliminates previous problems related to the production of the sabot, since the base no longer adheres to the printing surface, but leans on removable supports. This way the finished sabot can be detached very easily and without any danger of breaking it.

3.4.3. Middle Body

The central part of the sabot is the largest, in terms of size. It must be wide and long enough to accommodate the surrogate bird while remaining rigid enough to withstand the compressive loads it undergoes during acceleration. For this reason, when designing this part of the sabot it emerged the need to use a structure that was efficient both in terms of weight and strength. Polymeric honeycomb structures [39] are characterized by a high stiffness-to-weight ratio, they are widely known and used in many engineering applications for their great energy absorbing abilities. During the development of the sabot's middle body, two different configurations for an honeycomb structure were considered:

- Perforated Configuration
- Sandwich Configuration

The perforated configuration (fig. 3.12) consists in giving to the central body of the sabot a mesh shape, which completely wraps the surrogate bird. The geometry exhibits the typical element of a cross-section honeycomb structure (the hexagonal cell) embossed on the lateral surface and repeated in a pattern. This configuration allows to considerably reduce the mass, leading to the development of preliminary projects characterized by minimum amount of material and weight. Considering the limitations due to the 3D printing process (explained in detail in the next chapter), the hexagonal elements are not regular hexagons. They have been oriented and modified in such a way as to never present an angle with respect to the vertical direction greater than 40°. Several variants of this configuration have been investigated, varying the size and density of the hexagonal mesh, in order to analyze how the stiffness and strength properties of the resulting sabot would change.

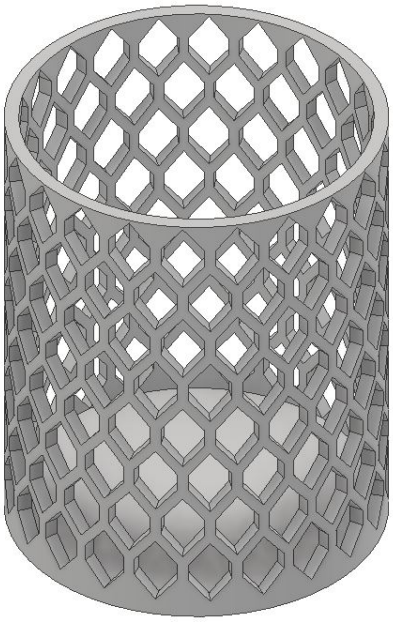

Figure 3.12: Perforated Configuration

The sandwich configuration instead consists in creating a honeycomb structure within the thickness of the middle body's cylindrical wall, enclosing it between two solid walls, as illustrated in fig. 3.13. This second solution is less weight-efficient but more performing as it is able to exploit the most the honeycomb structure's high compressive strength. In this configuration, in fact, when compressive forces are exerted on the central body the walls of adjacent honeycomb channels act to keep each honeycomb tube rigid, thus avoiding strong deformations. This structure also does not suffer from the limitations of 3D printing, as the tubes are oriented as the printing direction along the vertical, so regular hexagon-shaped channels can be used. Also for this configuration some different variants have been studied: interspersing honeycomb channels with one or more solid rings (thus shortening the tube's length) allows to increase the structural stiffness.

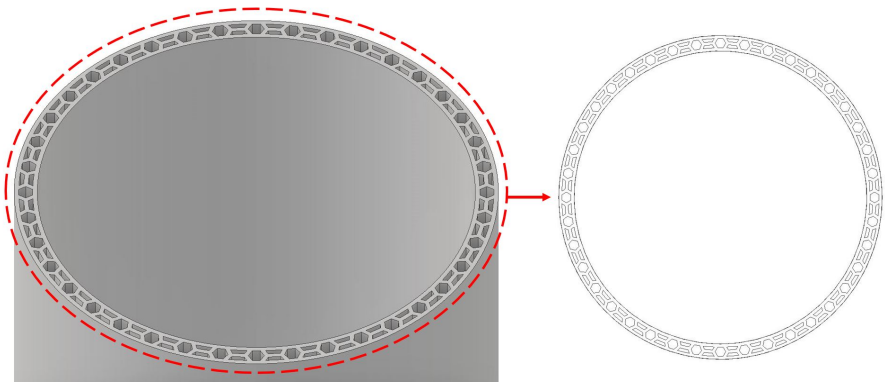

Figure 3.13: Sandwich Configuration

3.4.4. Divergent Cone

The terminal part of the sabot, consisting of the divergent cone, is the first that comes into contact with the stopper. The stopper has a lateral surface inclined by 45° with respect to the axle and an internal hole larger than that of the sabot, where the dummy bird resides. This ensures that the surrogate bird doesn't impact against the stopper, but also implies that some of the sabot's debris passes through the stopper along with the projectile. Since this is an undesirable condition, the sabot's cone design tries to mitigate it and is aimed to make the sabot gradually open upon its impact with the stopper, so that as many debris as possible can be radially deflected. For this purpose the sabot's divergent cone is designed with a taper angle smaller than the one of the stopper's lateral surface, in order to break radially and to guide the opening of the rest of the sabot in the same direction. Once again machinability has been taken into account, so the cone's taper angle was set to be always inferior to 40° with respect to the sabot's longitudinal axis. Clearly it has been tried to minimize also the mass of this terminal part of the sabot, at times thinning the walls Although, since this part of the sabot is a point of contact with the walls of the cannon where the weight of the sabot-bird package is discharged, the thinning was accompanied by the construction of thicker ribs to strengthen its structure. Another solution that has been used to subtract material is the creation of grooves that have the dual purpose of lightening and weakening the cone facilitating its radial opening.

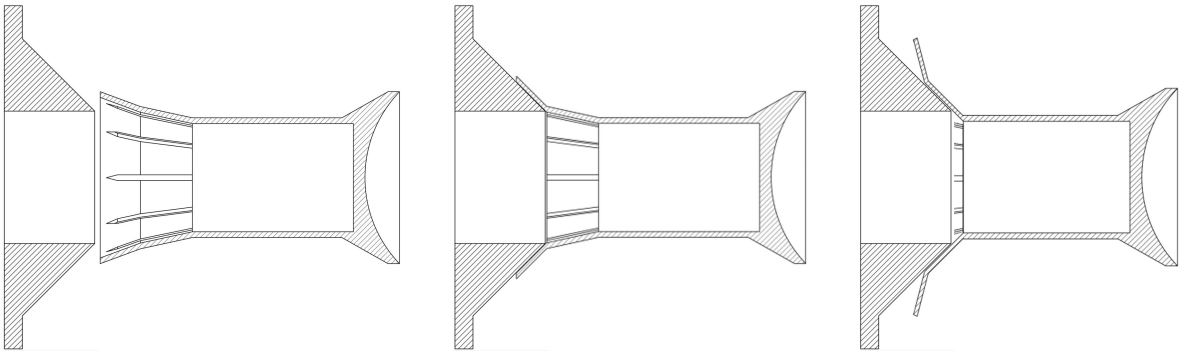

(a) (b) (c)

Figure 3.14: Desired Divergent Cone Opening

3.4.5. CAD Models

The various structural elements described above were used for the realization of the sabot's preliminary designs, which were developed as CAD models using Autodesk Inventor® software. In this working environment it was possible to monitor the estimated volume

of each geometry, in order to keep the design process in line with the mass reduction principle. These estimates were provided directly by the software. Below is reported a preview of the models along with their respective volume values, each design will be further discussed in relation to its numerical simulation results.

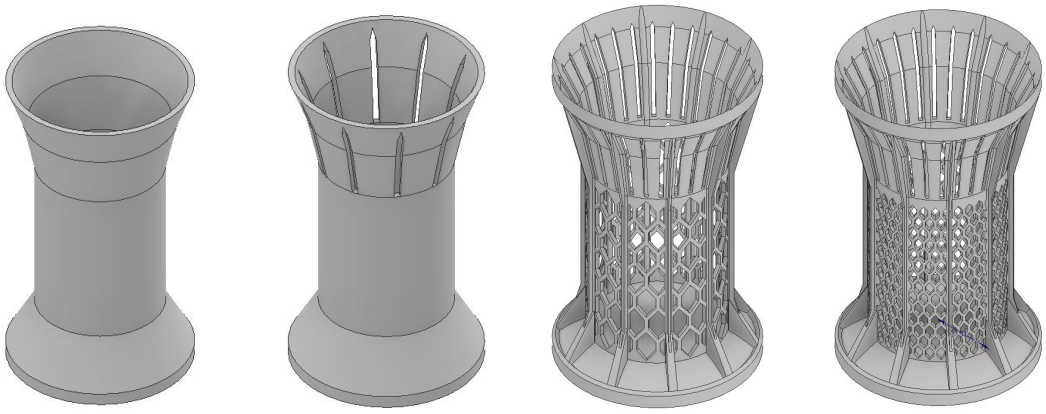

(a) S_{01} (b) S_{02} (c) S_{03} (d) S_{04}

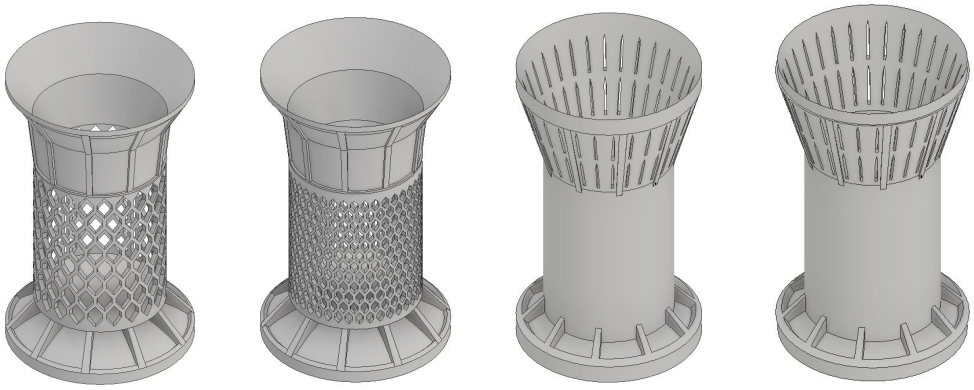

(e) S_{05} (f) S_{06} (g) S_{07} (h) S_{08}

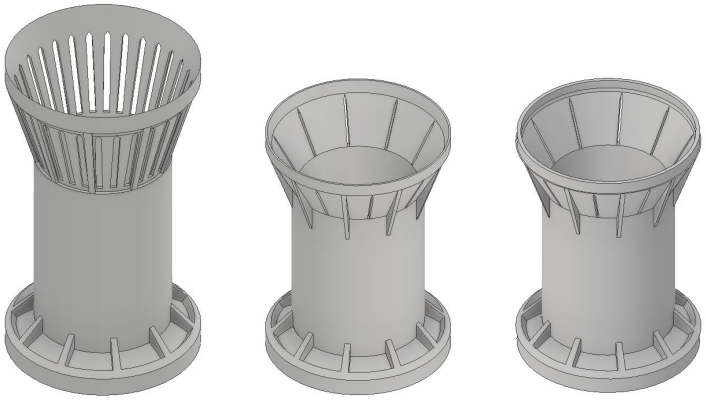

(i) S_{09} (j) S_{10} (k) S_{11}

Figure 3.15: Sabot 3D Models

Design Label	Volume $[cm^3]$
S_{01}	758.8
S_{02}	705.1
S_{03}	258.7
S_{04}	268.4
S_{05}	284.1
S_{06}	301.1
S_{07}	489.8
S_{08}	471.1
S_{09}	422.4
S_{10}	416.2
S_{11}	409.7

Table 3.13: Estimated Volumes

4 | Sabot Optimization

This chapter describes the optimization procedure for all preliminary designs, which exploits both numerical simulations and experimental tests.

The development of numerical models is discussed in the first section, where all numerical results are also presented and will be further discussed in relation to the outcomes of the corresponding experimental tests. Finite-element (F.E.) numerical simulations represent a fundamental tool for the improvement of the original design, guiding it towards the optimal one. Numerical models and simulations were both realized in LS-DYNA®, a specific finite-element software for high impact phenomena which uses explicit time integration to perform nonlinear dynamic analysis.

Section 4.2 deals with the production techniques and methodologies employed in the manufacturing of sabots' prototypes as well as in the assembly of the final projectile to be fired. Critical issues related to such process are addressed, altogether with the adopted solutions in order to overcome them.

The third and final section of the chapter on experimental tests illustrates all instrumentation and procedures used, providing a detail description of all performed tests. The experimental tests allow to validate the numerical models previously developed and are also an integral part of the optimization process for preliminary designs, as they provide an effective feedback on the basis of which it's possible to perform targeted design changes.

4.1. Finite Elements Models (FEM)

Two F.E. numerical models have been developed: the first to simulate the firing of the sabot-projectile package inside the cannon in order to investigate its motion and the ability of the sabot to withstand the loads applied, aimed at assessing its structural integrity. The second numerical model simulates the impact between the sabot and the stopper, it's main objective is to study the sabot's failure mode as well as the quality of the separation between sabot and dummy bird.

In both numerical models the main focus is on the sabot, since the dummy-bird must not break neither during the acceleration phase inside the barrel nor during its separation from the sabot. For this reason it was chosen to model the surrogate bird in the simplest way possible.

Before performing numerical simulations in LS-DYNA®, every sabot's CAD model was first imported into Hypermesh® in order to build its corresponding mesh (fig. 4.1a). Given the complexity of the geometric shapes, which feature several curved surfaces and facets, all sabots' meshes were realized using solid tetrahedral elements (fig.4.1b) with a characteristic size per side ranging from 2 $[mm]$ to 7 $[mm]$, exception made for design S_{01} which was possible to mesh with quadrilateral (hexahedral) elements. Since the mesh has great influence on the outcome of numerical simulations, mesh quality has always been evaluated before importing it into LS-DYNA® by checking element's aspect ratio, smoothness, orthogonality and other quality metrics [24] as well as the presence of duplicate nodes.

(a) S_{08} Mesh (b) Tetrahedron

Figure 4.1: Meshing example and element

4.1.1. Numerical Formulations

Real bodies can be modeled in numerical environment accordingly to finite element method [18] using different formulations, such as:

- Lagrangian
- Arbitrary Lagrangian Eulerian (or ALE)
- Smoothed Particle Hydrodynamics (or SPH)

Lagrangian formulation is used to asses the static, quasi-static and dynamic response to loads which induce deformations. In this approach every node of the model's mesh is attached to the material particle, so that the mesh moves with the physical material as it deforms. This allows an accurate and efficient tracking of material interfaces, as well as the incorporation of complex material models [18]. Lagrangian method has the advantage of being rather simple to implement in a finite element code, while its main disadvantage consists in providing unreliable results for large deformation problems, since in these cases mass losses often occur [30].

ALE formulation, unlike the Lagrangian one, allows to analyze phenomena with large deformations. The methodology consists of a combination of Lagrangian and Eulerian approach, as the physical material moves inside a fixed mesh. Since the bird behaves like a fluid at impact, ALE description is better suited and often used for bird-strikes and airframe impact applications [33].

SPH formulation doesn't require any mesh, the model consists of multiple particles bound together accordingly to an equation of state (EOS). This approach is particularly suitable for phenomena with extremely high deformations and material breakage, which is why it has been used at the La.S.T. laboratory for developing accurate surrogate bird's models.

Considering the main application for the numerical models to be developed (namely the projectile launch), large deformations of the sabot's model are nor desired and neither expected. Therefore a Lagrangian type formulation was adopted.

4.1.2. In-Bore Numerical Model

The first numerical model, developed to analyze the in-bore behavior of the sabot, consists of 4 distinct parts:

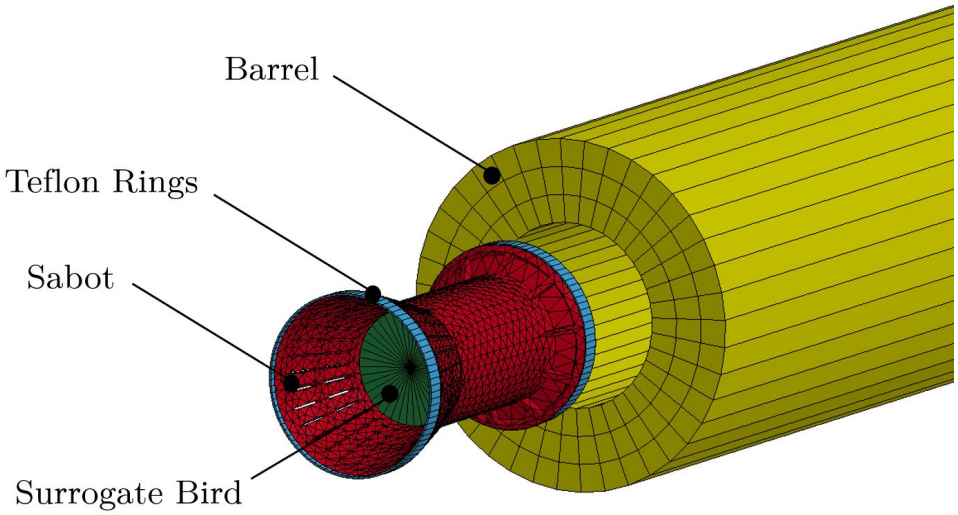

Figure 4.2: In-Bore Numerical Model

- **Sabot:**

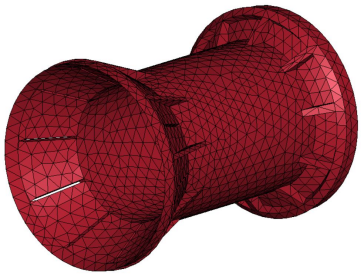

Figure 4.3: Sabot Model

Once imported the sabot's mesh to LS-DYNA®, the material was assigned to the part via the *`MAT_PIECEWISE_LINEAR_PLASTICITY` card, compiled with all HIPS data. Material type 024 [25] is a well known material model for polymers and isotropic elasto-plastic materials, originally developed for metals. To date it represents the most basic and widespread LS-DYNA® material for modelling high rate-dependent phenomena such as drop and crash tests, whose accuracy also depends on the linearity of the stress-strain curve up to the yield point: a condition verified for HIPS (as shown in fig.4.4).

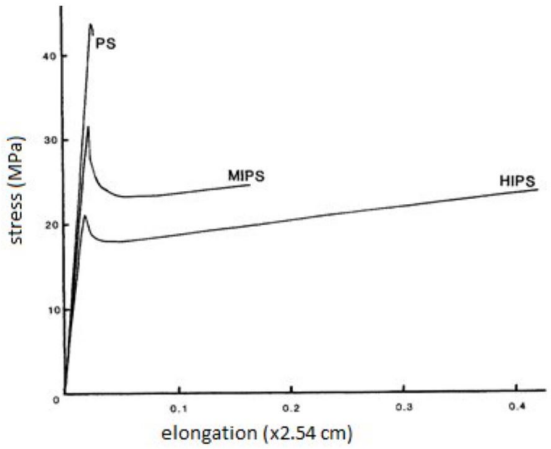

Figure 4.4: HIPS Stress - Strain Curve [16]

A discrepancy between the real sabot and its model consists in the fact that assigning the material, LS-DYNA® generates a part with 100% material infill, while the real piece is produced with a lower infill percentage (as will be explained in section 4.2). However such difference is acceptable, since if a simulation for a fully filled sabot (and therefore tendentially stiffer) isn't satisfactory, then it's plausible to assume that also the experimental test for the respective real sabot (with a lower filling and therefore less stiff) will not succeed. Vice-versa if a numerical simulation has satisfactory outcome, also its experimental test can be expected to succeed. Apparently, a possible solution would be to appropriately change the density of the material type 024, but doing so would alter the properties and the stress response of the material itself. In addition, since many preliminary designs feature a middle body and walls with 100% infill, such operation wouldn't lead to much more accurate solutions. As for the formulation of sabot's elements instead, it was chosen by setting the parameter `ELFORM`=10 of the *`SECTION_SOLID` card. Doing so allows to use a single integration point for every tetrahedral element when performing the explicit integration, thus saving on computational costs.

- **Barrel**:

Considering the gun bore as a non-deformable component, its model (fig. 4.5) consists of 720 solid and rigid elements, with material properties of steel. The barrel was shaped and meshed in LS-DYNA® respecting its real dimensions (inner diameter of 150 $[mm]$ and 7.5 $[m]$ length).

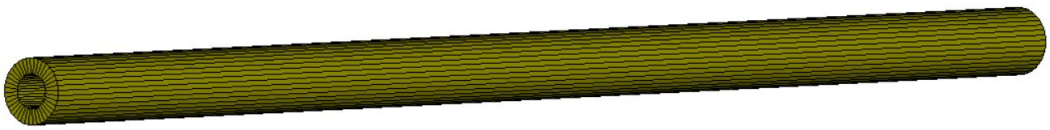

Figure 4.5: Barrel Model

All possible displacements and rotations were constrained by setting `CON1`=7 and `CON2`=7 inside the *`MAT_RIGID` card.

- **Surrogate Bird:**

In many studies previously conducted at La.S.T., very accurate bird models were developed involving SPH formulation, an ellipsoidal shape and the use of material types: *`MAT_ELASTIC_PLASTIC_HYDRO` or *`MAT_NULL`. However, since the surrogate bird's behaviour is not of great interest in this work, it was simply modelled with a Lagrangian formulation (`ELFORM`=1) using rigid solid elements and a cylindrical shape (fig. 4.6), as suggested by Bowman and Frank [6].

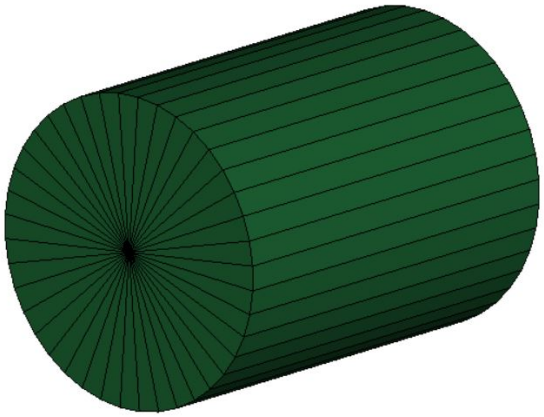

Figure 4.6: Surrogate Bird Model

The model used consists of 40 elements, its characteristic dimensions (95 $[mm]$ in diameter and 160 $[mm]$ in length) comply with the real bird ones. Due to the simplicity of its geometry, the mesh was made directly via LS-DYNA®, while the 1 $[Kg]$ mass was obtained by appropriately assigning the density in the material card *`MAT_RIGID`. It should be noted that the dummy bird's mass plays a fundamental role in numerical simulation because the pressure distribution, and therefore the stresses generated inside the sabot, greatly depend on the density of the body it carries.

- **Teflon Rings**:

The teflon rings were also modeled using material type 024, inserting the Teflon parameters for the material actually used in the experimental tests. The model used consists of 88 solid elements per ring, no link or tie between the rings and the sabot has been defined, only the contacts between the two parts.

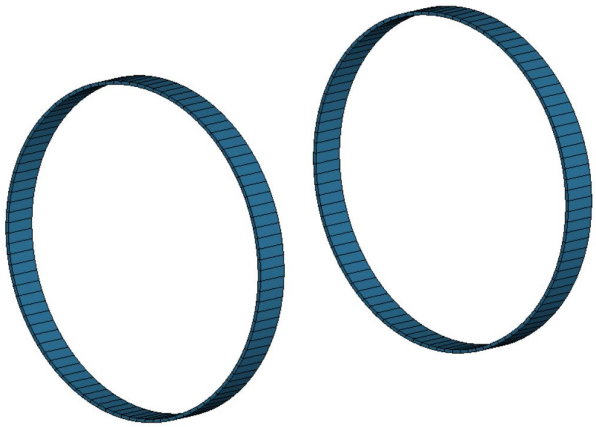

Figure 4.7: Teflon Rings Model

It should be noted that teflon bearings have not been used in all numerical simulations but only for those relative to preliminary designs S_{08} and S_{11}, specifically designed to accommodate them.

Contacts:

The definition of the contacts between the different parts of the numerical model highly affects results accuracy and computational costs. It is also essential to correctly define all contacts in order to avoid any con-penetrations or errors during the simulation. Given the long duration of the launch phenomenon, since the sabot-bird package has to travel the entire length of the barrel, it was opted for a contact which doesn't excessively affect CPU time. Therefore `*CONTACT_AUTOMATIC_SINGLE_SURFACE` contact type has been employed between all parts; namely (depending on the case) at the sabot-bird, sabot-teflon rings and sabot-barrel/teflon rings-barrel interfaces. Furthermore, such contact type employs contact search algorithms which make it suited to handle disjoint meshes [17]. Friction coefficients of 0.4 and 0.04 were set within the sabot-barrel and teflon rings-barrel contact cards respectively.

Loads:

The main load, due to driving pressure accelerating both sabot and projectile, was modeled by defining a constant pressure curve for the whole duration of the launch. This pressure was then applied impulsively to the base of the sabot via the *LOAD_SEGMENT_SET card. In the case of sabot with teflon bearings, the segment set upon which pressure acts consists of both sabot's and first ring's bases. The effect of gravity was also accounted for by assigning an acceleration of -9806 $[mm/s^2]$ along the z-axis, through the *LOAD_GRAVITY_PART card, for every part inside the barrel.

4.1.3. In-Bore Simulations' Results

A total of 11 F.E. analyses were performed, one for each preliminary sabot design. The following are the results of all numerical simulations, on the basis of which all changes made to every design are motivated. Technical drawings for each sabot are also displayed to better highlight main differences between various designs. The criteria chosen to determine whether a numerical simulation can be considered satisfactory are:

1. Absence of failed elements
2. Maximum Von-Mises stress (σ_{max}) lower than HIPS' tensile strength (21 $[MPa]$)
3. Maximum plastic deformation (ϵ_{max}) lower than HIPS' elongation at break (42 %)

Sabot design labeled as S_{01} was obtained by applying the saddle-back configuration to the original sabot, it has solid and thick walls which allow to easily sustain all loads during launch without any significant deformation. In design S_{02} the spherical cap base is introduced while mass reduction is achieved using slightly thinner walls and by adding 10 grooves on the divergent cone. Subsequent versions of the sabot (S_{03}; S_{04}; S_{05}; S_{06}) realize a great mass reduction through the honey-comb perforated configuration for the middle body. However, even using 10 ribs along the body's length or employing increasingly finer hexagonal meshes to locally increase stiffness, numerical outputs show excessively high stresses being generated, sometimes causing structural bulking at the central body [37]. With the S_{07} design instead satisfactory results were obtained, both in terms of weight-efficiency and compressive strength, thanks to the adoption of the sandwich configuration for the middle body. Sabot S_{08} was obtained adapting the S_{07} design in order to employ teflon rings. Numerical results of its simulation show that structural integrity is also guaranteed in this case, with teflon rings (which have higher mechanical properties than HIPS) remaining undeformed during launch. Such result gave the green light for the production and experimental testing of teflon bearings. A further attempt to reduce sabot's mass was performed with design S_{09} by increasing grooves' size in the divergent cone. Although such solution increased stresses in the surrounding area leading to un-

satisfactory numerical results. Another way was then followed: reducing sabot's length a lighter piece tailored around the dummy bird was developed. Resulting designs S_{10} and S_{11} (respectively with and without teflon rings) both exhibited good behaviours during the launch simulation. For these final versions, in the light of experimental test's results (see chapter 5), the middle body's inner diameter was increased from 95 $[mm]$ to 97 $[mm]$ in order to improve sabot separation's quality. Furthermore a shorter cone was designed slightly increasing its taper angle, with the addition of thin grooves and ribs on its side walls to control and direct the radial opening.

Numerical Simulation N°1:

Simulation results satisfactory.

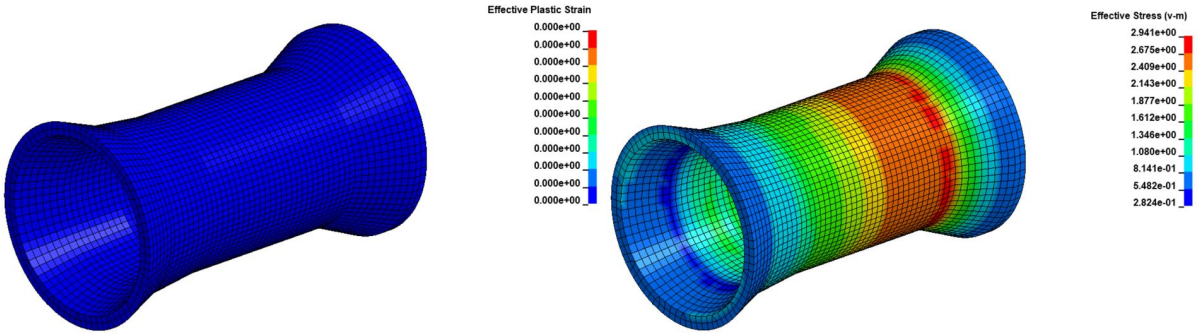

Figure 4.8: S_{01} Numerical Results

Design Label	Launch pressure	Estimated Mass [g]	ϵ_{max} [%]	σ_{max} [MPa]
S_{01}	7	453	0	2.9

Table 4.1: S_{01} Simulation Data

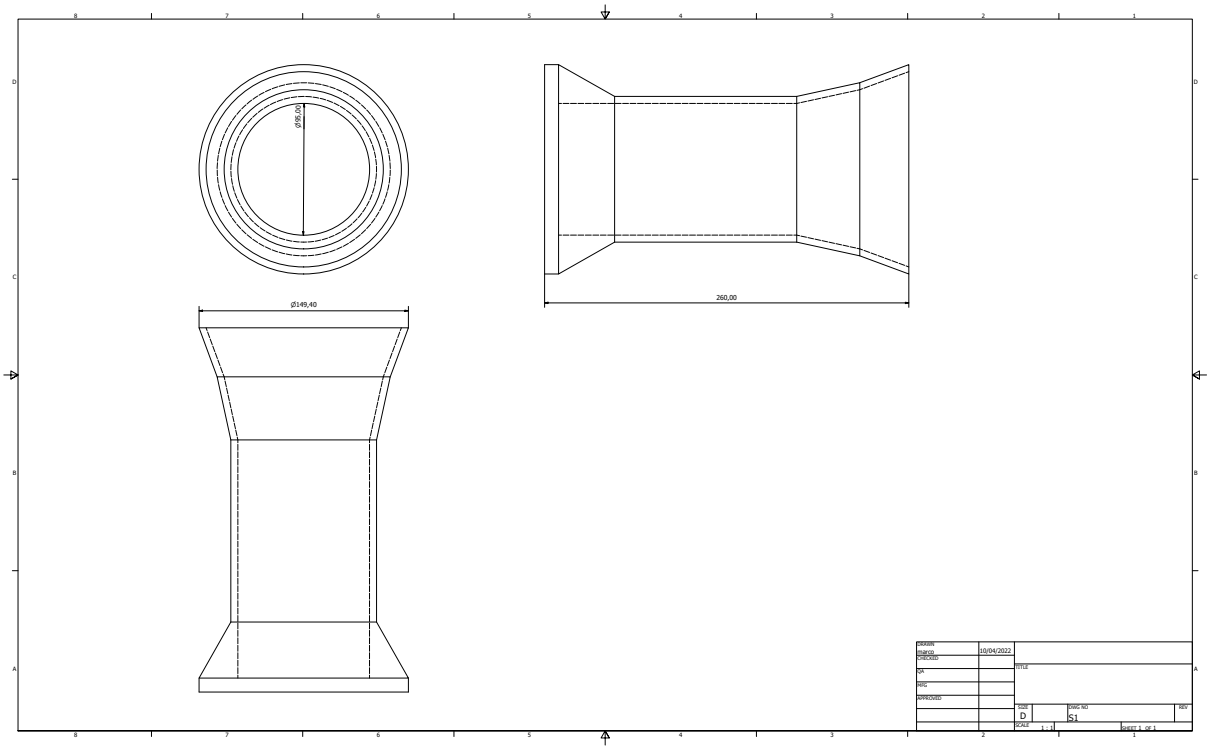

Figure 4.9: S_{01} Technical Drawing

Numerical Simulation N°2:

Simulation results satisfactory.

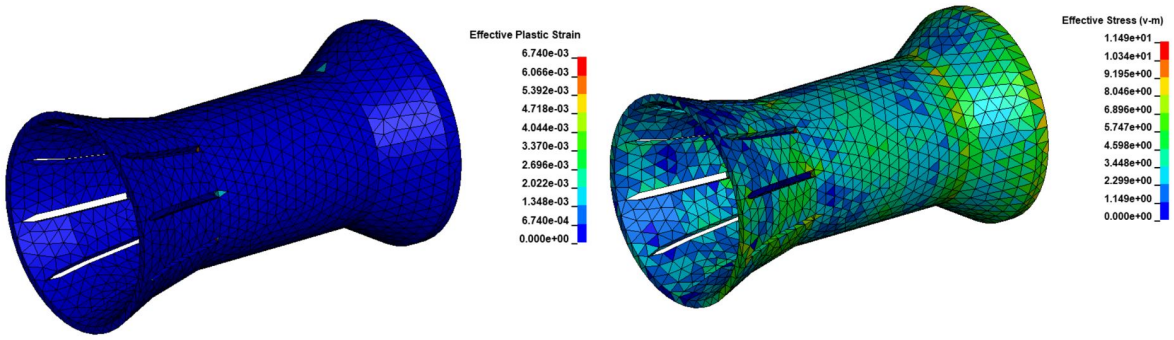

Figure 4.10: S_{02} Numerical Results

Design Label	Launch Pressure [bar]	Estimated Mass [g]	ϵ_{max} [%]	σ_{max} [MPa]
S_{02}	7	440	0.0067	11.49

Table 4.2: S_{01} Simulation Data

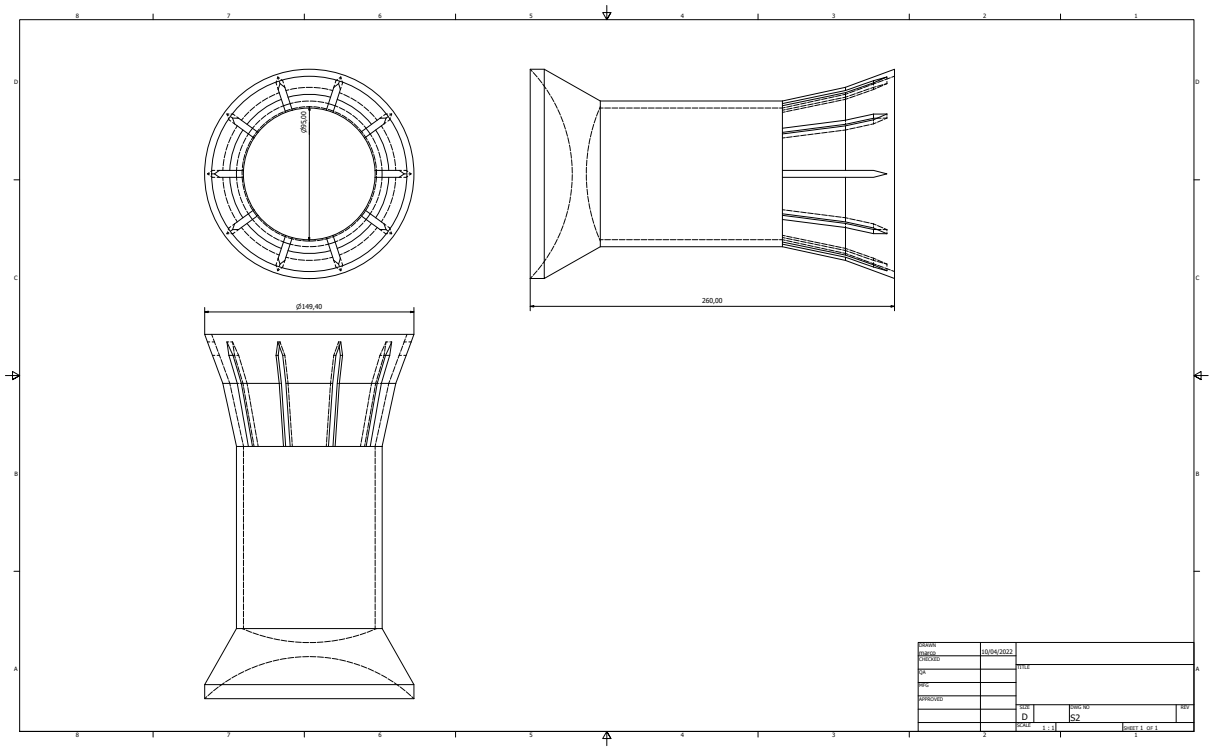

Figure 4.11: S_{02} Technical Drawing

Numerical Simulation N°3:

Simulation results unsatisfactory.

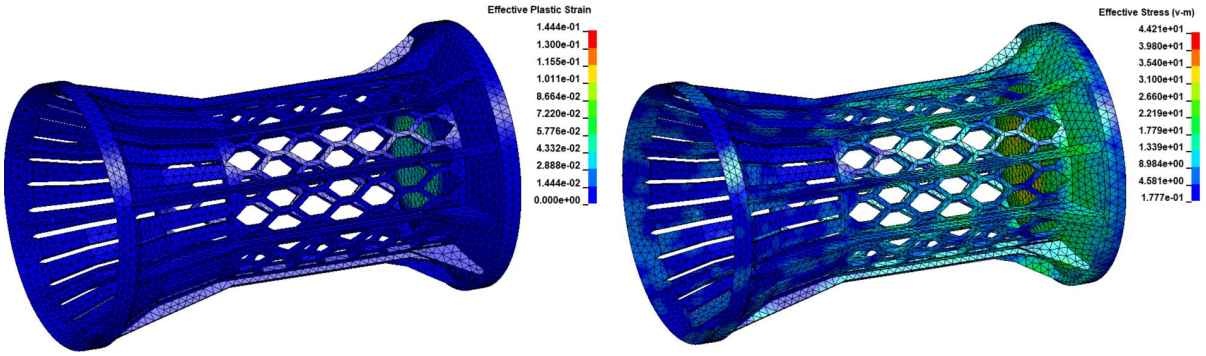

Figure 4.12: S_{03} Numerical Results

Design Label	Launch Pressure [bar]	Estimated Mass [g]	ϵ_{max} [%]	σ_{max} [MPa]
S_{03}	7	212	0.144	44.21

Table 4.3: S_{03} Simulation Data

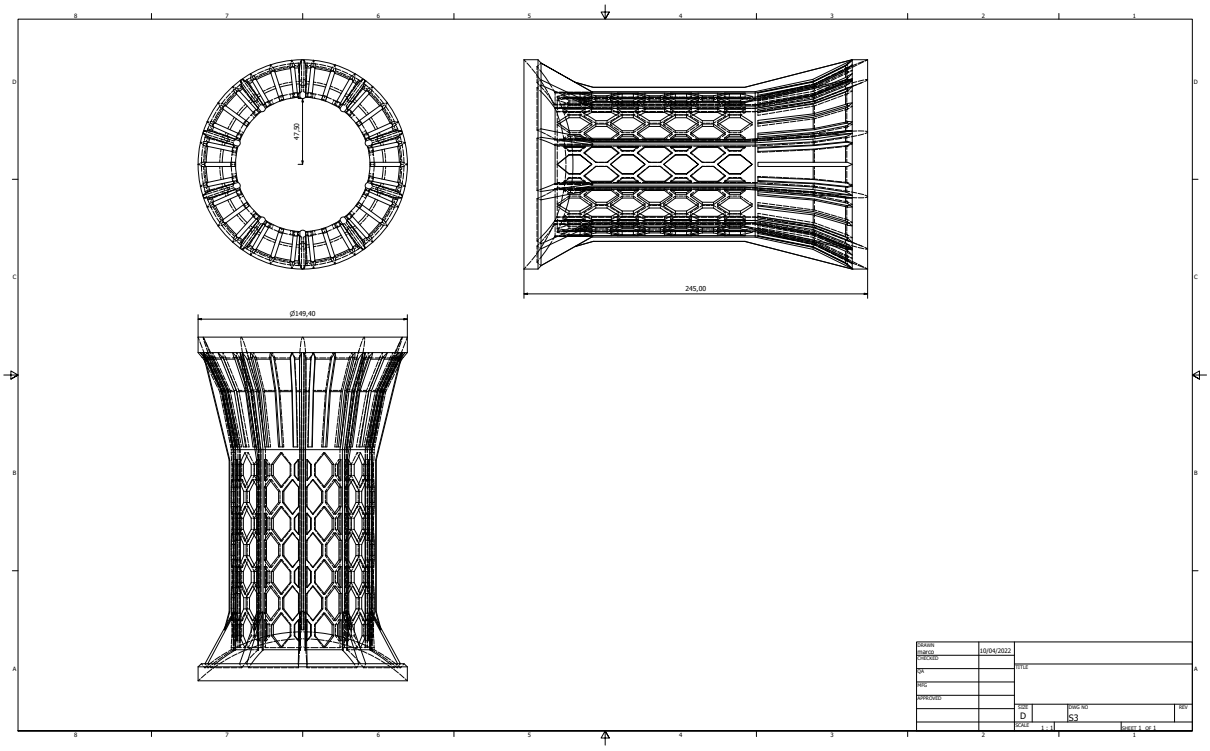

Figure 4.13: S_{03} Technical Drawing

Numerical Simulation N°4:

Simulation results unsatisfactory.

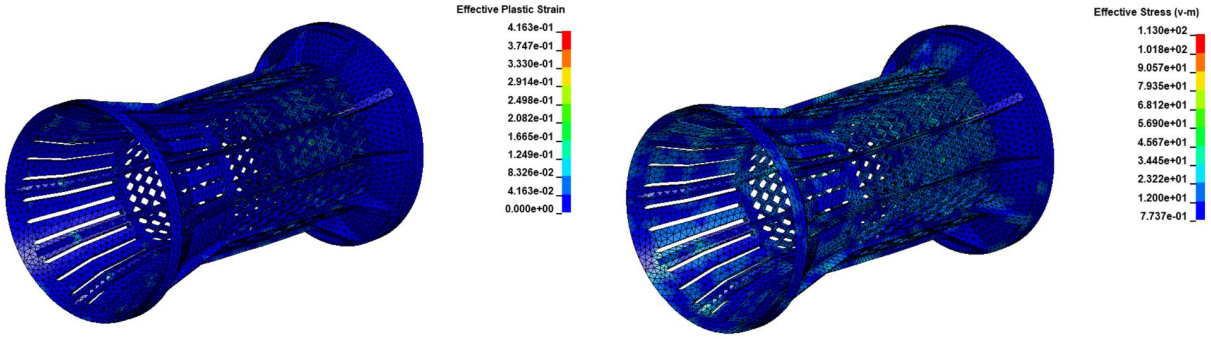

Figure 4.14: S_{04} Numerical Results

Design Label	Launch Pressure [bar]	Estimated Mass [g]	ϵ_{max} [%]	σ_{max} [MPa]
S_{04}	7	223	0.416	113

Table 4.4: S_{04} Simulation Data

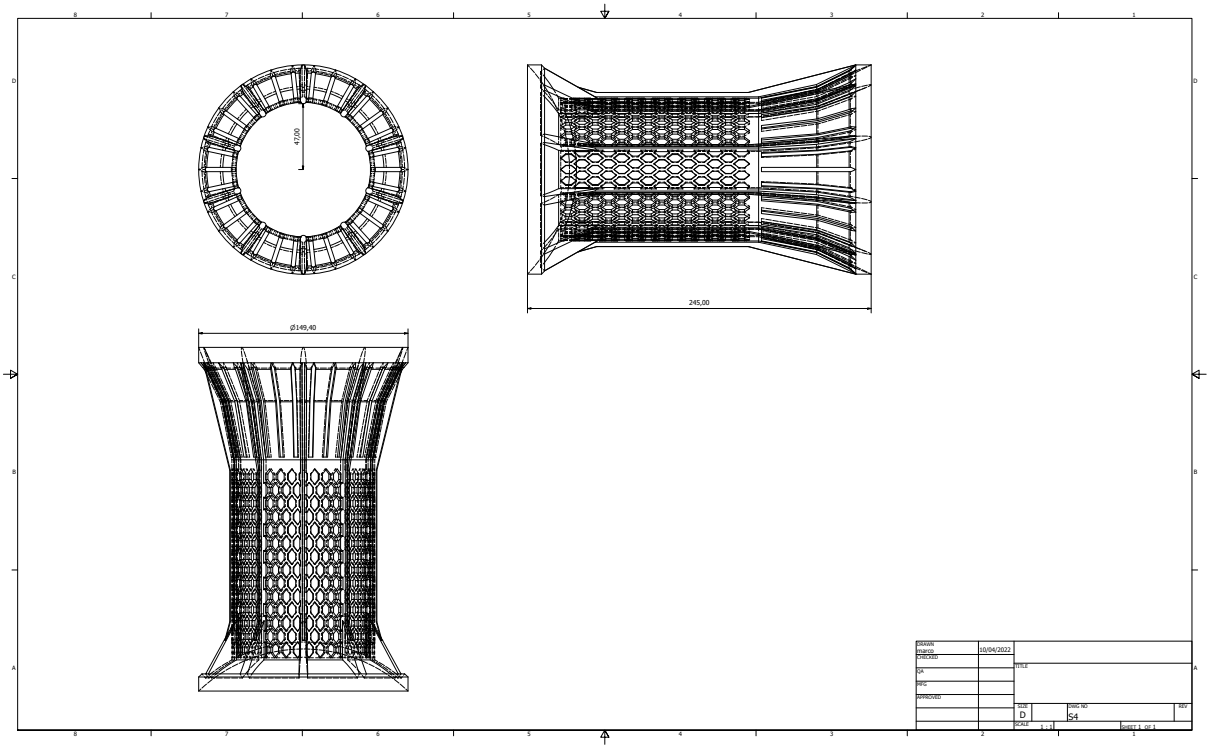

Figure 4.15: S_{04} Technical Drawing

Numerical Simulation N°5:

Simulation results unsatisfactory.

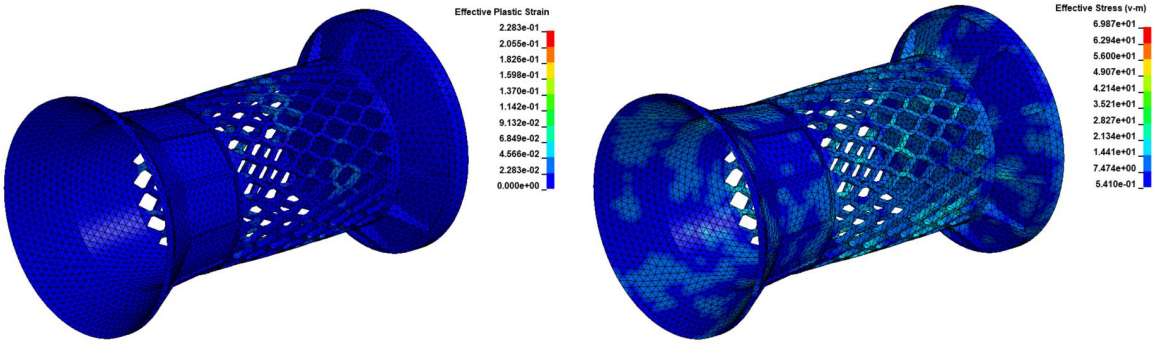

Figure 4.16: S_{05} Numerical Results

Design Label	Launch Pressure [bar]	Estimated Mass [g]	ϵ_{max} [%]	σ_{max} [MPa]
S_{05}	7	240	0.228	69.87

Table 4.5: S_{05} Simulation Data

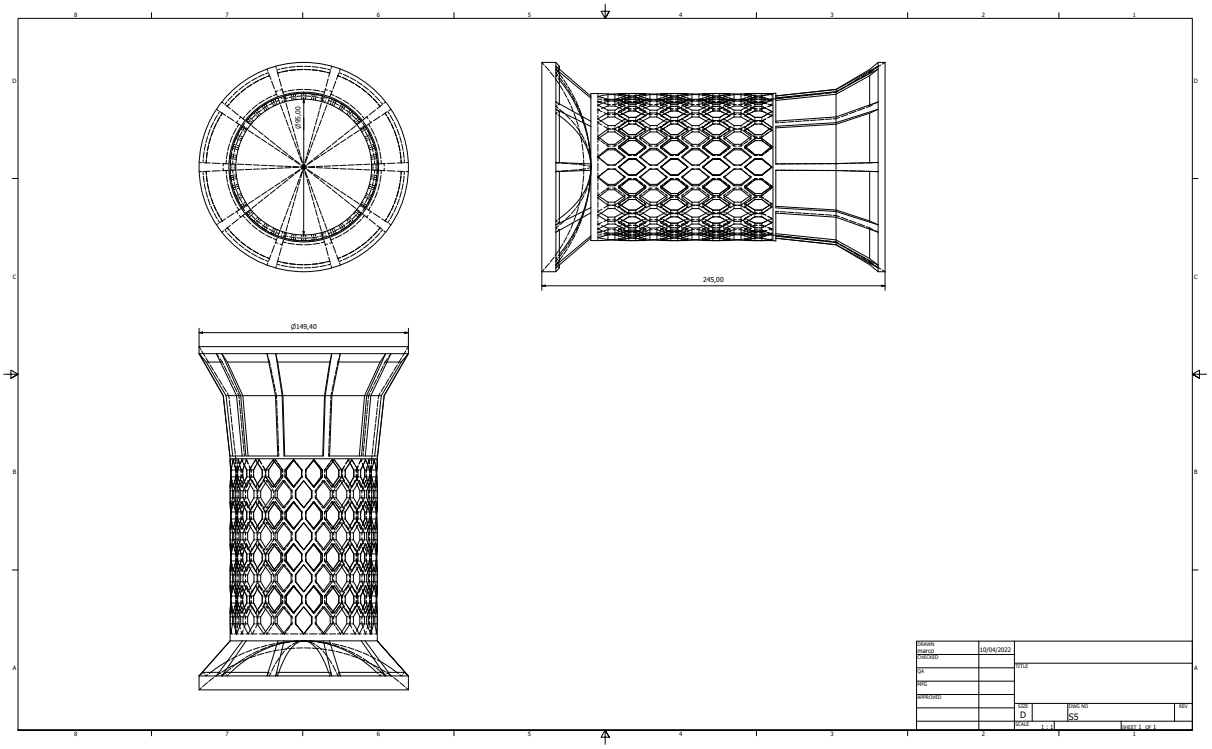

Figure 4.17: S_{05} Technical Drawing

Numerical Simulation N°6:

Simulation results unsatisfactory.

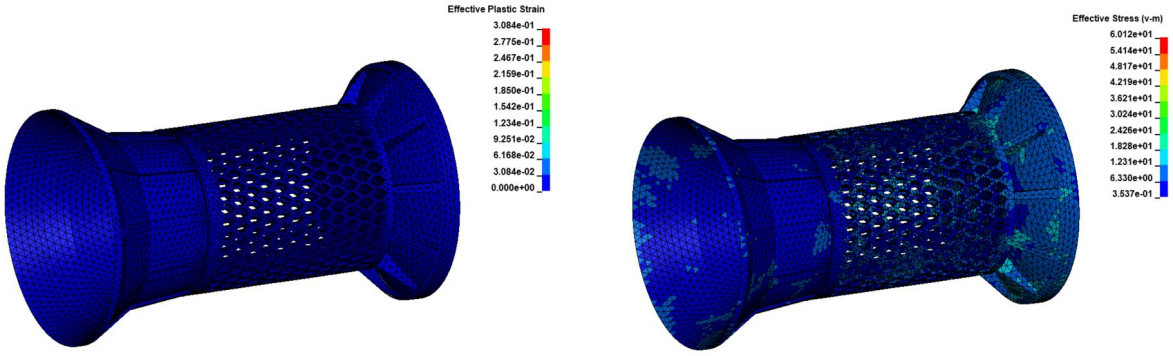

Figure 4.18: S_{06} Numerical Results

Design Label	Launch Pressure [bar]	Estimated Mass [g]	ϵ_{max} [%]	σ_{max} [MPa]
S_{06}	7	256	0.308	60.12

Table 4.6: S_{06} Simulation Data

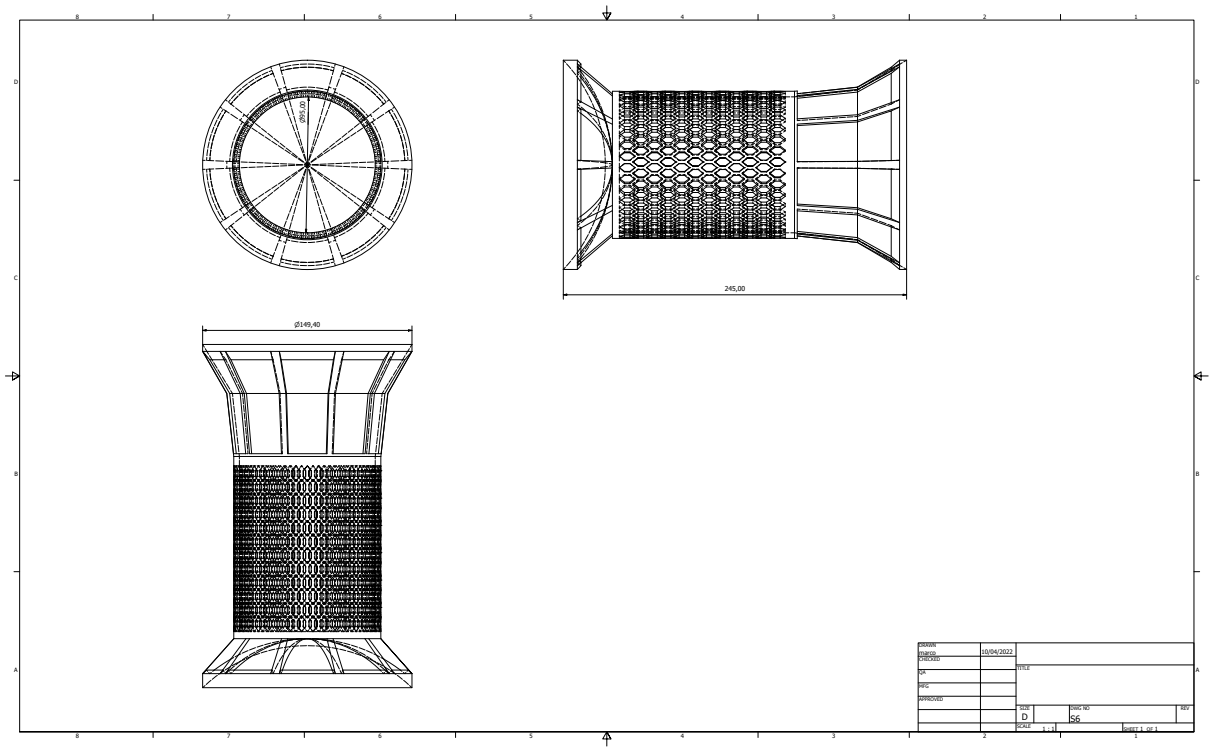

Figure 4.19: S_{06} Technical Drawing

Numerical Simulation N°7:

Simulation results satisfactory.

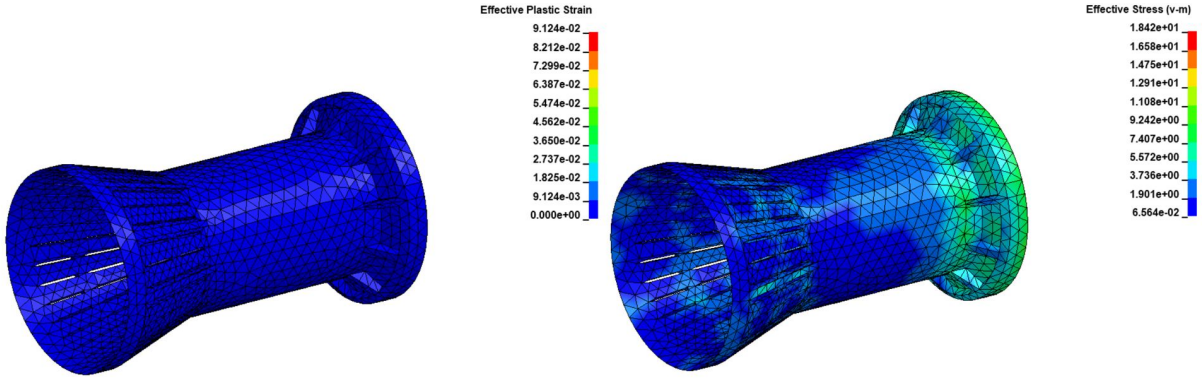

Figure 4.20: S_{07} Numerical Results

Design Label	Launch Pressure	Estimated Mass [g]	ϵ_{max} [%]	σ_{max} [MPa]
S_{07}	7	352	0.091	18.42

Table 4.7: S_{07} Simulation Data

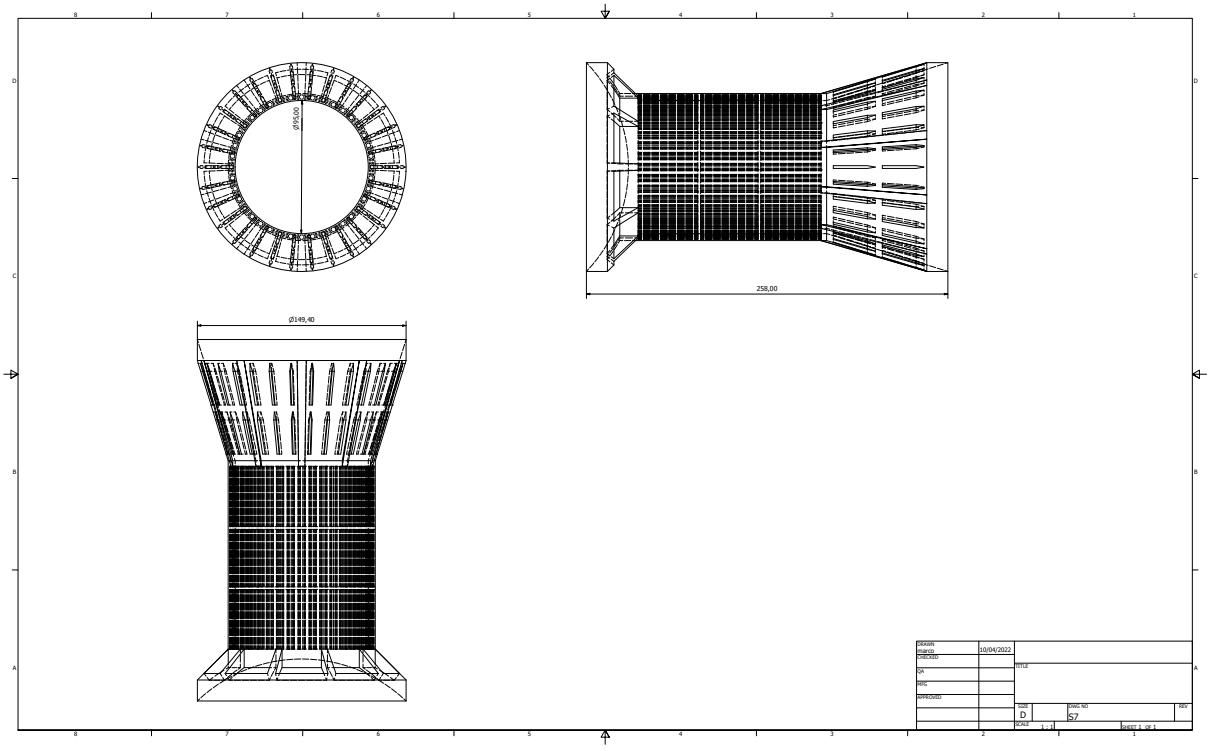

Figure 4.21: S_{07} Technical Drawing

Numerical Simulation N°8:

Simulation results satisfactory.

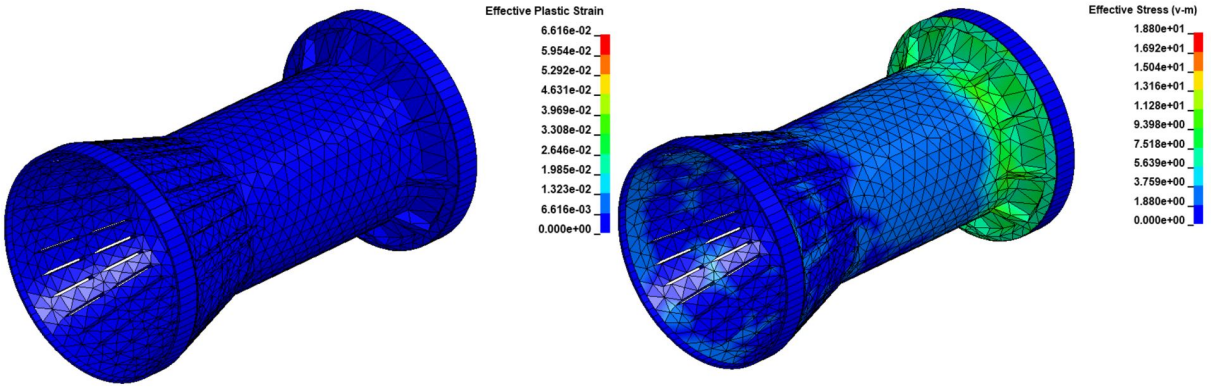

Figure 4.22: S_{08} Numerical Results

Design Label	Launch Pressure	Estimated Mass [g]	ϵ_{max} [%]	σ_{max} [MPa]
S_{08}	7	349	0.0661	18.8

Table 4.8: S_{08} Simulation Data

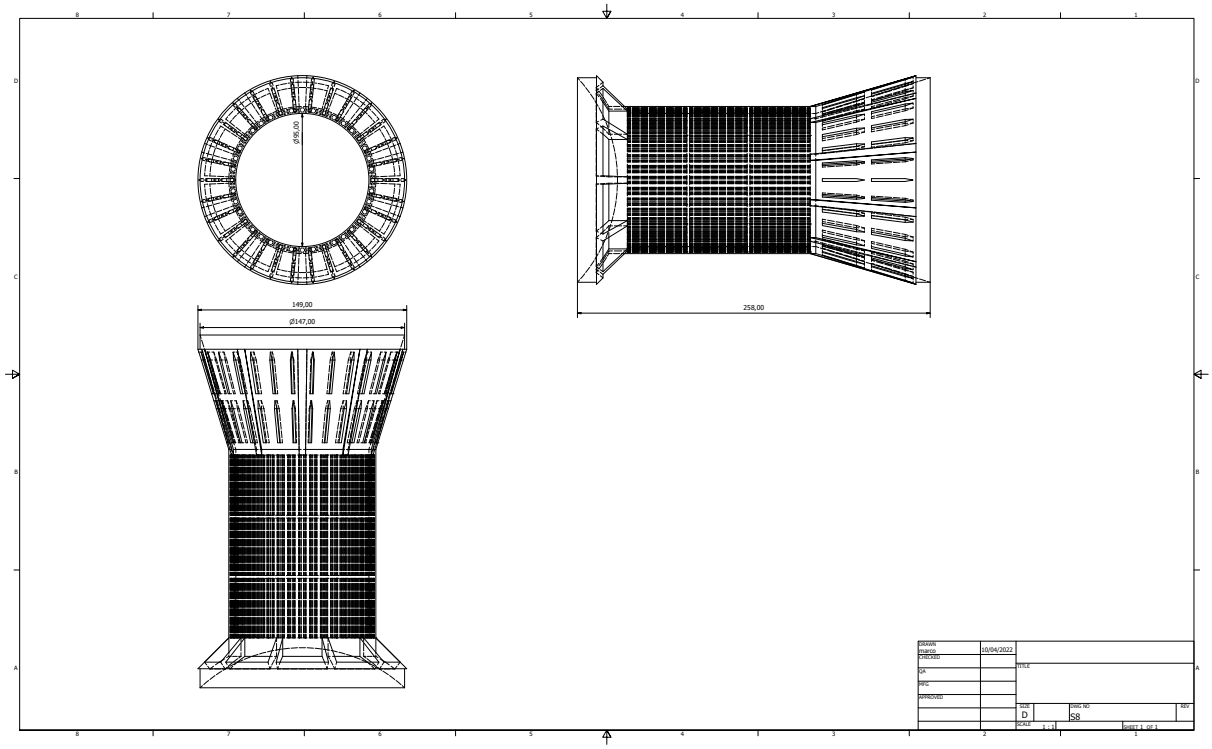

Figure 4.23: S_{08} Technical Drawing

Numerical Simulation N°9:

Simulation results unsatisfactory.

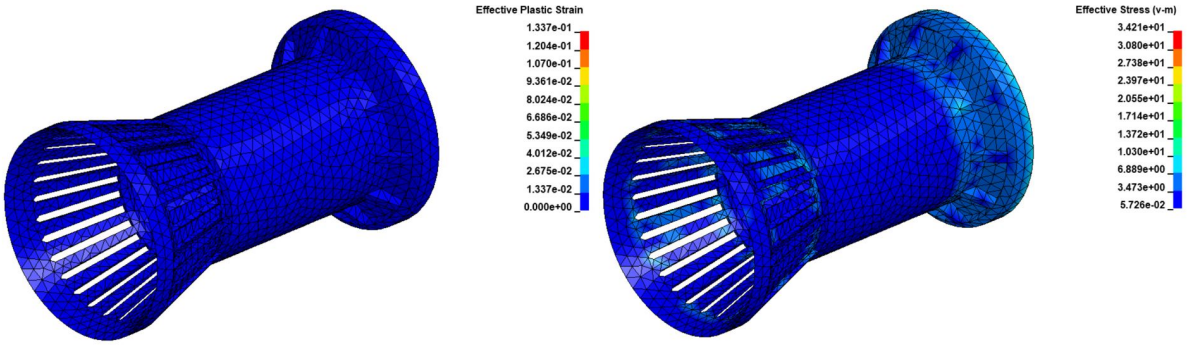

Figure 4.24: S_{09} Numerical Results

Design Label	Launch Pressure	Estimated Mass [g]	ϵ_{max} [%]	σ_{max} [MPa]
S_{09}	7	347	0.1337	34.21

Table 4.9: S_{09} Simulation Data

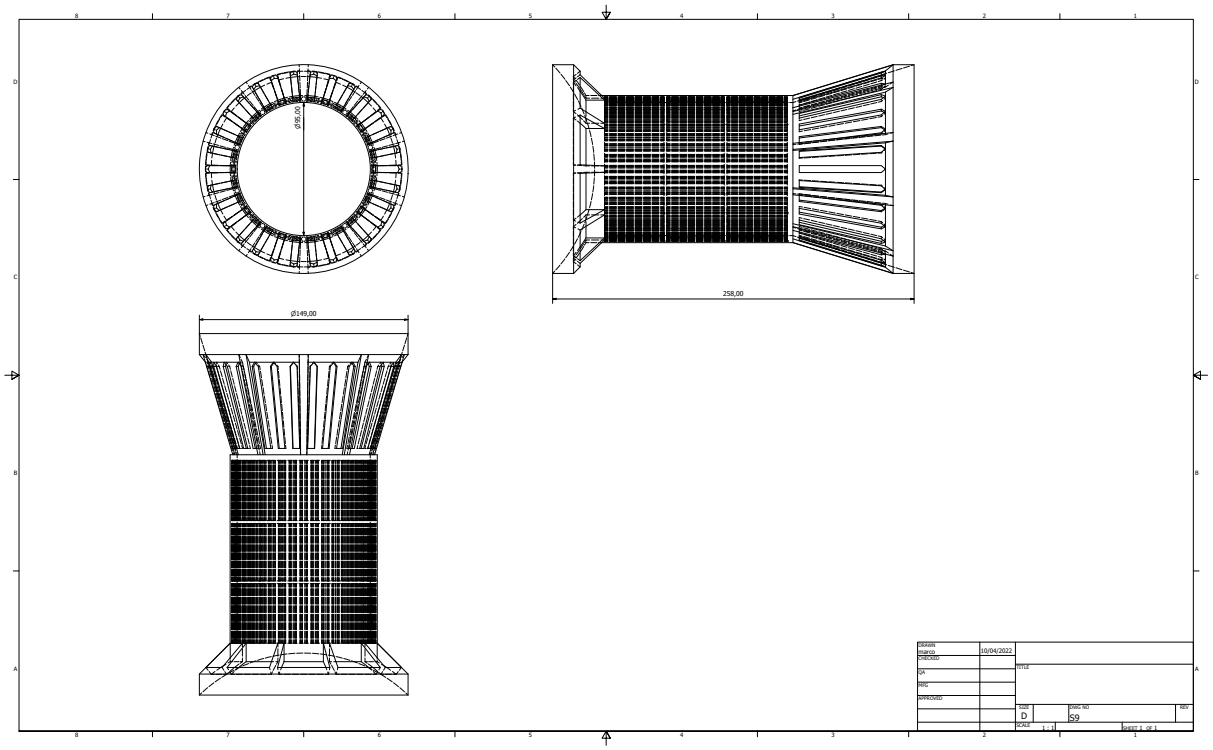

Figure 4.25: S_{09} Technical Drawing

Numerical Simulation N°10:

Simulation results satisfactory.

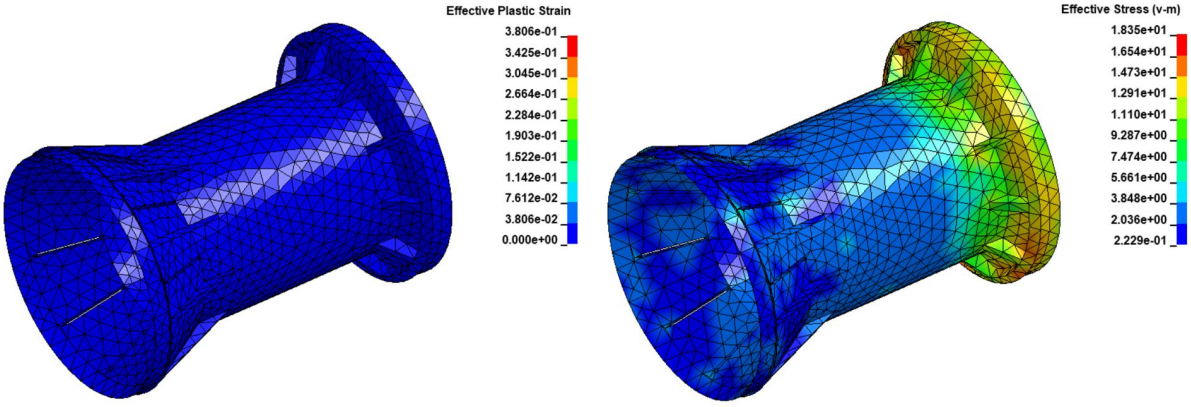

Figure 4.26: S_{10} Numerical Results

Design Label	Launch Pressure	Estimated Mass [g]	ϵ_{max} [%]	σ_{max} [MPa]
S_{10}	8	338	0.3806	18.35

Table 4.10: S_{10} Simulation Data

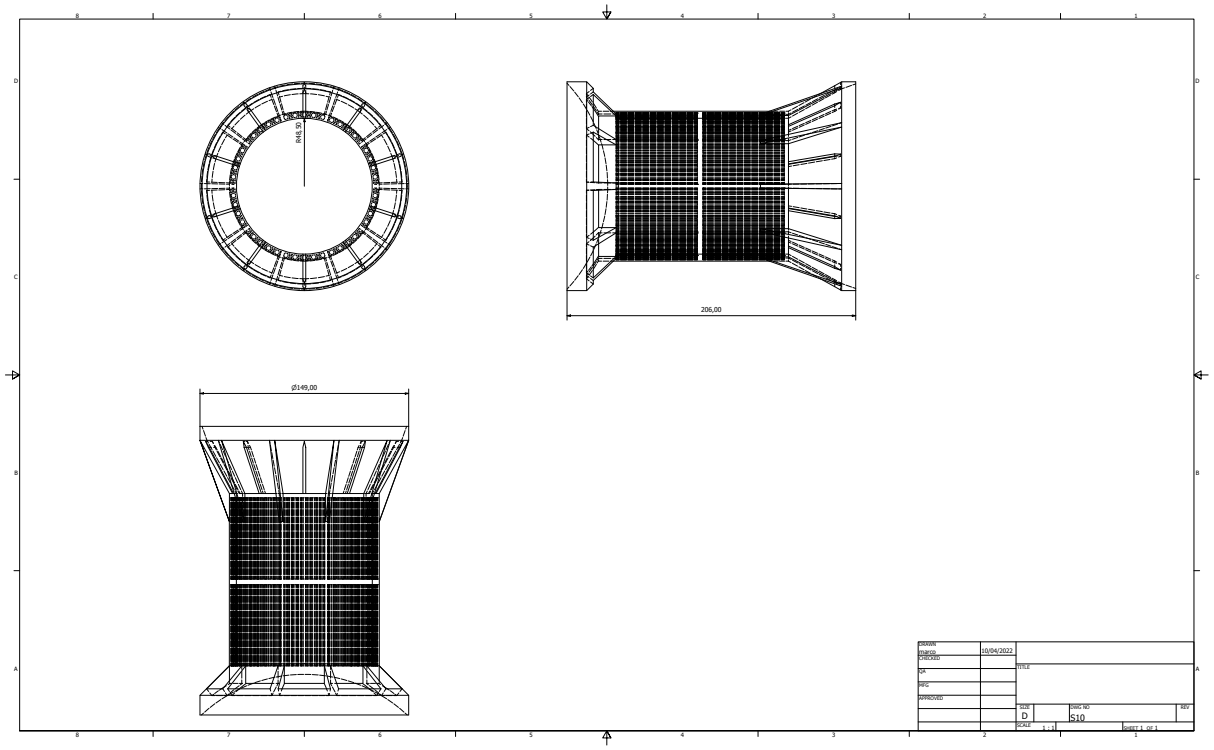

Figure 4.27: S_{10} Technical Drawing

Numerical Simulation N°11:

Simulation results satisfactory.

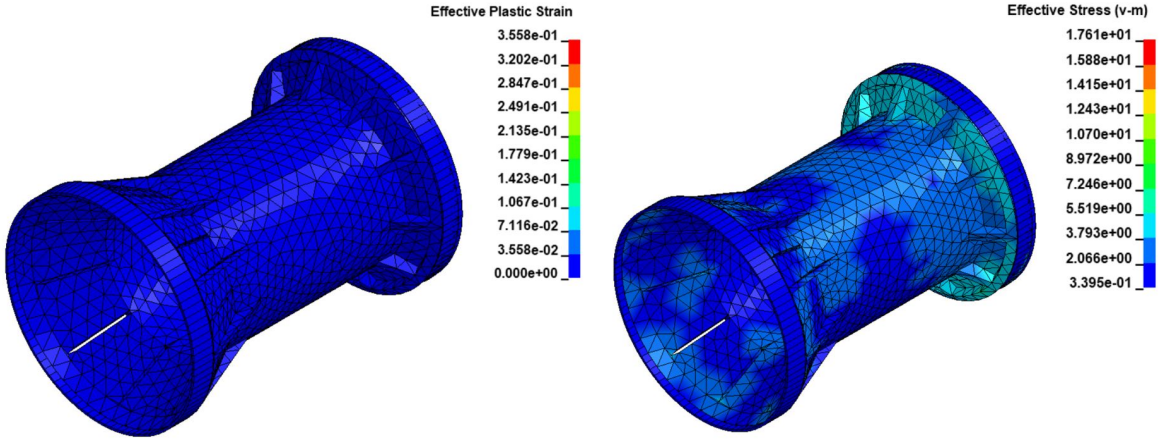

Figure 4.28: S_{11} Numerical Results

Design Label	Launch Pressure [bar]	Estimated Mass [g]	ϵ_{max} [%]	σ_{max} [MPa]
S_{11}	8	332	0.3558	17.62

Table 4.11: S_{11} Simulation Data

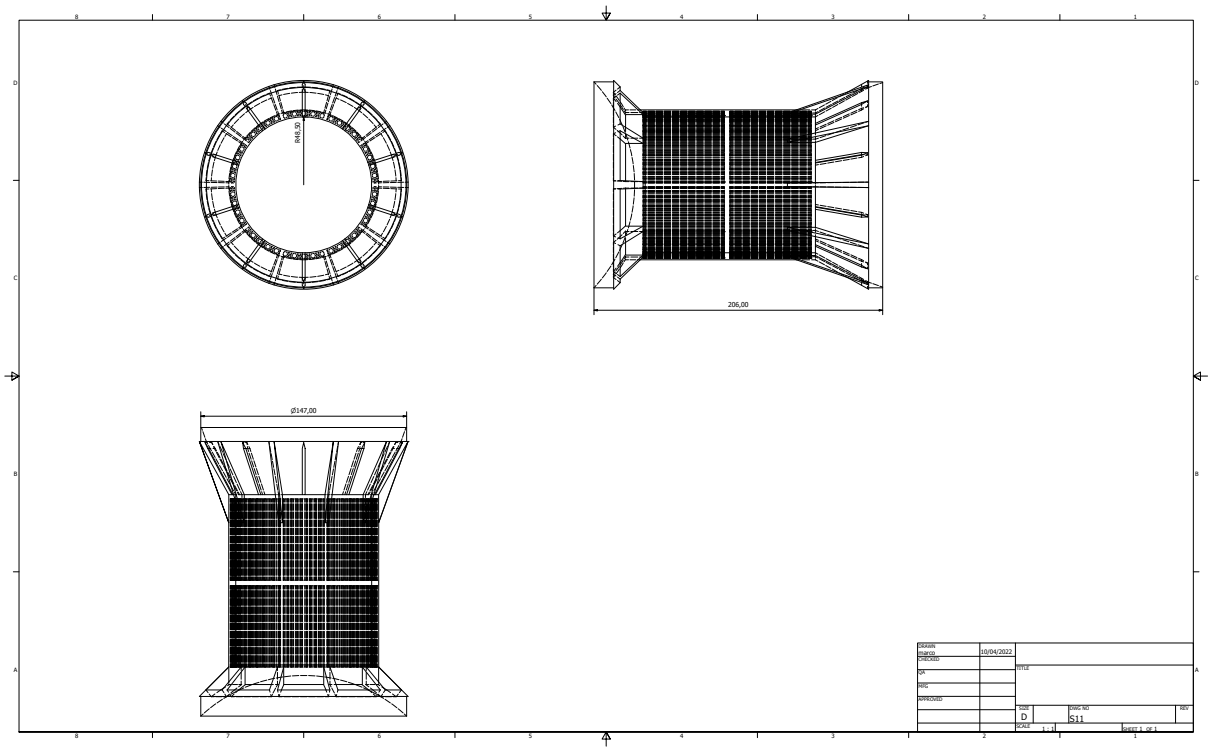

Figure 4.29: S_{11} Technical Drawing

4.1.4. Sabot Impact Numerical Model

As previously mentioned, the second F.E. model was developed with the aim of predicting at macroscopic level the sabot's failure mode at the moment of its impact against the stopper. This way it would be possible to know in advance if the designed piece is able to perform a correct separation from the bird (fundamental for the success of experimental tests), following the desired radial opening. Such analysis however doesn't allow to perform a control on the amount of debris generated by the impact, as in LS-DYNA® all failed elements are automatically eliminated from the simulation. The models consists of two distinct parts:

- **Stopper:**

The stopper was modelled with 2000 solid elements and (assuming it as non-deformable) a rigid material with steel properties was assigned to it. All displacements and rotations of the component were then constrained.

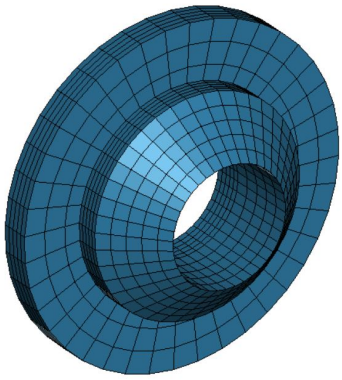

Figure 4.30: Stopper Model

- **Sabot:**

A single sabot impact simulation was performed using the sabot design labeled as S_{07}, the first to be prototyped and tested. The definition of the sabot's model is the same as the one previously used, exception made for the material assigned to the part. Due to the high speed at which the collision occurs between the sabot and the stopper, breakages and very large plastic deformations are expected. Therefore a different material was chosen, in order to better represent the real sabot's behavior. Material type 003 (or `*MAT_PLASTIC_KINEMATIC`, usually employed to model blast phenomena) is able to manage fracture development while considering strain rate and material's failure, thus suitable for high-speed impact applications. The corresponding material card was compiled with HIPS' properties.

Applied loads and contacts modeling has been instead kept the same as for the in-bore simulation, while to the sabot was assigned a speed (through the *`INITIAL_VELOCITY_GENERATION` card) equal to the one measured for the real S_{07} sabot in the experimental tests.

4.1.5. Sabot Impact Simulation Result

Simulation results show the evolution of the impact at different time instants (fig.4.31). From the initial impact phases it's possible to observe how the sabot tends to open up in the desired way. At later time instants the sabot's middle body is apparently cut by the stopper, leading to an excessive passage of debris along with the surrogate bird through the stopper.

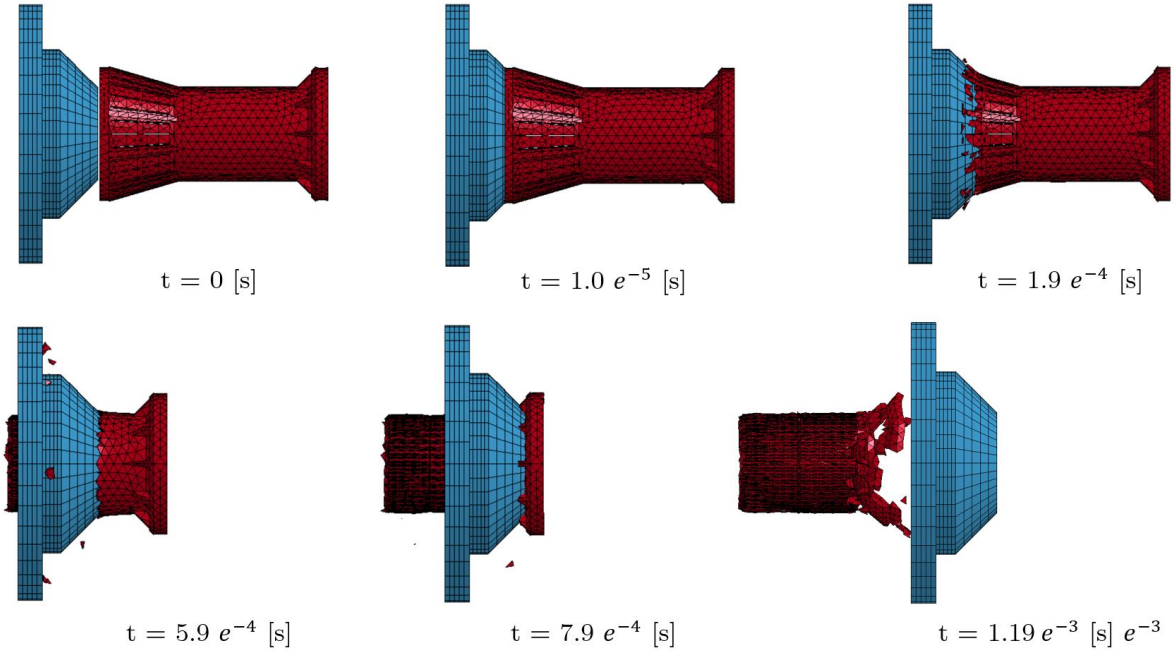

Figure 4.31: Sabot Impact Simulation

Moreover, due to the high speeds and forces involved, in the simulation problems of conpenetration between sabot's and stopper's material emerged. Further developing this F.E. analysis such problem could be solved by choosing a different contact type. Alternatively the formulation of the whole model should be changed, switching to an ALE or SPH method.

4.2. Prototype Production

4.2.1. Sabot

Preliminary sabot's designs which gave satisfactory numerical results were realized using FDM technology (Fuse Deposition Modeling) with a Delta Wasp 2040 3D printer (fig 4.32), at La.S.T. laboratory. This printer works using suitable thermoplastics, which are extruded through a heated nozzle and then deposited in the form of semi-molten filaments. Multiple layers are created starting from the printer's building plate and going upward until the pre-programmed piece is fully molded. The high degree of accuracy and repeatability of 3D printers makes them particularly suitable for the production of prototypes. Additionally, the 3D printing technology makes it possible to manufacture components [9] with "unique properties, very difficult to obtain by other methods, e.g., lightweight, hollowed-out elements with space-framed interiors."

Figure 4.32: Delta Wasp 3D Printer

However 3D printing also has limitations: not all thermoplastic materials can be printed, especially those with excessively high extrusion temperatures, since the printer's nozzle can only be heated up to 300 °C. Model's walls with overhang angles greater than 45° may not provide upper layers with a sufficient support base for the deposition of new filaments. In this case the next deposited layer tends to yield and fall, so the generation of appropriate supports is required. There is a risk of damaging the finished piece when removing these supports, so it is advisable to use them as little as possible. Moreover, for

the printing of some thermoplastics (including HIPs) it's necessary to use a specific glue to guarantee good adhesion between bottom layers and the printer's building plate. Such aspects related to the prototype production have been considered during the design phase and no printed preliminary designs have walls with an angle to the vertical higher than 45°, exception made for the spherical cap base. As mentioned in chapter 3, subsection 3.4.2, the spherical cap base was adopted to ensure an easy detachment of the sabot from the printer's building plate. In the past this operation has led to ruptures of the printed piece (see 3.15a), due to a flat base adhering too much to the building plate. Other drawbacks that need to be addressed when 3D printing are: weakness points between layers and uncontrolled shrink which might occur while the model cools down. For these reasons, special attention was paid to the production of 3D-printed parts, putting into practice all measures suggested by the Delta WASP 2040 User and Maintenance Manual [38], such as the pre-printing calibration and cold filament loading.

3D Printing Parameters and Slicing:

The quality of 3D printed parts, which can be assessed by mechanical properties, is strictly dependent on the selected print settings. It is possible to choose which and how many settings to use when printing through the slicing operation. Slicing consists in converting the designed CAD model (typically a .stl file) into a file containing all the information needed to 3D-print that specific model (also known as .gcode). Among all parameters, the .gcode also includes the path which the nozzle follows during the sequential build-up of each layer. Each setting affect different properties of the finished part, therefore the most important ones are hereby described and motivated.

- **Print Orientation** is the first aspect to consider before 3D-printing the sabot. Since every layer is deposited on top of the previous one, typically the bond between two successive layers is weaker than the extruded material's molecular bond. Because of this, tensile and shear loads tend to stress more the piece, leading to layer separation with a delamination-like failure mode [26]. Considering that the sabot is mainly subject to compressive loads during its acceleration at launch, the print orientation must deposit layers on a plane always perpendicular to the sabot's longitudinal axis, as shown in fig.4.33.

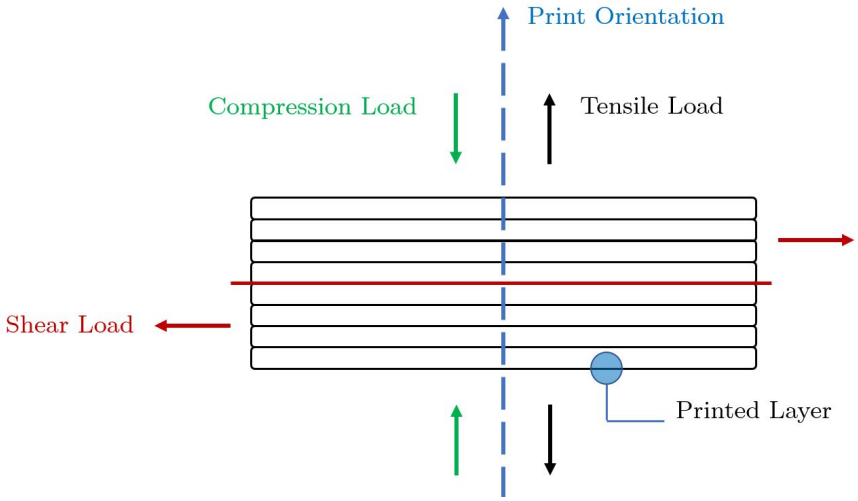

Figure 4.33: Best Print Orientation

- **Layer Height** does not significantly affect the strength of the final piece, although smaller heights result in longer print times and extra deposited material. Therefore, within the typical range going from 0.1 to 0.5 mm, a value of 0.3 mm was selected to contain the amount of material used and the weight.

- **Layer Thickness** it's a parameter that if increased it has been proven to lead to more robust parts, instead it determines a greater surface finish when reduced. Since the sabot has few contact surfaces, a certain roughness of these surfaces is tolerable, so the thickness of the layers has been set to high values, between 0.8 and 1.0 mm.

- **Infill** is one of the most important printing parameters as it serves as the internal support structure that aims to keep the outer walls together, adding stiffness to the sabot. Little infill leads to excessive deformation, lower print quality and less success of the part. The 3D infill patterns typically range from 30% to 50% in density, in this case the internal stiffness of the sabot has been preferred at the expense of its weight by setting the infill to 50%.

- **Infill Pattern** is an additional setting that defines the internal geometry that the internal structure of the sabot will assume. Given the versatility of FDM technology, it's possible to use a variety of different geometries (some of which are shown in fig.4.38), among these was chosen a line pattern infill (fig. 4.34a) as it allows to reach a high infill density (50%) without printing errors and it also ensures to

be easily employed in all sabot's various configurations. Furthermore 3D-printed polymers with a linear infill have been proved to confer an orthotropic behavior to the piece [34].

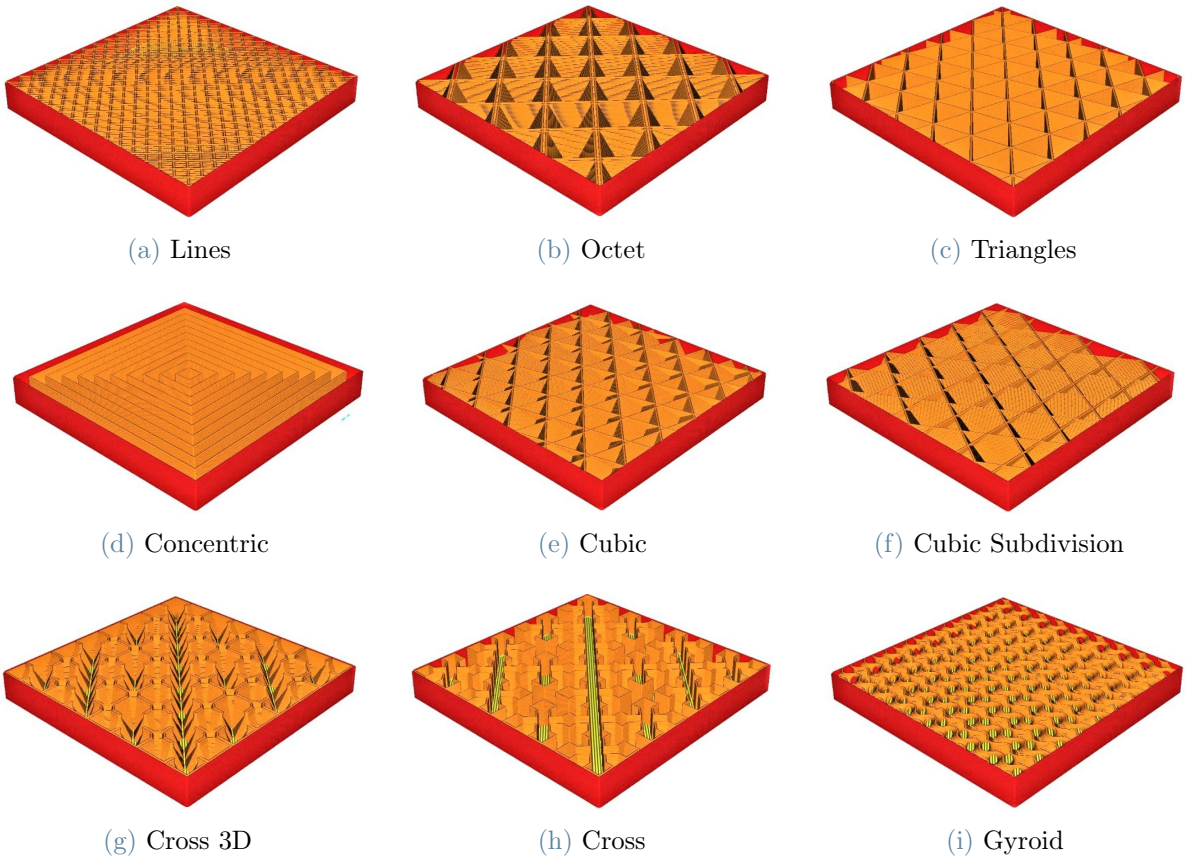

(a) Lines (b) Octet (c) Triangles

(d) Concentric (e) Cubic (f) Cubic Subdivision

(g) Cross 3D (h) Cross (i) Gyroid

Figure 4.34: Different Infill Patterns

Mass Estimation:
The chosen printing settings (in particular infill percentage and pattern) affect the final mass of the sabot. Once a preliminary design is executed, known its volume and material, estimating its mass as $M = V \cdot \rho$ doesn't provide an accurate value, which is instead desired to perform a reliable mass reduction process. A more precise mass estimate is obtained considering the wanted filling, depending on the different geometries, for each individual preliminary design.

4.2.2. Surrogate Bird

The surrogate bird in order to comply with the certification standards must always have a weight of about 1kg, therefore it's the projectile's component responsible for more than

70% of its total weight. Dummy birds are also produced at La.S.T. laboratory by carrying out the following procedure:

STEP 1: The PERMAGEL® gelatin is unboxed and fragmented into several pieces, so as to be placed inside a dedicated furnace (fig.4.35).

(a) (b)

Figure 4.35: Unprocessed PERMAGEL®

STEP 2: The furnace is turned on, setting it to a temperature of 120 ^{o}C. From the moment the desired temperature is reached, it will take 6 hours for the ballistic gelatin to melt completely. During this phase it's of particularly importance to keep the furnace always closed so that no impurities enter. In addition, before proceeding to the next step, it's essential to ensure that there are no air bubbles in the dissolved gelatin. If this is not the case, it will be necessary to wait longer than the indicated 6 hours for these to be released.

STEP 3: Once the gelatin has correctly melted, it's then possible to turn off the furnace and to introduce special cylindrical moulds for the dummy-birds. Such moulds have the internal diameter equal to that of the final surrogate bird, but they generally have a longer length. When introducing the moulds into the melted gelatin, it was made sure that no air remained trapped inside the moulds, but that they were completely filled and covered by PERMAGEL® as in fig.4.36. Once the moulds are positioned, it is necessary to wait

for the curing time of the gelatin, which typically takes 12 hours to re-solidify.

Figure 4.36: Submerged Moulds

STEP 4: When the PERMAGEL® is fully solidified the molds can be extracted and opened, retrieving the gelatin blocks (fig.4.37). However, the latter are longer and heavier than the desired dummy-birds. Therefore, the procedure involves gradually cutting their ends, until a mass of about 1 Kg is reached.

Figure 4.37: Gelatin Cylindrical Blocks

STEP 4: The last step of this procedure consists in wrapping each individual surrogate bird at first with layers of American tape (fig.4.38a), and then using paper tape (fig.4.38b).

(a) American Tape (b) Paper Tape

Figure 4.38: Surrogate Bird Wrapping

Once the surrogate birds are produced their final mass is measured by weighting them once again. The obtained masses are hereby provided among with the respective experimental test in which each bird was employed:

Experimental Test:	**Surrogate Bird's Mass:** $[g]$
Test 1	962
Test 2	982
Test 3	949
Test 4	964
Test 5	1033
Test 6	994
Test 7	999

Table 4.12: Surrogate Birds' Mass

4.2.3. Teflon Rings

As explained in chapter 3, subsection 3.3.4, one way to achieve friction reduction is to employ Teflon rings which shall act as bearings between barrel and sabot. The production of these rings was carried out at La.S.T. laboratory starting from a uniform Teflon plate of dimensions: 1200x50x1 mm. Being the original plate extremely thin and flexible, it has been wound on itself. Doing so an initial curvature was conferred to the whole plate. Strips of material were then cut using a circular saw while holding the work-piece in place via a vise, as shown in fig. 4.39. The obtained results show high dimensional accuracy, matching the desired nominal dimensions for each strip (respectively 10 and 15 mm in width) within $\pm$ 0.05 mm.

(a) Ring Cut n°1 (b) Ring Cut n°2

Figure 4.39: Performed Teflon Cuts

Further cuts are made to obtain teflon strips of the right length, equal to the nominal outer circumference of the sabot ($C_{outer} \approx 468$ $[mm]$) , so that they can be properly wrapped on them. The obtained teflon parts constituting the rings have then been weighted (fig.4.40), the mass of each teflon bearing is reported in the table 4.13 along with the sabot's prototype ID onto which it will be applied during the assembly phase.

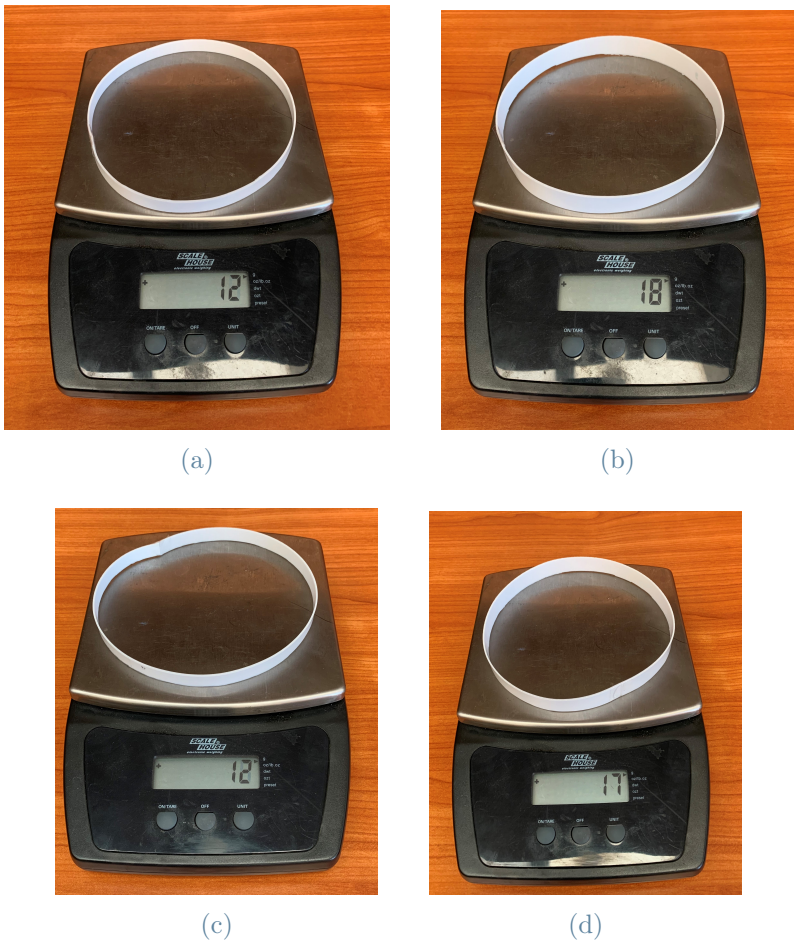

(a) (b)

(c) (d)

Figure 4.40: Teflon Rings

Teflon Ring:	Prototype ID:	Mass: $[g]$
Ring 1 (fig.4.40a)	P_{06}	12
Ring 2 (fig.4.40b)	P_{06}	18
Ring 3 (fig.4.40c)	P_{07}	12
Ring 4 (fig.4.40d)	P_{07}	17

Table 4.13: Teflon Rings' Mass

4.2.4. Prototype and Projectile Assembly

For those prototypes that require Teflon rings, an assembly is performed in order to ensure a good seal between the bearings and the sabot (fig.4.41). As previously mentioned, it's not easy to attach the Teflon rings to the HIPs material of the sabot, being discouraged soldering techniques and given the high chemical inertia of Teflon. Despite the difficulties involved in the processing of this material, gluing was chosen as the joining method.

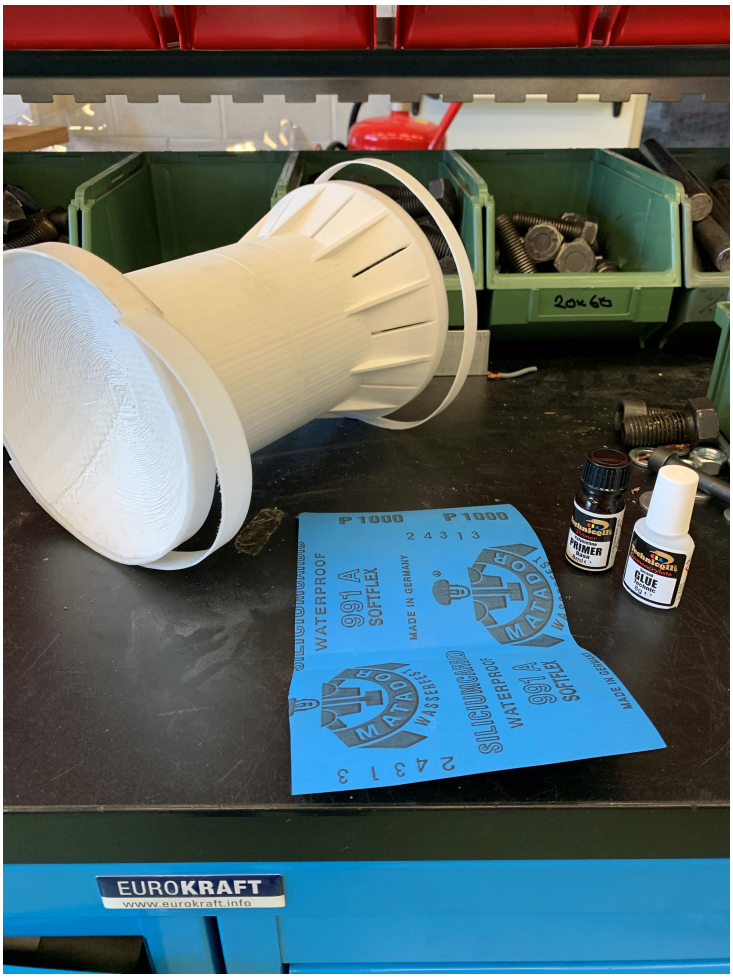

Figure 4.41: Prototype Assembly

However, in order to achieve a bonding that holds, it's necessary to properly treat the PTFE material at first. All Teflon rings were therefore first sanded down, on the side that shall adhere to the sabot, using a very fine sand paper (P1000). This allows to locally increase the roughness of the material, without generating an abrupt surface and letting that same surface be coated as much as possible by the bonding agents which will be later applied.

After a thorough research, cyanoacrylate was selected as an appropriate adhesive. Cyanoacrylates are industrial-grade bonding agents which stand out among various classes of adhesives. They are suitable for bonding a variety of materials, especially hard thermoplastics, and have the advantage of requiring a very short application time (they're indeed classified as instant bonding adhesives). Another great advantage is that their bonding process cure at ambient temperature, without requiring any additional or external energy. Despite these excellent properties cyanoacrylate itself is not able to establish a lasting joint.

It is in fact necessary to apply a Polyolefin-based primer on the PTFE, the purpose of which is to activate the surface to be glued, making it more receptive and reinforcing the power of the adhesive itself. So, in order to create a stronger bond, a thin primer film is then applied to the inner surface of each ring using a small brush. After the PTFE piece is allowed to stand and dry for about 8 minutes, the cyanoacrylate adhesive is applied in the same manner. Then the teflon rings are immediately placed in the respective housings on the Sabot obtaining the final two-material prototype.

After all sabot's prototypes (with or without Teflon bearings) have been manufactured, the last step to obtain a full projectile ready to be fired consists in inserting a surrogate bird inside each prototype.

4.3. Experimental Tests

This section illustrates all standard procedures and instrumentation used to perform bird impact tests, all executed shots for different case studies and their respective experimental results are then presented. It is reminded that whenever executing these tests particular attention must always be paid to safety.

4.3.1. Test Equipment

All bird-strike tests have been conducted at La.S.T. Laboratory of *Politecnico di Milano* inside the dedicated ballistic test range, constituted of a room which houses the launching system described in Chapter 2. In order guarantee safety at all time, tests are performed only when the cannon's room is sealed and free from any personnel. The firing of the single-stage gas gun is triggered operating a control panel, shown in fig.(4.42), placed outside the test range.

Figure 4.42: Exterior Control Panel

Other important equipment necessary for carrying out experimental tests is:

1. **High Speed Cameras:**
   High speed cameras are among the most essential tools for testing, as they are able to capture the separation of the surrogate bird from the sabot when exiting the barrel, the sabot's fracturing against the stopper and the collision of the dummy bird on the target. All these events are of extreme interest but they only take few milliseconds to occur, at such high velocities they can't be caught by the naked eye. Besides from providing clear images of such phenomena, high speed cameras are also essential to monitor debris generation from the sabot's rupturing, to measure the velocity of the surrogate bird, its attitude and its behaviour when traveling from the stopper to the target. In all tests two different cameras have been used: the Phantom® V210 in fig.4.43a, and the Phantom® VEO E-310L in fig.4.43b.

(a) Phantom® V210. (b) Phantom® VEO E-310L.

Figure 4.43: High Speed Cameras

Both cameras have an adjustable resolution and frame rate, which are set accordingly to tests' requirements. These two settings are inversely proportional to each other; it is therefore appropriate to carry out a trade-off based on the specific test case. Since the sabot is expected to travel at high speed it's desirable to set the highest possible frame-rate, this was achieved by reducing the frame resolution.
All adopted settings in every performed test are reported in Table 4.14 for both cameras. Camera 1 (Phantom® V210) was placed in front of the target, while camera 2 (Phantom® VEO E-310L) was positioned at the exit of the cannon's barrel. Note that from experimental test N°4 onward, both cameras were VEO E-310L.

	Resolution		**Frame-Rate**	
	Camera 1	**Camera 2**	**Camera 1**	**Camera 2**
Test 1	608x600	576x144	5600	36000
Test 2	608x600	576x144	5600	36000
Test 3	608x600	576x144	5600	36000
Test 4	832x600	1024x264	6400	12000
Test 5	832x600	896x256	6400	14000
Test 6	832x600	896x256	6400	14000
Test 7	832x600	1024x264	6400	12000

Table 4.14: Cameras' Settings

These high speed cameras present many useful features, among them there is the Image-Based Auto-Trigger which places the cameras in an alert state, starting both recordings simultaneously in a circular buffer, this allows to catch the whole phenomenon in its entirety without losing any detail and without the need to manually trigger the cameras. This function will be exploited in section 4.3.2 since it is part of the test's standard procedure.

2. **Lighting System:**
   Due to the very high frame rate in order to obtain a good visualization from the cameras' recordings both the stopper and the target must have proper lightning. For this purpose, a lighting system consisting of a LED wall is used. The LED lights are subdivided into 9 orientable lamps as shown in fig.4.44:

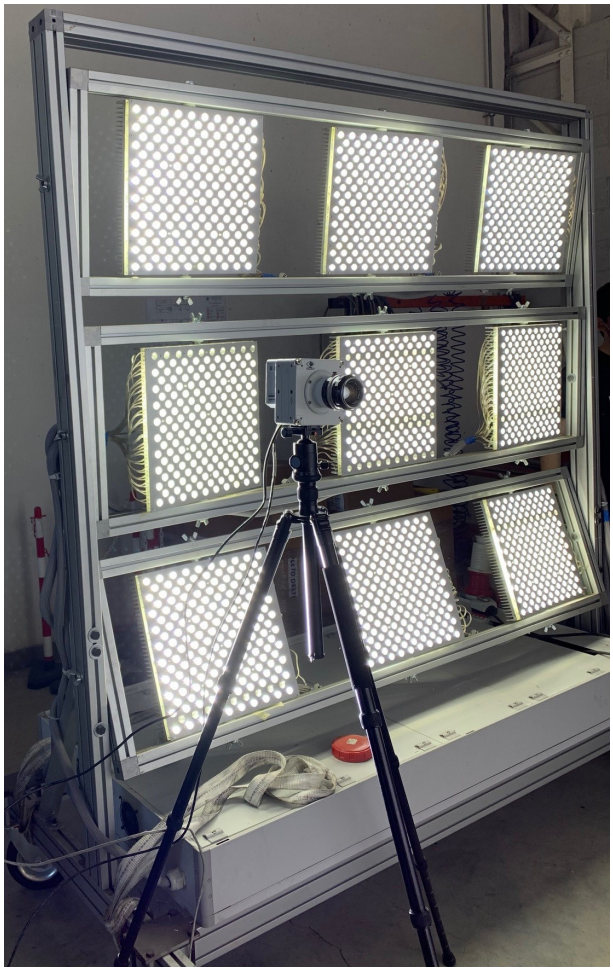

Figure 4.44: Lightning System

3. **Containment Cage:**
   When the dummy-bird hits the target at high velocity the impact force is so strong that fragments of ballistic Permagel® gelatin are radially redirected from the target towards the outside. These debris continue to have a sustained speed even after the impact and they might cause damages to the equipment in the test room, especially to the high speed cameras. Therefore, to mitigate this risk, a containment cage is placed right in front of the gun's barrel, enclosing the hole target as in fig.4.45:

Figure 4.45: Containment Cage

Since the cage consists of three metal grids which are not welded to one another, these are held together by dedicated plastic zip ties (fig.4.46). Given that after a shot one or more ties may break, it is advisable to check their state and eventually replace them in between two tests.

Figure 4.46: Plastic Zip Ties

4. **Scales:**
   As mentioned in section x it is important to correctly measure the effective sabot's mass using a scale. This measurement is repeated before each shot, and is aimed not only at double-checking the mass of the sabot, but also at assessing the mass of the dummy-bird and the total mass of the projectile which is about to be shot. It is to be noted that the surrogate bird's mass is not exactly constant, but varies slightly from piece to piece. This is due to the fact that their manufacturing technique does not guarantee excessive accuracy, hence the importance of the pre-launch measurements.

4.3.2. Test Setup

In order to carry out the experimental tests, all the necessary equipment must be properly set up and prepared. The standard procedure for performing a launch involves the following steps:

1. **Loading operation:** the barrel is separated from the fitting with the fast acting valve and the sabot-bird package is inserted. Afterwards particular attention is paid during components' re-connection, when placing the gasket and tightening all joint's bolts.
2. **Test range evacuation:** all personnel leave the firing area, moving to another space from where it's possible to control both launch and data acquisition systems.
3. **Acquisition arming:** the video acquisition system is set on alert state by activating the pre-trigger function.
4. **Tank pressurization:** La.S.T. laboratory pressurization system is operated, providing compressed air to the launch system's pressure reservoir.
5. **Firing:** once the desired launch pressure has been reached, the cannon is triggered from its dedicated control panel. At the same time, the trigger for the video acquisition is also activated.

4.3.3. Test Cases

A total of 7 experimental tests were performed during the development of the new sabot, below are reported all the test cases and their respective parameters, which characterize both the sabot and the surrogate bird employed in each launch. For high speed cameras' settings used in the various tests, please refer to table 4.14.

Test Case N°1:

(a) Sabot (b) Surrogate Bird

Figure 4.47: Sabot & Surrogate Bird for Test N°1

Sabot Design Label:	S_{00} (Original Sabot)
Launch Pressure [bar]	7
Sabot Mass: [g]	455
Surrogate Bird Mass: [g]	962
Total Mass: [g]	1417

Table 4.15: Parameters for Experimental Test N°1

Test Case N°2:

(a) Sabot (b) Surrogate Bird

Figure 4.48: Sabot & Surrogate Bird for Test N°2

Sabot Design Label:	S_{00} (Original Sabot)
Launch Pressure [bar]	7
Sabot Mass: [g]	457
Surrogate Bird Mass: [g]	982
Total Mass: [g]	1439

Table 4.16: Parameters for Experimental Test N°2

Test Case N°3:

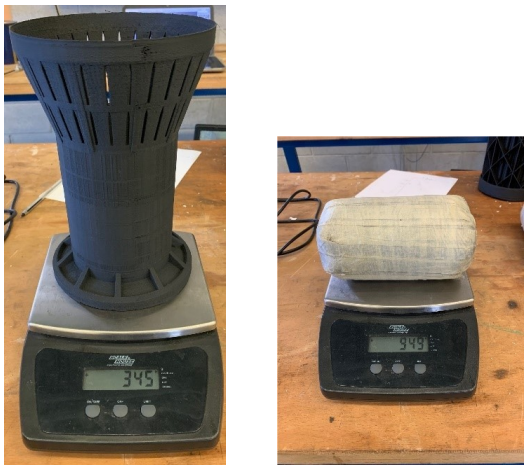

(a) Sabot (b) Surrogate Bird

Figure 4.49: Sabot & Surrogate Bird for Test N°3

Sabot Design Label:	S_{07}
Launch Pressure [bar]	7
Sabot Mass: [g]	345
Surrogate Bird Mass: [g]	949
Total Mass: [g]	1294

Table 4.17: Parameters for Experimental Test N°3

Test Case N°4:

(a) Sabot (b) Surrogate Bird

Figure 4.50: Sabot & Surrogate Bird for Test N°4

Sabot Design Label:	S_{07}
Launch Pressure [bar]	7.5
Sabot Mass: [g]	344
Surrogate Bird Mass: [g]	964
Total Mass: [g]	1308

Table 4.18: Parameters for Experimental Test N°4

Test Case N°5:

(a) Sabot (b) Surrogate Bird

Figure 4.51: Sabot & Surrogate Bird for Test N°5

Sabot Design Label:	S_{07}
Launch Pressure [bar]	8
Sabot Mass: [g]	352
Surrogate Bird Mass: [g]	1033
Total Mass: [g]	1385

Table 4.19: Parameters for Experimental Test N°5

Test Case N°6:

(a) Sabot (b) Surrogate Bird

Figure 4.52: Sabot & Surrogate Bird for Test N°6

Sabot Design Label:	S_{11}
Launch Pressure [bar]	7.5
Sabot + Teflon Rings Mass: [g]	353
Surrogate Bird Mass: [g]	994
Total Mass: [g]	1347

Table 4.20: Parameters for Experimental Test N°6

Test Case N°7:

(a) Sabot (b) Surrogate Bird

Figure 4.53: Sabot & Surrogate Bird for Test N°7

Sabot Design Label:	S_{11}
Launch Pressure [bar]	8
Sabot + Teflon Rings Mass: [g]	356
Surrogate Bird Mass: [g]	999
Total Mass: [g]	1355

Table 4.21: Parameters for Experimental Test N7

5 | Results and Discussion

The following are the results obtained from the experimental tests carried out at the La.S.T. laboratory for all considered test cases.

5.1. Velocity Measurements

By analyzing the recordings captured by the high-speed cameras, it's possible to calculate the projectile's velocity when exiting the cannon. The most significant results are obtained from the first camera's videos (framing the barrel's exit), as they allow to evaluate nozzle speed, separation quality, debris generation and the projectile's orientation in the following instants. The methodology adopted to compute the speed exploits the image processing software Phantom Cine Viewer®. In such environment it's possible to perform a calibration (fig.5.1) by associating the number of pixels between two fixed points on the gun barrel to the respective distance experimentally measured (equal to 480 $[mm]$).

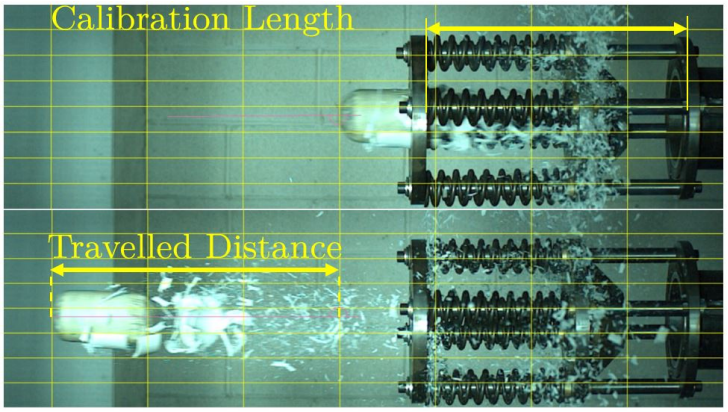

Figure 5.1: High Speed Recordings Calibration

Once a calibration scale ($[mm/pix]$) is defined, speed can be determined by identifying two points for which the dummy-bird passes at two different image frames. The software then extrapolates time and travelled distance between the two identified points, giving as output the projectile's speed value. Since the calibration operation is performed man-

ually, errors may occur when selecting points on video. To mitigate possible systematic errors which might affect the final speed value, 10 calibrations and 10 measurements were performed per test. The average speed value was then taken as the most reliable measurement and compared with the theoretical one. Such theoretical velocity is defined as the velocity that the projectile would have in the ideal case of a launching system without any energy loss (that is, if the efficiency of the whole launching system was equal to $\eta = 1$). The theoretical values are determined using the simplified formula:

$$V_T = \sqrt{\frac{P \cdot A \cdot L}{m}} \tag{5.1}$$

Where:

$$\begin{cases} P\ [Pa] = \textit{Launch Pressure} & \text{(5.2a)} \\ A\ [m^2] = \textit{Area upon which the Pressure acts on Sabot} & \text{(5.2b)} \\ L\ [m] = \textit{Barrel's Length} & \text{(5.2c)} \\ m\ [Kg] = \textit{Projectile+Sabot mass} & \text{(5.2d)} \end{cases}$$

5.2. Experimental Results:

EXPERIMENTAL TEST N°1:

This test was performed in order to obtain reference values in terms of speed, launching the original sabot (S_{00}) at a pressure of 7 [bar]. However, due to the sudden opening of a valve during the compression phase of the 1000 litres tank, the launching system misfired at a pressure ranging between 3 and 4 [bar].

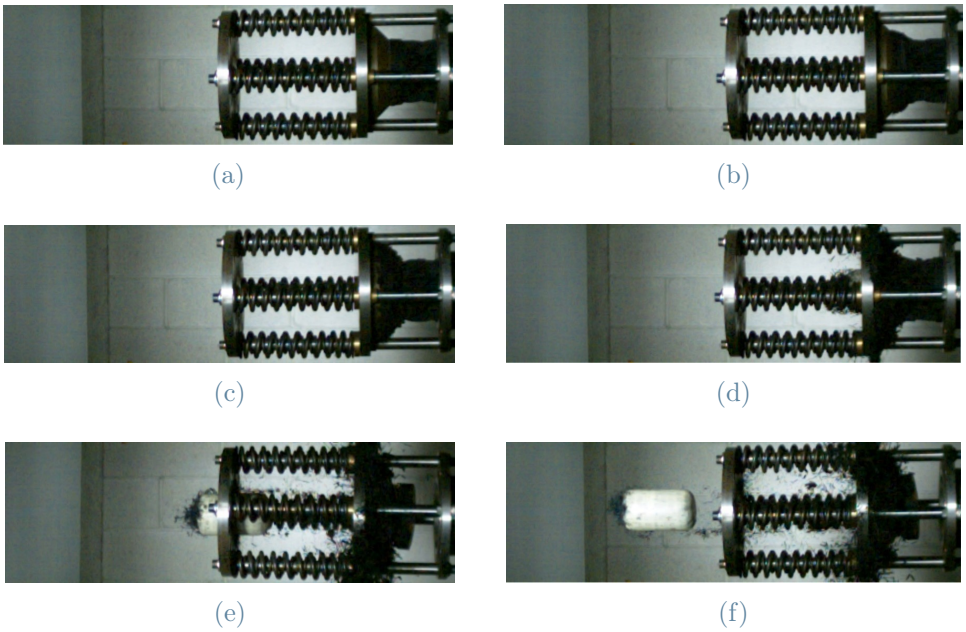

(a) (b) (c) (d) (e) (f)

Figure 5.2: Test N°1 Separation Phase

From this experimental test it was still possible to measure the value of the exit speed (as reported in table 5.1), even if it wasn't taken as the reference speed value for the original sabot. In the separation phase it's possible to observe the formation of a considerable amount of sabot's debris in the front of the projectile (fig.5.2e & 5.2f). Such condition is strongly undesired, as it implies that tested aircraft components are hit first by debris and not by the surrogate bird, affecting the outcome of any certification tests. Despite the low launch pressure, and therefore the low speed reached, it's appreciable how the dummy bird behaves as a fluid when impacting the target, as shown in fig. 5.3

Calibration Scale $[mm/pix]$	Projectile Velocity $[m/s]$
2.192	74.309
2.189	74.144
2.201	75.204
2.197	74.722
2.216	76.230
2.214	75.783
2.203	75.298
2.199	75.053
2.214	75.783
2.197	74.722
Average Projectile Velocity $[m/s]$	Theoretical Projectile Velocity $[m/s]$
75	167.5

Table 5.1: Test N°1 Speed Measurement

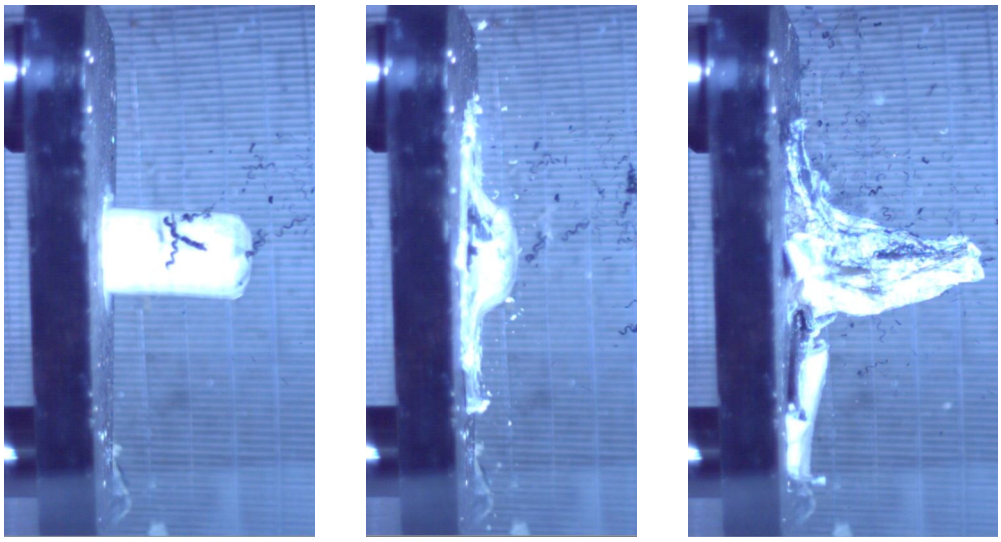

(a) (b) (c)

Figure 5.3: Test N°1 Impact Phase

EXPERIMENTAL TEST N°2:

The second test successfully provided a reference value for the maximum speed achievable with the original sabot using a launch pressure of 7 [bar].

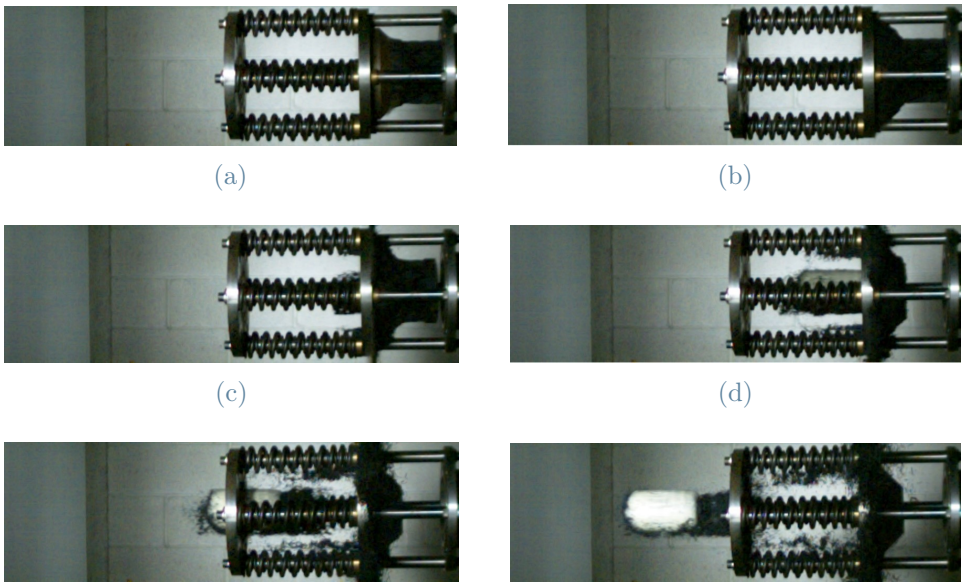

(a) (b) (c) (d) (e) (f)

Figure 5.4: Test N°2 Separation Phase

Once again, the presence of debris can be observed in the projectile's frontal area (fig.5.4e & 5.4f), although in smaller quantities with respect to Test N°1.

Calibration Scale $[mm/pix]$	Projectile Velocity $[m/s]$
2.182	221.525
2.201	226.394
2.200	226.291
2.198	224.970
2.199	225.175
2.208	226.715
2.218	228.295
2.220	228.425
2.215	227.145
2.199	225.175
Average Projectile Velocity $[m/s]$	Theoretical Projectile Velocity $[m/s]$
226	254

Table 5.2: Test N°2 Speed Measurement

The surrogate bird, after its separation from the sabot, maintained a good orientation

along its trajectory until it hit the target.

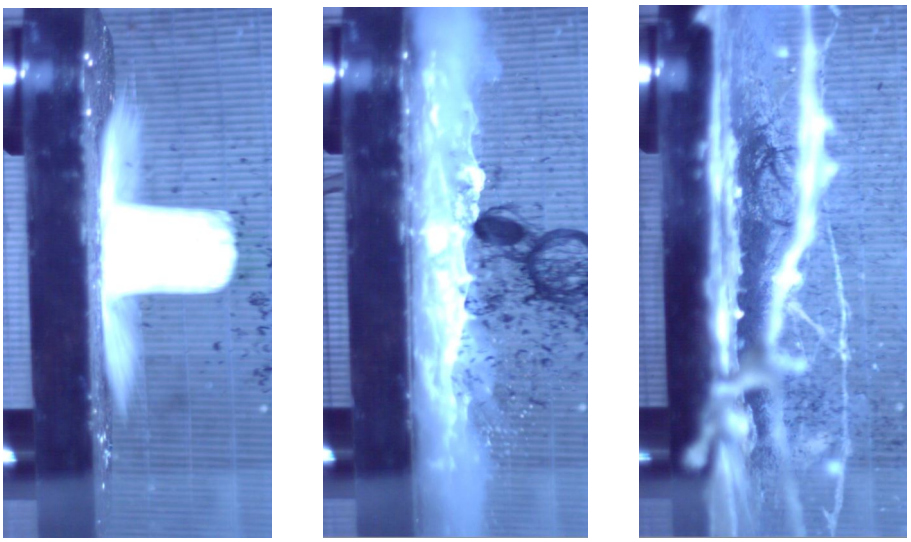

(a) (b) (c)

Figure 5.5: Test N°2 Impact Phase

EXPERIMENTAL TEST N°3:

By launching the S_{07} design prototype at a pressure of 7 [bar], it was experimentally found how the piece is able to maintain structural integrity until the impact with the stopper.

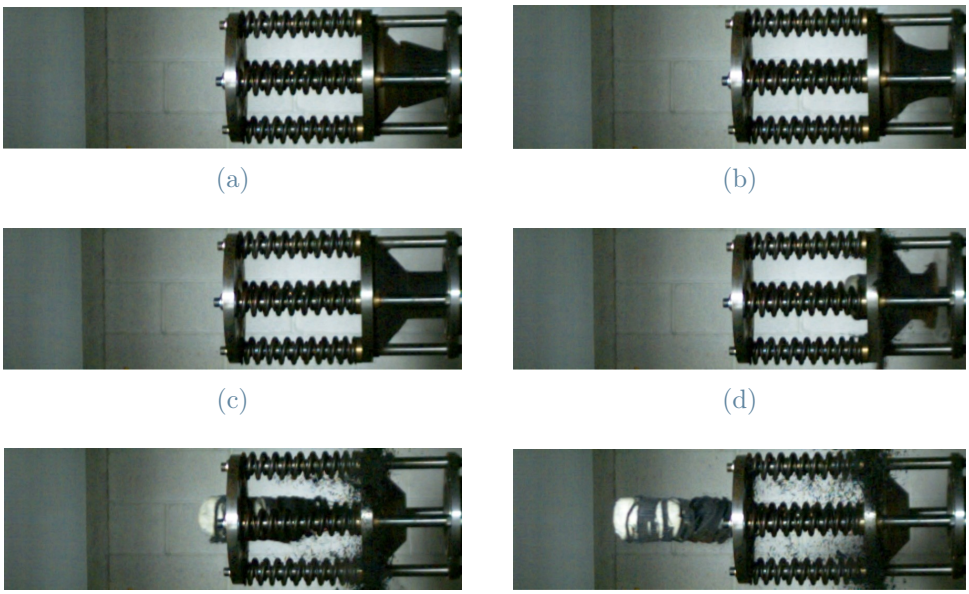

(a) (b) (c) (d) (e) (f)

Figure 5.6: Test N°3 Separation Phase

In the separation phase most of the debris are radially diverted, which translates into an advantage over the original sabot as there aren't debris in front of the projectile. However, from figures 5.6e & 5.6f appears that the sabot's central body isn't completely eliminated and tends to shrink the dummy bird. This phenomenon is undesired and led to design changes in later sabot versions, such as middle body enlargement. The sabot's base instead only generates debris along the projectile's wake, without disturbing it. Furthermore from the measured speeds (table 5.3) it has emerged that S_{07} prototype was able to confer a significant velocity increment to the surrogate bird, namely 5 $[m/s]$ higher than the one obtained with the original sabot at the same launch pressure:

Calibration Scale $[mm/pix]$	Projectile Velocity $[m/s]$
2.212	230.427
2.201	229.379
2.210	230.314
2.199	229.168
2.221	231.460
2.200	229.275
2.220	231.320
2.219	231.216
2.222	231.612
2.219	231.216
Average Projectile Velocity $[m/s]$	Theoretical Projectile Velocity $[m/s]$
231	267.8

Table 5.3: Test N°3 Speed Measurement

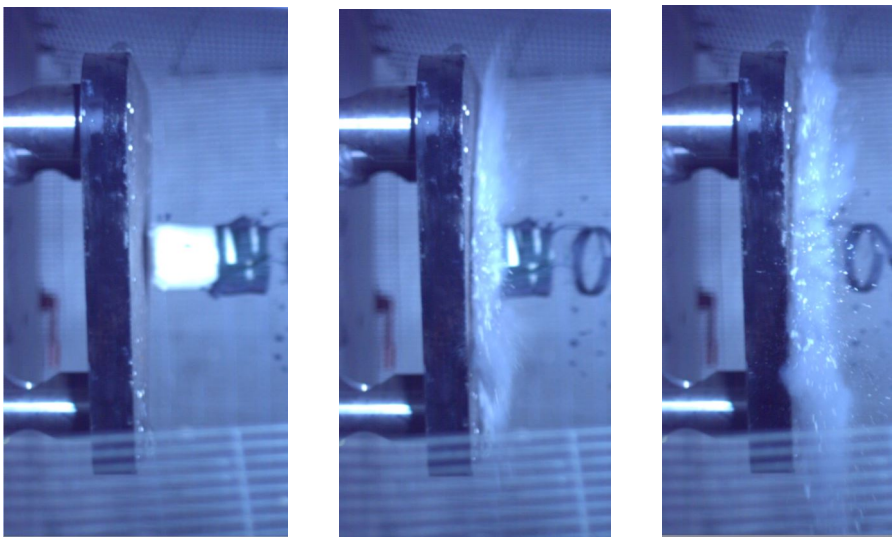

(a) (b) (c)

Figure 5.7: Test N°3 Impact Phase

EXPERIMENTAL TEST N°4:

Prototype S_{07} was then launched at a higher pressure of 7.5 [bar] in order to determine its limits as well as the maximum achievable speed with this design.

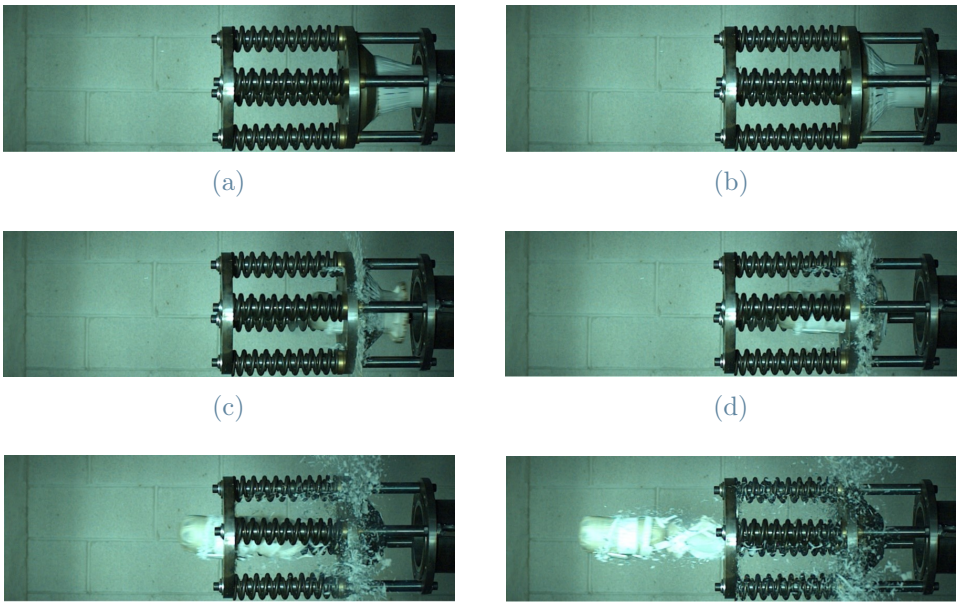

(a) (b) (c) (d) (e) (f)

Figure 5.8: Test N°4 Separation Phase

The sabot can still maintain structural integrity and is able to reach even higher velocities, performing a successful separation. However, middle body's debris remain and a slight squeeze of the dummy bird is still visible.

Calibration Scale $[mm/pix]$	Projectile Velocity $[m/s]$
1.354	250.439
1.351	249.113
1.351	249.113
1.362	251.145
1.366	252.231
1.347	249.091
1.358	250.470
1.398	252.492
1.358	250.47
1.364	251.838
Average Projectile Velocity $[m/s]$	Theoretical Projectile Velocity $[m/s]$
250	275.7

Table 5.4: Test N°4 Speed Measurement

The projectile follows a straight trajectory up to the impact with the target and has an optimal orientation, being perfectly aligned with the normal to the target's plane.

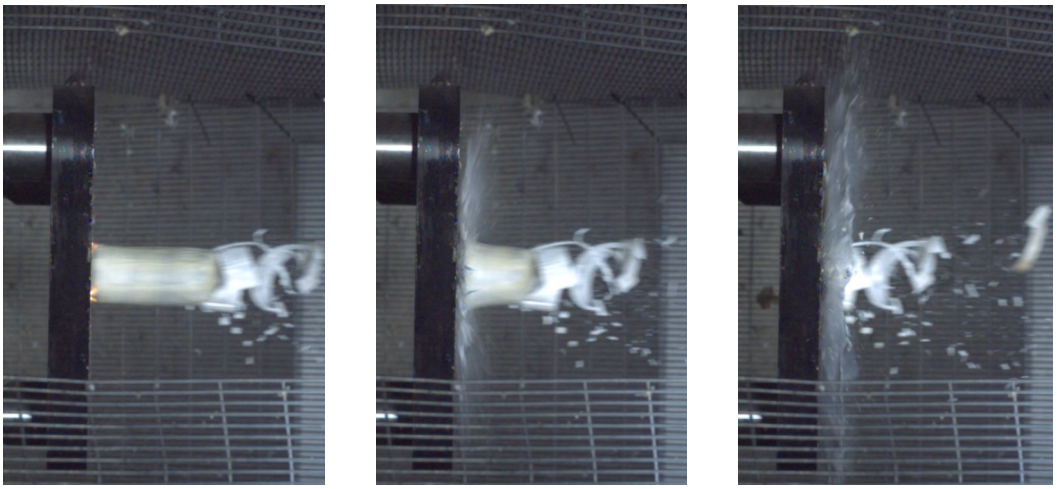

(a) (b) (c)

Figure 5.9: Test N°4 Impact Phase

EXPERIMENTAL TEST N°5:

Increasing the launch pressure up to 8 [bar], it was observed that prototype S_{07} is no longer able to withstand the applied loads, as it yielded inside the barrel before reaching the stopper. No velocities could be measured.

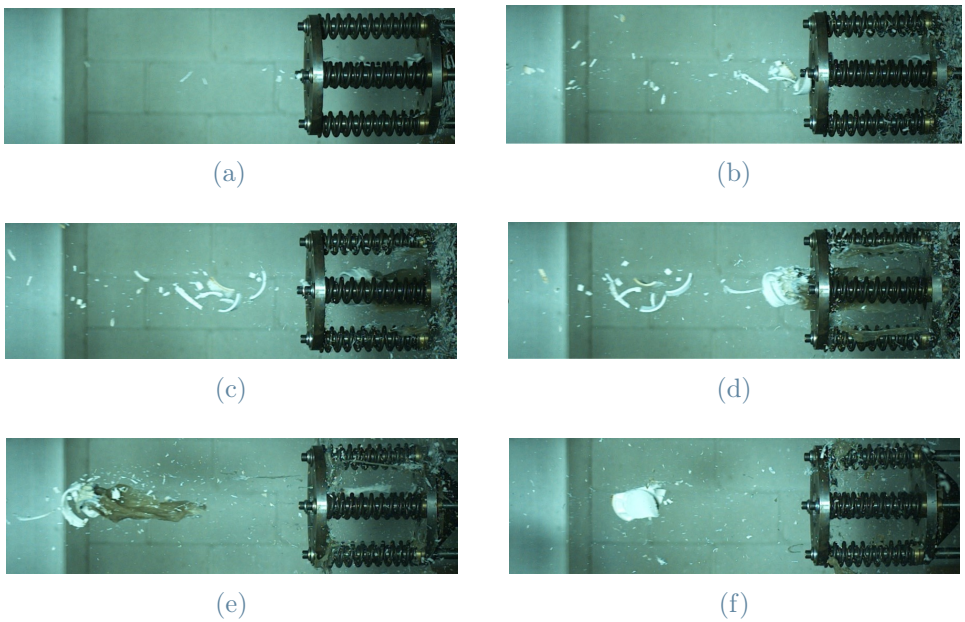

(a) (b) (c) (d) (e) (f)

Figure 5.10: Test N°5 Separation Phase

Although the launch was unsuccessful, it served to identify the limit operating condition for this design, which can be taken as the one described in the experimental test N°4. The maximum speed determined for the S_{07} sabot is therefore equal to 250 $[m/s]$.

EXPERIMENTAL TEST N°6: The prototype of the new S_{11} design was tested using the maximum bearable launch pressure (7.5 [bar]) from the previous S_{07} version. In this test it was also possible to investigate the effectiveness of teflon rings.

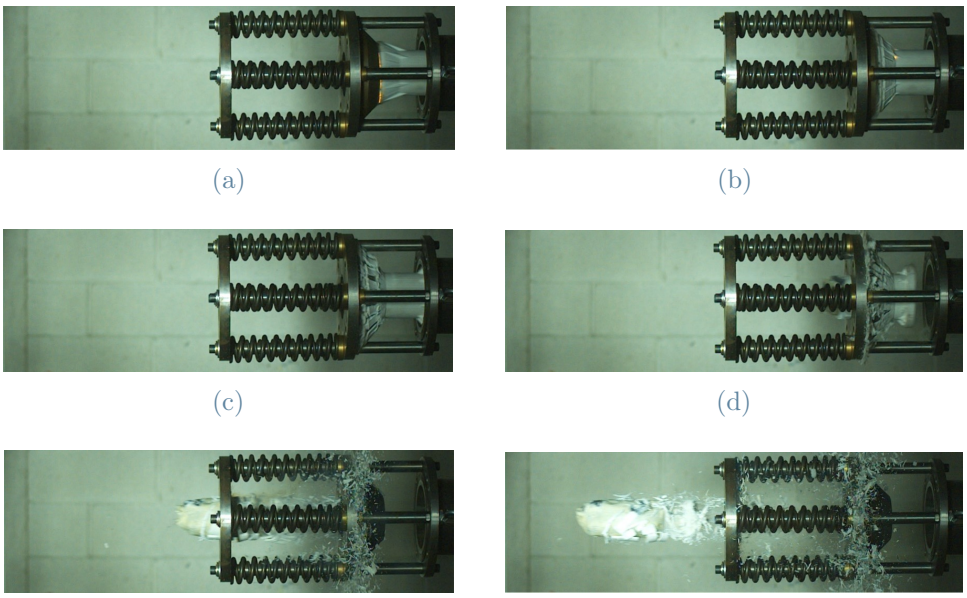

(a) (b) (c) (d) (e) (f)

Figure 5.11: Test N°6 Separation Phase

The sabot exhibited good behavior during the launch. Particularly appreciable was the separation, during which the divergent cone of the sabot opened radially on the stopper as designed (detail depicted in fig.). The test revealed an improvement in terms of debris generated, as the middle body is completely fragmented, eliminating the surrogate bird shrinkage problem. Generation of sparks was also observed at the first contact between stoppers and teflon rings, due to the high speeds reached. In fact, the teflon bearings configuration allowed to reach a higher velocity than the S_{07} prototype, providing an increase of about 13 $[m/s]$ even if projectile's total mass was 39 $[g]$ heavier than the one used in test N°4 (see tables 4.20 & 4.18).

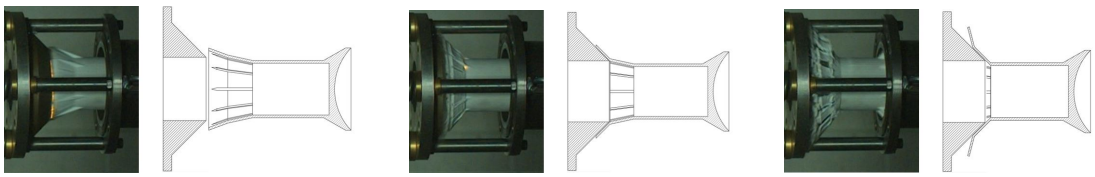

(a) (b) (c)

Figure 5.12: Divergent Cone Radial Opening

Calibration Scale $[mm/pix]$	Projectile Velocity $[m/s]$
1.333	261.979
1.342	263.966
1.329	260.639
1.340	263.573
1.341	263.859
1.332	261.898
1.347	263.982
1.329	260.639
1.331	261.499
1.341	263.859
Average Projectile Velocity $[m/s]$	Theoretical Projectile Velocity $[m/s]$
263	271.6

Table 5.5: Test N°6 Speed Measurement

Even if the surrogate bird maintains a good trajectory when leaving the stopper, at the impact with the target it can be observed that its orientation is not optimal, being inclined with respect to the normal to the target's plane.

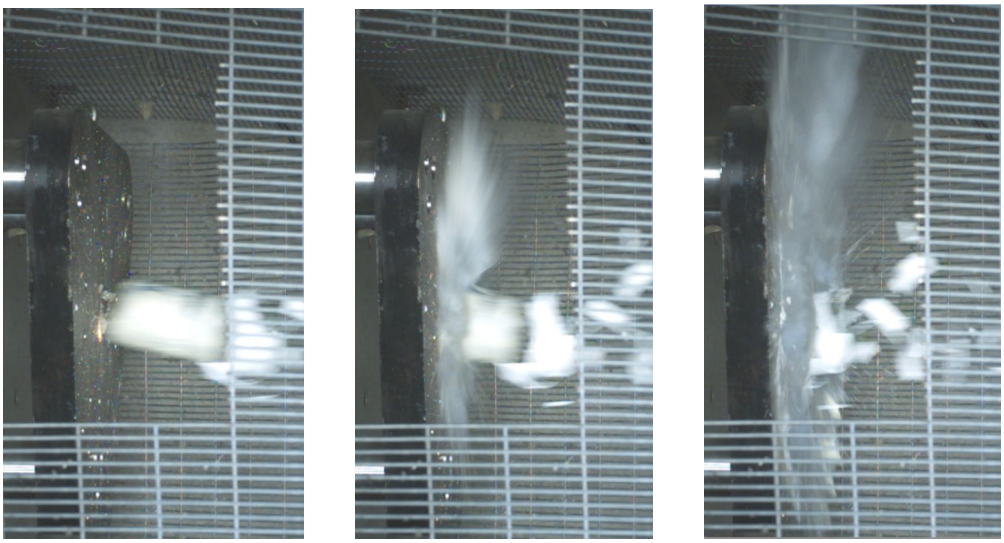

(a) (b) (c)

Figure 5.13: Test N°6 Impact Phase

EXPERIMENTAL TEST N°7:

This test was conducted at a launch pressure of 8 [bar]. The S_{11} design responded well, once again ensuring the structural integrity of the sabot until the collision against the stopper.

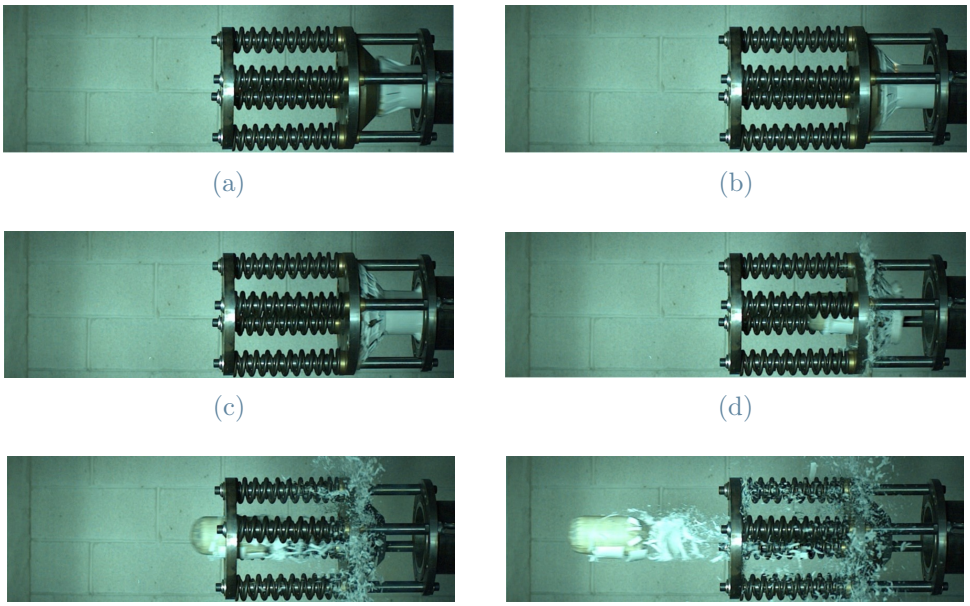

(a) (b) (c) (d) (e) (f)

Figure 5.14: Test N°7 Separation Phase

,The separation appears to be clean, with most of the debris remaining behind the surrogate bird. As a result of employing teflon rings and a high launch pressure, the highest recorded speed was reached during this test (reported in table 5.6).

The orientation of the surrogate bird just before the impact improves compared to the experimental test N has 6, although it is still visible a slight inclination with respect to the normal of the target plane.

Calibration Scale $[mm/pix]$	Projectile Velocity $[m/s]$
1.366	262.468
1.372	266.826
1.381	268.097
1.380	267.407
1.377	267.304
1.382	268.984
1.379	267.331
1.378	267.323
1.381	268.097
1.380	267.407
Average Projectile Velocity $[m/s]$	Theoretical Projectile Velocity $[m/s]$
267	279.7

Table 5.6: Test N°7 Speed Measurement

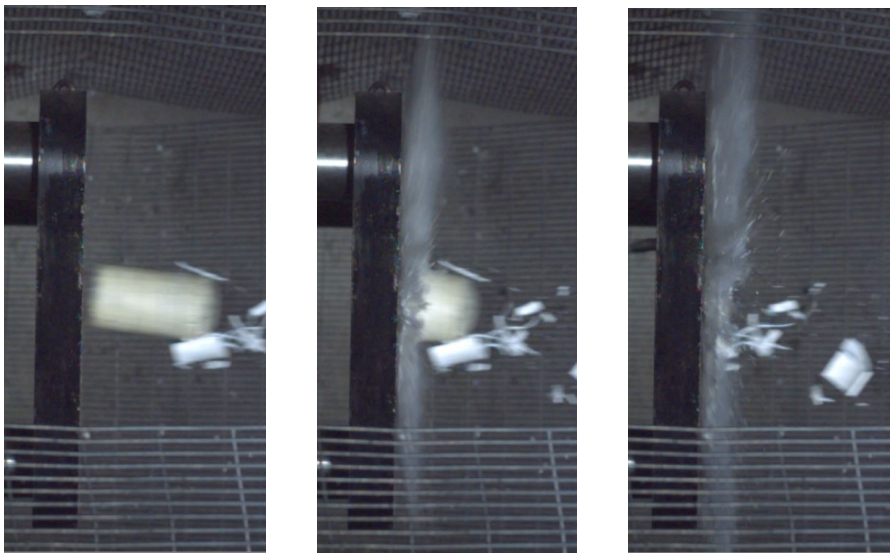

(a) (b) (c)

Figure 5.15: Test N°7 Impact Phase

Below is reported the trend of the theoretical speed for a projectile whose mass is equal to the average mass (1.36 [Kg]) of all fired projectiles in the performed experimental tests, as the pressure varies. On the same graph are also reported both theoretical and measured speed values for each experimental test:

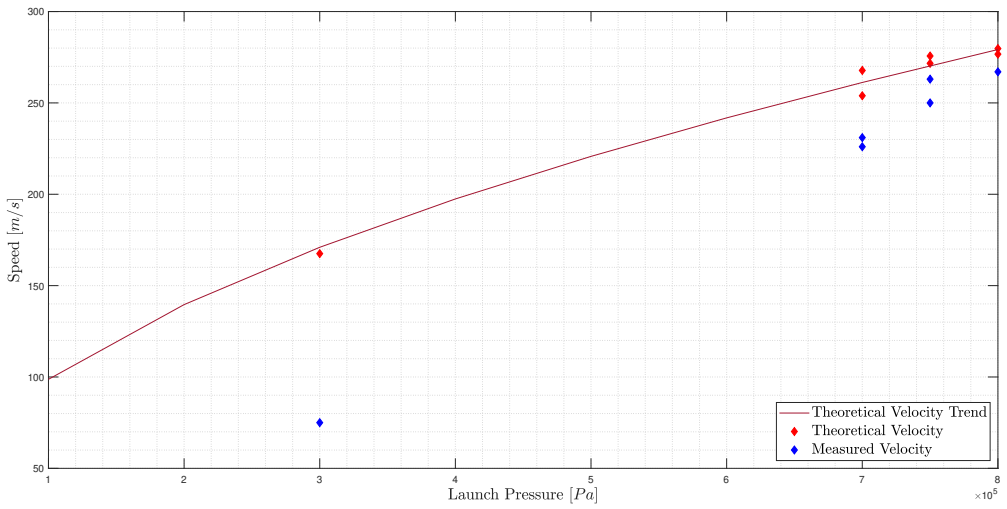

Figure 5.16: Speed Trend and Values

The graph shows that the measured speeds closest to their theoretical values are those related to the Sabot S_{11} in which the teflon bearings were used. From the experimental evidence it can therefore be stated that teflon rings actually proved to be effective by providing a significant reduction of the energy dispersed in the form of friction, which allows the achieve higher speeds. Another aspect that surely contributed to the increase in reached speeds is the mass optimization process. Below are shown all the iterations performed with the estimated mass values, provided by the 3D slicing software, for each developed design:

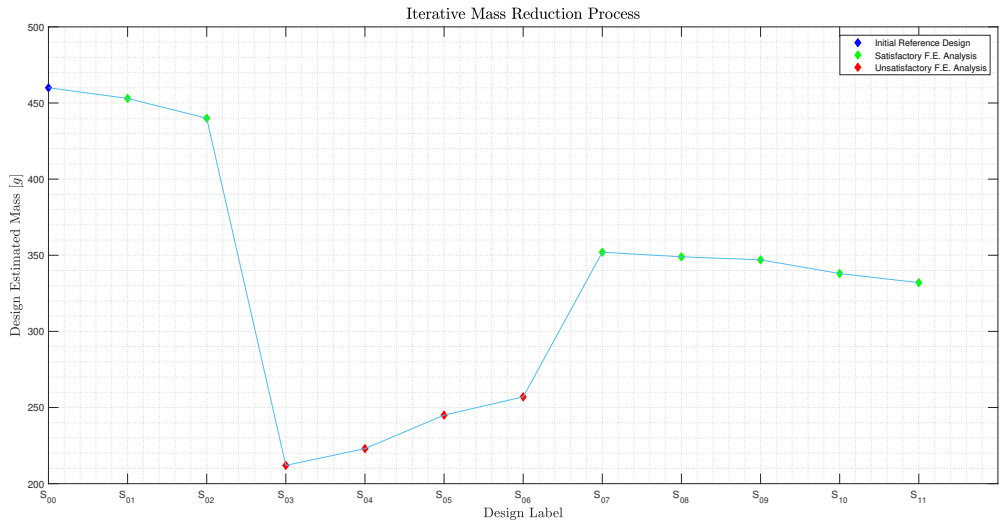

Figure 5.17: Iterative Mass Reduction Process

Please note that the two prototypes realized for the sabot design S_{11} were found to be extremely light, with a real mass of 323 $[g]$ and 326 $[g]$, respectively. The addition of Teflon bearings led their mass to increase so as to be comparable with the mass of the prototype corresponding to the design S_{07} (344$[g]$) without Teflon rings, which was used in experimental test N°4.

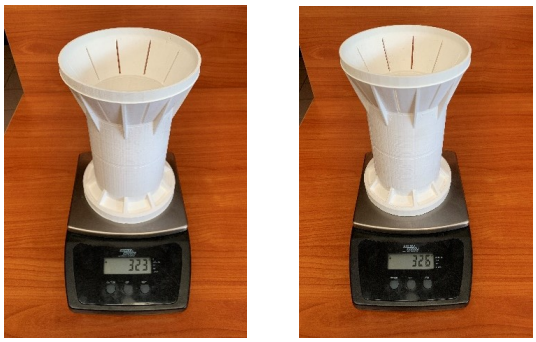

(a) (b)

Figure 5.18: S_{11} Design Masses without Teflon Rings

5.3. Experimental-Numerical Results Comparison

From the experimental results previously illustrated it emerges that all launches made for those designs whose numerical simulations gave satisfactory outputs, have been successful.

Sabot S_{07}, whose numerical simulation was performed with a launch pressure of 7 [bar], behaved as predicted by the F.E. analysis up to a pressure of 7.5 [bar] before failing when fired at 8 [bar]. Since the in-bore numerical model was able to correctly describe the sabot's macroscopic behaviour during launch, a good correlation level was reached between numerical outputs and field test results.

As for the second numerical model instead, it's not possible to validate it since it still presents inconsistencies at the level of contacts. Furthermore the model shall still be improved by exploiting a more suited formulation than the Lagrangian one, in order to take into account the large deformations which the sabot undergoes when impacting against the stopper. Despite these great limitations it should be noted that, however approximate, even this numerical model was able to capture a phenomenon occurred while testing the S_{07} sabot's prototype:

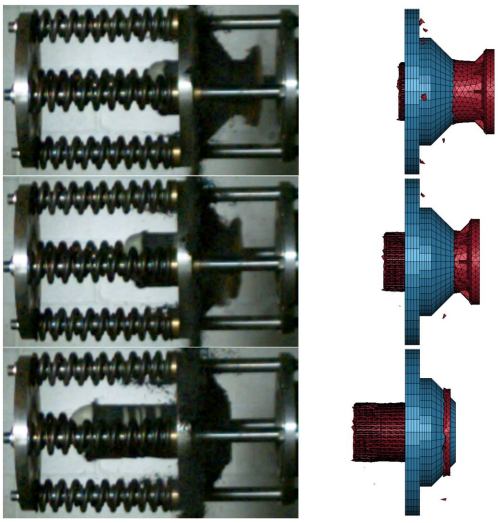

Figure 5.19: Middle Body Cutting Sequence

From experimental test N°3 it's indeed possible to observe how the middle body, with inner sandwich configuration, is actually cut by the stopper as shown in the numerical simulation.

6 | Conclusions and Future Developments

This Thesis work was conducted with the aim of developing a more performing sabot for high-speed bird-strike testing, in order to achieve higher maximum speeds than those obtained in the past at the La.S.T laboratory.

A design scheme was outlined and implemented exploiting both finite element numerical models and experimental tests providing feedback on the basis of which targeted design changes were carried out in order to achieve the best possible result. All developed numerical models were compared with the obtained experimental results and validated whenever a good level of correlation was found.

6.1. Conclusions

Several factors have been taken into account during the design process, with emphasis on some key principles including mass optimization. The geometry of the sabot has been optimized starting from the original one through material removal in correspondence of specific areas which don't affect the behavior of the sabot itself and its interactions with the surrogate bird and the stopper. Particular attention was also paid to the choice of material, the machinability of the final piece and its production process. All these elements helped guiding the design together with the results coming from all performed simulations and experimental tests. From the numerical tests which provided good results, only the lightest and most promising designs were selected for prototype production and experimentation.

With the first obtained result, namely Sabot design S_{07}, a considerable reduction in mass was achieved, ranging between 105 $[g]$ and 113 $[g]$ less with respect to the old sabot. This first new design has recorded during its testing an increase in speed of 5 $[m/s]$ (or 18 $[Km/h]$). In addition, the new design has made it possible to eliminate the problem of unwanted breakage of prototypes during their 3D-printing, through the use of a dedicated

spherical cap base.

Many subsequent versions for the sabot have been developed, always following the same design principles and procedures, in order to further improve the performance of the piece. During this next design phase, a solution with teflon bearings was also investigated, designed, and manufactured in order to reduce friction losses. The resulting design, labeled as S_{11}, maintained its structural integrity when launched at high pressures, showing great improvements in terms of velocity conferred to the projectile by providing a further speed increase of 13 m/s (or 46.8 km/h). The new sabot also has a much lower mass than the original one: only 326 [g] (without considering its teflon rings) against an initial mass of 457 [g].

6.2. Future Developments

The work carried out revealed some issues related to the measurement of the projectile's speed which, although better than measure tape-based measurements used in the past, still relies on a methodology inevitably affected by errors. A possible solution could be placing two photoelectric sensors after the stopper and separated by a known distance. Connecting a stopwatch to such system it would be possible to calculate the time elapsed when the surrogate bird passes in front of both photocells in a very accurate way. However, this solution also presents complications: quite often sabot's debris travel along with the dummy bird. Debris might pass through the sensors first, completely distorting the results or introducing a noise on the measurements that would require adequate filtering for their reading.

Another aspect which can be improved and that would help studying sabot's failure modes is to further develop the sabot impact numerical model. An SPH formulation may be the best choice also to predict how much debris are generated and in which directions they're deflected after the impact with the stopper.

In addition, Sabot's S_{11} design could be adapted to accommodate a small drone's components. Impacts between drones and aircraft in fact pose a new danger and are increasingly studied in these years. By adding dedicated supports inside the sabot's middle body the various components could easily interlock with one another. Clearly the drone's battery shall be replaced with a ballast of equivalent mass, in order to avoid uncontrolled explosions.

Bibliography

[1] G. J. Appleby-Thomas, D. Wood, A. Hameed, J. Painter, V. Le-Seelleur, and B. Fitzmaurice. Investigation of the high-strain rate (shock and ballistic) response of the elastomeric tissue simulant perma-gel®. *International Journal of Impact Engineering*, 94:74–82, 2016.

[2] J. P. Barber, H. R. Taylor, and J. S. Wilbeck. Bird impact forces and pressures on rigid and compliant targets. Technical report, Dayton Univ OH Research Inst, 1978.

[3] L. Barriere, M. Bouquet, and J.-F. Ferrero. Bird strike shielding materials: development of a high velocity impact test platform. In *SAMPE Europe*, 2015.

[4] F. K. Becker, R. L. Millikin, and A. J. Leslie. Using radar technology to assess visual monitoring accuracy of cape vulture movements. *Ostrich*, 91(1):83–90, 2020.

[5] É. Bélanger and P. Gosselin. Engineering development analysis of a segmented projectile discarding sabot. Technical report, NUMERICA TECHNOLOGIES INC QUEBEC CITY (CANADA), 2005.

[6] D. Bowman and G. Frank. Ibrg artificial bird project. *Work programmed and Schedule, United Kingdom*, 2000.

[7] T. N. Canning, A. Seiff, and C. S. James. Ballistic-range technology. Technical report, Advisory Group for Aerospace Research and Development Neuilly-sur-Seine (France), 1970.

[8] A. C. Charters. Development of the high-velocity gas-dynamics gun. *International Journal of Impact Engineering*, 5(1-4):181–203, 1987.

[9] G. Ćwikła, C. Grabowik, K. Kalinowski, I. Paprocka, and P. Ociepka. The influence of printing parameters on selected mechanical properties of fdm/fff 3d-printed parts. In *IOP conference series: materials science and engineering*, volume 227, pages 12–33. IOP Publishing, 2017.

[10] B. S. Davis, B. J. Guidos, and T. E. Harkins. Complementary roles of spark range and onboard free-flight measurements for projectile development. Technical report,

Army Research Lab Arberdeen Proving Ground MD Weapons and Material research, 2009.

[11] R. A. Dolbeer. Trends in reporting of wildlife strikes with civil aircraft and in identification of species struck under a primarily voluntary reporting system, 1990-2013. 2015.

[12] R. A. Dolbeer, M. J. Begier, P. R. Miller, J. R. Weller, A. L. Anderson, et al. Wildlife strikes to civil aircraft in the united states, 1990–2019. Technical report, United States. Department of Transportation. Federal Aviation Administration, 2021.

[13] C. Doolan. A two-stage light gas gun for the study of high speed impact in propellants. Technical report, AERONAUTICAL AND MARITIME RESEARCH LAB SALISBURY (AUSTRALIA) WEAPONS SYSTEMS DIV, 2001.

[14] W. Drysdale. Design of kinetic energy projectiles for structural integrity. Technical report, ARMY BALLISTIC RESEARCH LAB ABERDEEN PROVING GROUND MD, 1981.

[15] W. H. Drysdale, R. D. Kirkendall, and L. D. Kokinakis. Sabot design for a 105mm apfsds kinetic energy projectile. Technical report, ARMY BALLISTIC RESEARCH LAB ABERDEEN PROVING GROUND MD, 1978.

[16] A. GENÇER. Design of rigid wheat gluten materials. 2014.

[17] D. B. Gladman. *LS-DYNA Keyword User Manual*. Livermore Software Technology Corporation (LSTC).

[18] V. Goyal, C. Huertas, J. Borrero, and T. Leutwiler. Robust bird-strike modeling based on ale formulation using ls-dyna. In *47th AIAA/ASME/ASCE/AHS/ASC Structures, Structural Dynamics, and Materials Conference 14th AIAA/ASME/AHS Adaptive Structures Conference 7th*, page 1759, 2013.

[19] ICAO. Icao: Air transport monitor. URL `https://www.icao.int/sustainability/pages/air-traffic-monitor.aspx`.

[20] ICAO. Eletronic bulletin, 2008 - 2015 wildlife strike analyses (ibis), 2017.

[21] S. A. E. International. G-28 simulants for impact and ingestion testing, 2016.

[22] K. E. Kafdağlı. Development of a sabot design tool for aeroballistic range testing. Master's thesis, Middle East Technical University, 2006.

[23] J. Kittur, S. Vijaykumar, V. P. Bellubbi, P. Vishal, and M. Shankara. Comparison of different mcdm techniques used to evaluate optimal generation. In *2015 interna-*

tional conference on applied and theoretical computing and communication technology (iCATccT), pages 172–177. IEEE, 2015.

[24] P. Knupp. Remarks on mesh quality. Technical report, Sandia National Lab.(SNL-NM), Albuquerque, NM (United States), 2007.

[25] M. Lobdell, B. Croop, and H. Lobo. Comparison of crash models for ductile plastics. In *10th European LS-DYNA User's Conf.*, 2015.

[26] N. Maqsood and M. Rimašauskas. Delamination observation occurred during the flexural bending in additively manufactured pla-short carbon fiber filament reinforced with continuous carbon fiber composite. *Results in Engineering*, 11:100246, 2021.

[27] J. A. Martin, J. L. Belant, T. L. DeVault, B. F. Blackwell, L. W. Burger Jr, S. K. Riffell, and G. Wang. Wildlife risk to aviation: a multi-scale issue requires a multi-scale solution. *Human-Wildlife Interactions*, 5(2):198–203, 2011.

[28] B. M. Molnar, S. McGrady, J. Liquore, K. Schroeder, and J. Kozak. Launching station for sensor deployment.

[29] NTSF. Accident report us airways flight 1549, ntsb/aar-10/03, 2009.

[30] E. Oñate, A. Franci, and J. M. Carbonell. Lagrangian formulation for finite element analysis of quasi-incompressible fluids with reduced mass losses. *International Journal for Numerical Methods in Fluids*, 74(10):699–731, 2014.

[31] J. Reaugh. Results of a preliminary assessment of an explosive projectile launch system. Technical report, Lawrence Livermore National Lab.(LLNL), Livermore, CA (United States), 1995.

[32] T. L. Saaty. What is the analytic hierarchy process? In *Mathematical models for decision support*, pages 109–121. Springer, 1988.

[33] A. S. Seetamsetti. *Comparison of finite element analysis of impact on water and soil using Lagrangian, ALE, and SPH approaches and airframe impact applications*. PhD thesis, Wichita State University, 2012.

[34] R. Torre and S. Brischetto. Experimental characterization and finite element validation of orthotropic 3d-printed polymeric parts. *International Journal of Mechanical Sciences*, 219:107095, 2022.

[35] E. Triantaphyllou, S. H. Mann, et al. Using the analytic hierarchy process for decision making in engineering applications: some challenges. *International journal of industrial engineering: applications and practice*, 2(1):35–44, 1995.

[36] E. Triantaphyllou, B. Shu, S. N. Sanchez, and T. Ray. Multi-criteria decision making: an operations research approach. *Encyclopedia of electrical and electronics engineering*, 15(1998):175–186, 1998.

[37] Z. Wang, J. Liu, and D. Hui. Mechanical behaviors of inclined cell honeycomb structure subjected to compression. *Composites Part B: Engineering*, 110:307–314, 2017.

[38] .-D. Wasp. *Delta Wasp 2040 Manual of Use and Maintenance*. CSP S.r.l.

[39] P. Zhang, D. J. Arceneaux, and A. Khattab. Mechanical properties of 3d printed polycaprolactone honeycomb structure. *Journal of Applied Polymer Science*, 135 (12):46018, 2018.

List of Figures

List of Tables